University of Groningen

Research Project

Modeling and simulations of the Ocean Grazer's floater blanket under irregular wave: a Port-Hamiltonian approach

Author:
Roelof Jan Boer

Supervisors:
1st supervisor: Prof. Dr B. Jayawardhana
2nd supervisor: Prof. Dr. A. Vakis

Version: Thesis, first print

Industrial Engineering & Management

August 30, 2018

Abstract

The Ocean Grazer device is a novel wave energy converyer developed at University of Groningen. It is a novel hybrid renewable energy device which can harvest wind and wave energy to provide short-to-medium term energy output that can be stored on-site and allows it to decouple the variability of renewable energy sources from the supply to the grid.

As part of the design process, the development of an accurate mathematical model, describing the physical interaction of the wave and the floater blanket of the Ocean Grazer, and subsequently their interaction with the power take-off systems becomes an essential element in this complex and costly design process. Such a model will enable the Ocean Grazer's group to optimize the mechanical design, to develop the control algorithms for maximizing the energy capture, and more importantly, to predict the overall behaviour of the device prior to its deployment in the ocean.

In this research thesis, we extend the previous work on the modeling of the wave-floater blanket interaction. The first contribution of the thesis is the development of a port-Hamiltonian model that describes the wave-floater blanket simulation. The generic dynamical model is applied to the case of a floater blanket with ten floaters, under irregular waves, and is validated with the existing computer model using WEC-sim. The second contribution of the thesis is the performance analysis of the Ocean Grazer's floater blanket (with ten-floaters) connected to linear PTO systems. As part of our first contribution, we investigate the modeling of a realistic irregular wave based on the well-studied Bretschneider wave spectrum. In particular, we present the design of such an irregular wave generator by employing a white-noise generator coupled with a specially designed band-pass filter.

Using this realistic irregular wave time series, we validate the dynamic behaviour of the ten-floater case that is modeled using our port-Hamiltonian model. The simulation is compared with that using the popular WEC-sim computer model that is widely used for simulating various wave energy converters. For the regular wave, a maximum error of 0.0125 meters on a relative body displacement of 1 meter, which corresponds to an error percentage of 1.25% For the irregular wave, the error percentage is about 1.88%

During the investigation of the performance of the floater-blanket, several experiments where conducted. Analysis learns that under irregular waveinput, concerning the the contribution of energy, the radiation system is dominant over the mechanical system. The model behaves opposite under regular wave input, where the mechanical system is dominant. During the experiments the captured energy shows a sharp decline at higher order dampening coefficients and is different under regular and irregular wave inputs. The results of experiments using Ocean Grazer's scaled lab setup, due to the assumptions, aren't regarded as suffiently accurate, but suggest a lower powercapture than assumed in previous work, further research is recommended.

Contents

List of Constants

An alphabetical ordered list of the constants used in this thesis, **unless** otherwise specified.

Symbol	**Constant**	**Value**
A_b	Basal area of the buoy	49 m^2
b_{pto}	PTO damping coefficient	1.153·106kg/s
g	Gravitational acceleration	9,81 m/s^2
H_b	Height of the buoy	2 m
m_b	Mass of the buoy	45 000 kg
$m_{\infty i,i}$	Added mass of the buoy due its own movement	1,0545 $x10^5$ kg
$m_{\infty i,j}$	Added mass of the buoy due the movement of the other buoy	1,1327$x10^4$ kg
S_p	Separation between the piston and the cylinder	400 μm
μ	Viscosity of the working fluid	0,0734 Pa-s
ρ	Density of the working fluid	1000 kg/m^3
ρ_s	Density of the sea water	1025 kg/m^3

List of Variables

An alphabetical ordered list of the variables used in this thesis, unless otherwise specified.

Symbol	**Variable**	**Units**
b	Damping coefficient	kg/s
c	Filtering factor	-
f_b	Buoyancy force	N
f_{ex}	External excitation force	N
f_{pto}	Forces exerted by the PTO	N
f_r	Radiation force	N
G	pH input matrix	-
H	Hamiltonian function	J
h_M	Mean wave height	m
h_s	Significant wave height	m
h_b	Height of the buoy's movement	m
J	pH interconnection matrix	-
K	Matrix of spring coefficients	N/m
k	Stiffness coefficient	N/m
k_{pto}	PTO stiffness	N/m
m_∞	Added mass matrix at infinite frequency	kg
m	Mass of the system	kg
m_w	Mass of the column of water	kg
n	Number of buoys	-
p	Momentum	kg-m/s
$\dot{p}$	Force	N
q	Displacement	m
$\dot{q}$	Velocity	m/s
$\ddot{q}$	Acceleration	m/s^2
R	pH dissipation matrix	-
r	Radiation component	-
t_M	Mean wave period	s
t_s	Significant wave period	s
u	Input of the system	-
x	State of the system	-
y	Output of the system	-
z	Radiation component	-
φ	Convolution kernel	-

List of Abbreviations

An alphabetical ordered list of the abbreviations used in this thesis is given next.

DoF	**D**egree **o**f **F**reedom
MP^2	**M**ultiple-**P**iston **M**ultiple-**P**ump
MPP	**M**ultiple-**P**iston **P**ump
OG	**O**cean **G**razer
FIR	**F**inite **I**mpulse **R**esponse
IIR	**I**nfinite **I**mpulse **R**esponse
ISSC	**I**nternational **S**hip **S**tructures **C**ongres
ITTC	**I**nternational **T**owing **T**ank **C**ongress
JONSWAP	**J**oint **N**orth **S**ea **W**ave **O**bservation **P**roject)
MP2PTO	multi-piston, multi-pump, power take-off
MPC	**M**odel **P**redictive **C**ontrol
NREL	U.S. **N**ational **R**enewable **E**nergy **L**aboratory
pH	**P**ort-**H**amiltonian
SNL	**S**andia **N**ational **L**aboratories
PTO	**P**ower **T**ake-**O**ff
WEC	**W**ave **E**nergy **C**onverter

Chapter 1

Introduction

1.1 Renewable energy

For the past decade energy from renewable sources has been trending. Society has become more aware of the impact of non-renewable energy and technologies like solar panels have become more readily available. Governments, in turn, set goals and provided a legislative framework in which development becomes possible. The Dutch government, for example, aims at 14,5% renewable energy in 2020 and 100% renewable energy in 2050. In 2010 the Dutch government envisioned the distribution of energy sources, as is shown in Figure 1.1.

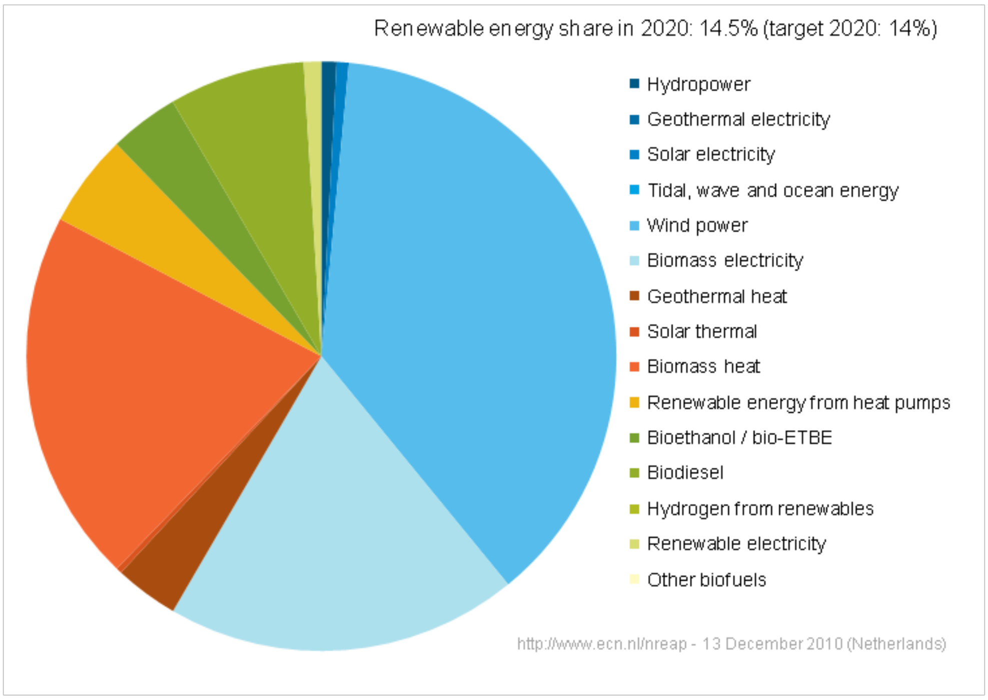

FIGURE 1.1: The Netherlands target 2020 [1], according to the energy agreement The Netherlands should atleast have 14.5% renewable energy at 2020.

This is to date still a far stretch, because the situation in 2016 as shown in Figure 1.2 is still around 5.4% (Hernieuwbare energie = Renewable energy). To achieve the 14,5% renewable energy, there are

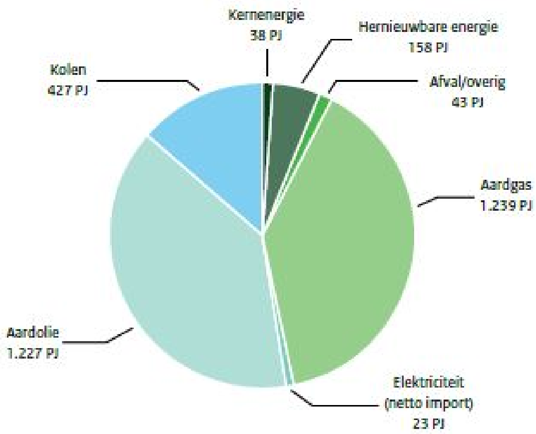

Figure 1.2: An overview of energy sources in the Netherlands, situation in 2016, 5.4% of The Netherlands energy demand is renewable [2].

several sources of renewable energy available, solar, geothermal, hydro and wind power. Of all renew-

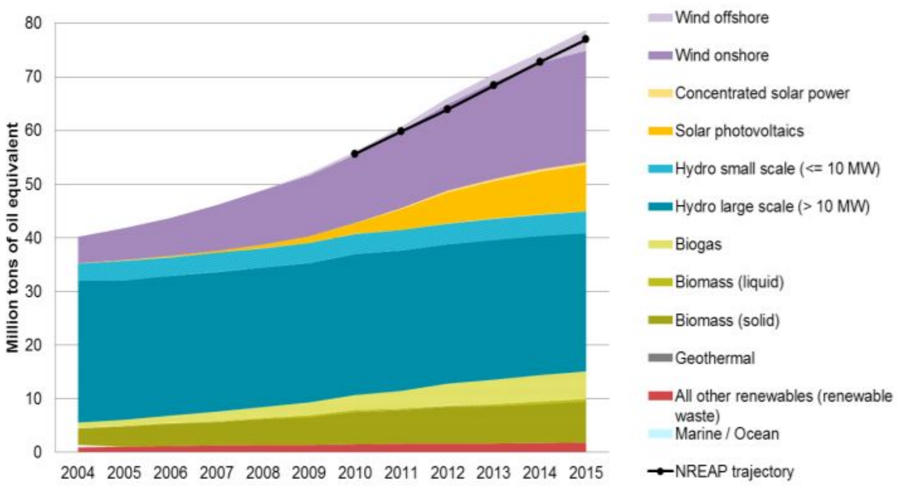

Figure 1.3: An overview of energy sources in the Netherlands, situation in 2016 [2]

able energy sources, hydropower is the most utilized within the European Union, and while its share dropped from 74% in 2004 to 38% in 2015, it still contributes the highest renewable energy generation.

Hydropower consists mainly of producing electricity by the use of gravitational force, acting upon flowing water. In the Netherlands, unfortunately, there is not enough height difference available to make use of gravitational force of flowing water. The original renewable energy plan of 2010, Figure 1.1 initially called for several percents of energy extracted from waves. A source of renewable energy that is still not often utilized is wave-energy extraction. Extraction of wave-energy can be realized through a device commonly known as a wave energy converter[3]. While first patented by Pierre-Simon Girard 1799 in France to drive pumps, mills and other heavy machinery [4][5], due to high costs of construction, deployment and maintenance, development of wave energy converters staggered until the 1960's. During the oil shortage crisis in 1973, the scientific community became particularly engaged in extracting energy from waves[6]. The following research has led to the development of roughly four groups: point absorber buoys, surface attenuators, oscillating water columns, and overtopping devices [7].Point absorber buoys operate, like surface attenuators from the *mechanical flexing and bobbing principle*, but unlike surface, attenuators have dimensions smaller than the wavelength. Figure 1.4

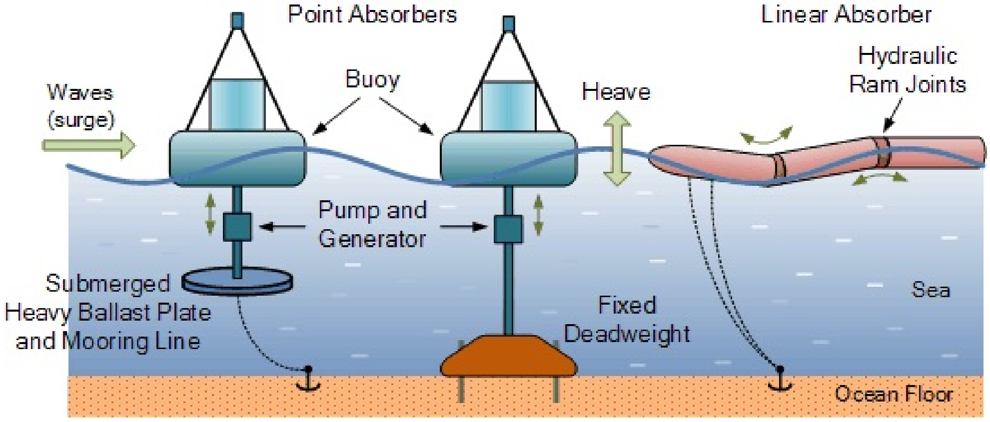

FIGURE 1.4: Mechanically flexing and bobbing principle wave energy converters, [8]

illustrates point absorbers (bouys) that consist of a buoy, are fixed to the ocean floor by either a mooring line or a fixed deadweight. They absorb wave energy by "*bobbing*", moving up and down on the motion of the waves. These motions drive hydrodynamic or electric generators. In attenuators, hydraulic or electric generators in the joints between the cylindrical components resist mechanical flexing. When this joint is flexed (as shown in 1.4), electricity is generated. Both devices can be found directly installable on the seabed using fixed deadweights and in the case of deep water the wave energy converters can be installed using a moring line. Surface attenuators are used in the worlds first grid-connected wave farm; The 2,25MW Aguaadoura Wave plant, located in Portugal, consists of three coupled 750kW Pelamis devices, as shown in Figure 1.5. The original goal of the Pelamis project

FIGURE 1.5: Pelamis machines, during sea trials, one practical example of the mechanically flexing and bobbing principle [9]

was to scale up the project to 25 Pelamis machines, increasing the capacity to 21 MW [10]. While the Pelamis offered a good prognosis and reasonable efficiency, the newly developed machines where prone to technical issues, the project was stopped after two months in operation, and the Pelamis company went out of operation in 2014 [11][12]. The oscillating water columns, are stationary and floating air chambers with the bottom open to the sea water below the waters free surface. They can be found near/on shorelines, and float at sea. These work by letting the moving waves create a pressure difference between the outside air and the air column trapped inside the structure [13]. Figure 1.6 shows the operating principle of an oscillating water column system. In this system, the

(A) The Wells turbine of the Limpet osciliating water collumn, indicating the real world scale, [14]

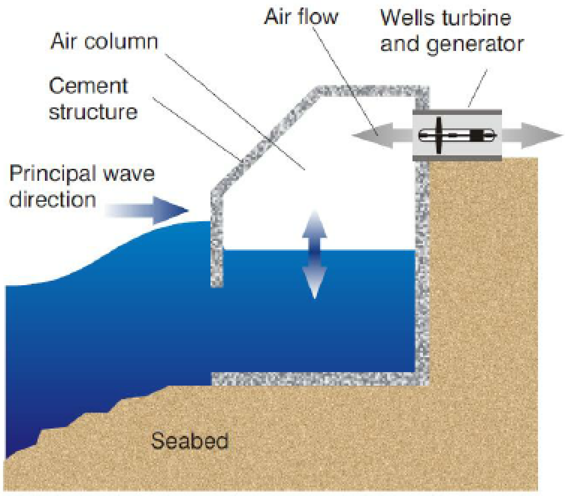

(B) Working example of the Limpet oscillating water column,[15]

Figure 1.6: Oscilating water column system

water column moves up and down, this pull's air in and pushes air out of the system through a turbine and generator. The movement of air through the turbine generates electricity.

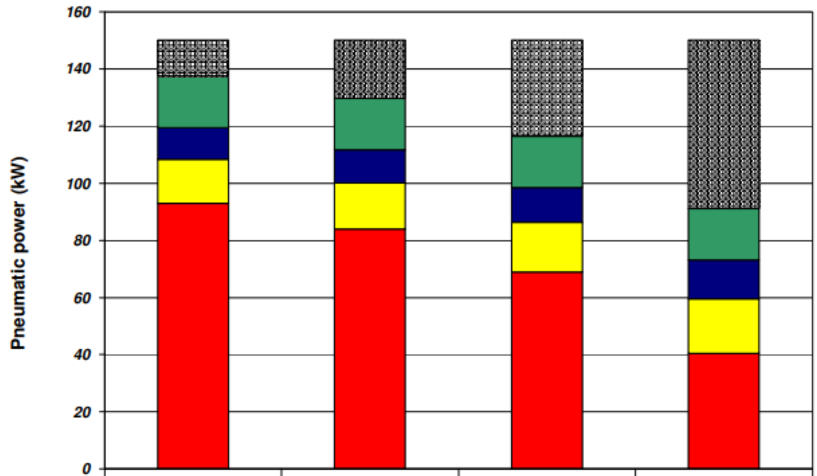

	A - Current	B - Opt Speed	C - Balanced	D - Theoretical
Supplied power	12.53	20.34	33.51	58.85
Inverter losses	18.00	18.00	18.00	18.00
Generator losses	11.08	11.49	12.18	13.52
Windage losses	15.39	16.16	17.31	19.14
Turbine losses	93.00	84.00	69.00	40.50

FIGURE 1.7: Efficiency of the Limpet oscillating water column, according to [13]. The figures, reported in 2004, denote the losses in KW, turbine losses come at 93KW.

An example of such a system is the Limpet system; this system operates off the cost of the island of Islay. It operates now for ten years, with 98% uptime according to the owner [13]. There are however drawbacks of the Limpet system, as can be seen in Figure 1.7. The efficiency of the system during a series of trial months is low due to the number of turbine losses. Of the roughly 150 kW pneumatic power, only 12.53 kW of electricity can be realized. According to the company owning the Limpet system, the low efficiency is mostly blamed on the control algorithm and speeding and slowing of the turbine due to reversing of the wave vector. However, the maximum practically obtainable efficiency according to the company owning the system (situation C of Figure 1.7) is at 33.51kW electric, 22.3% and still low. Overtopping devices, or sometimes referred to as wave capture devices, are devices that

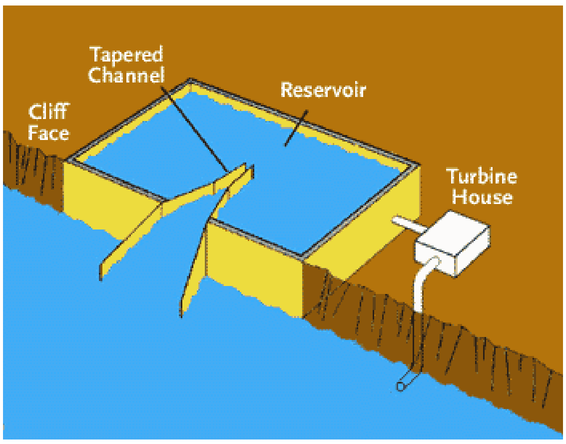

FIGURE 1.8: Example of a shoreside overtopping device, in this case Tapchan power plant [16]

operate on the shoreline or near the shore. Overtopping devices capture the incoming wave and convert

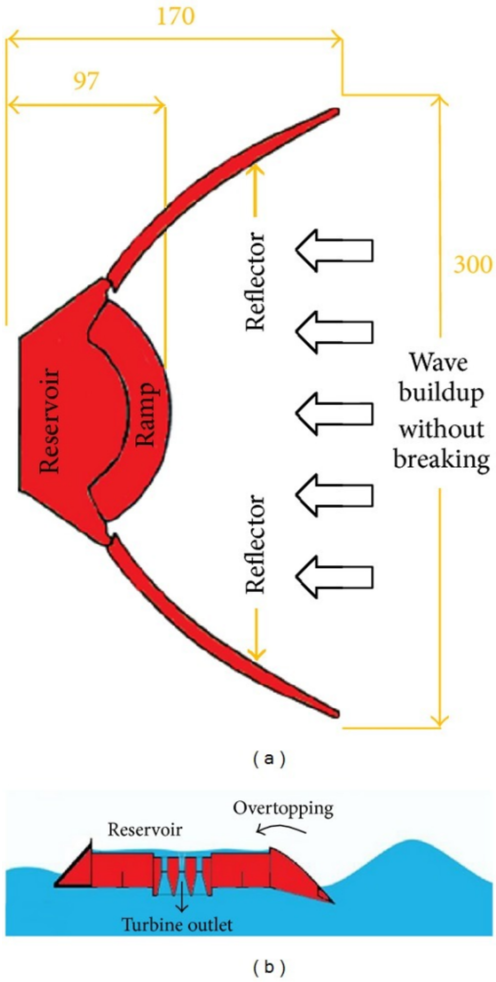

FIGURE 1.9: Example of a floating overtopping device, in this case the "Wave Dragon", operating in the black sea [17]

that wave energy into potential energy. This potential energy is converted to electric energy using a turbine. A nearshore variant is shown in Figure 1.9. This specific overtopping device carries two reflector beams. These Reflector beams aim to reflect the waves inward onto and over the ramp. The, by the shape of the beams and ramp, lifted wave, fills the reservoir, after which the potential energy is converted to electric energy in a turbine. Due to their low but oscillating differential pressure, high internal leakage, their respective reported efficiency is around 30%. The shoreline variant, Figure 1.8 works by channeling water along a horizontal man-made tunnel, this channel is funnel-shaped and is wide at the seaside where the waves enter. At the reservoir, the channel is narrowed, as the waves propagate along the narrowing channel the wave height is lifted due to the funneling effect to a level exceeding that of the reservoir. Water is then allowed to spill into a confined basin above the normal sea level. As the water is above sea level, the potential energy of the water trapped in the basin can be extracted by draining the water back to the sea through a low-head turbine as before.

1.2 The Ocean Grazer

The original Ocean Grazer is a novel wave energy converter concept that has advantages over existing designs. The concept consists of two basins, pump systems, turbines and a system of floaters. Development of the Ocean grazer has seen multiple concepts, of which version 1 and version 2 are the main distinguishable versions. Key features of either design are the multi-piston pump (referred to as MP2PTO system), and the energy storage. The MP2PTO, or multi-piston, multi-pump, power take-off (PTO), principle consists of a buoy that drives a PTO system which in turn drives one or multiple pistons depending on the amount of energy that can be extracted from a wave. The multi-piston-pump allows for optimized energy extraction and adaption to changing situations. The difference with point absorber systems is that the floater system allows for multiple buys.

1.2.1 Version one

Version one focusses on making a large dedicated structure. It consists out of a grid of interconnected floater elements (also known as a floater blanket), each floater is connected to a piston type hydraulic pumping system. The difference with standard point-absorber systems is that in an interconnected floater blanket, shown in Figure 1.11, each individual floater is connected to multiple pistons. This so-called *multi piston pump system* allows the ocean grazer to minimize radiation effects and hydrodynamic energy losses. The adaptability of the power take-off, the multi pistons, allows the ocean grazer to extract the energy of various wave heights efficiently and its ability to provide a predictable and stable energy output on demand, using its large energy storage capacity, distinguishes the Ocean Grazer from existing devices.

Figure 1.10 shows the working principle of the Ocean Grazer concept schematically. As waves move floater bodies ($B_1..B_4$), the PTO system will be moved ($P_1..P_4$). This PTO system is illustrated by a single piston but consists of multiple pistons and will pump the working fluid to the upper reservoir. The potential energy, caused by the difference in height, in Figure 1.10 shown by H, can be converted to electric energy using a turbine after which the working fluid flows back to the lower reservoir. Previous research shows that the design can take advantage of fast-changing energy prices to optimize production [18].

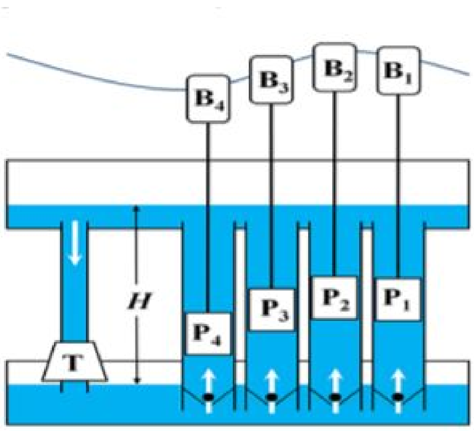

FIGURE 1.10: Ocean grazer working principle, Floaterbodies $B_1..B_4$ are manipulated by waves, this moves the PTO system consisting of multiple pistons, this moves water to the upper reservoir, the potential energy due to height(H) is converted to electric energy by means of a turbine [19]

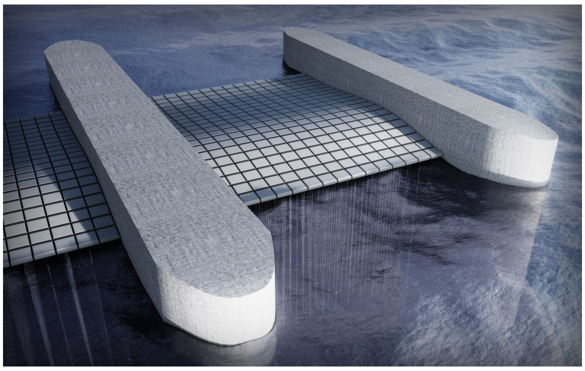

(A) Floater blanket construction showing two dimensional arrays of floaterbodies

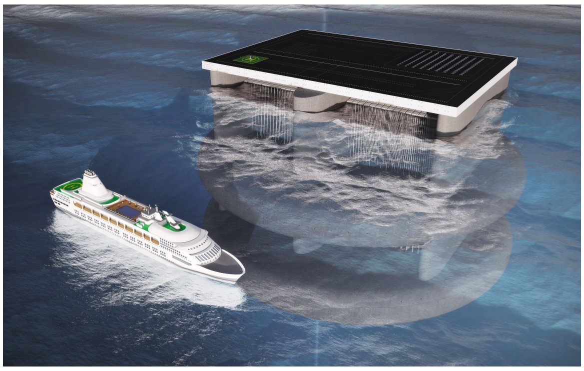

(B) Scale, Ocean grazer vs Cruise ship

FIGURE 1.11: Ocean grazer version 1 [19]

While the Ocean Grazer is a large structure in size,Figure 1.11, research has shown that it has favourable financial potential[18].

1.2.2 Version 2, concept 3.0

Where the first version contained a large structure focused mainly on wave energy, requiring a huge investment, the second version is smaller, modular and can directly be integrated/combined with offshore wind turbine platforms, thereby, reducing initial investment. The second version further contains fewer floaters, this, in turn, means that there are fewer interfaces between outside and inside the structure, reducing the leakage potential. This version can be integrated into offshore wind farms, connecting to their electric power grid and the supporting structure of the windmill is used as the lower basin and kept at atmospheric pressure. The base section of the windmill, see Figure 1.13, contains

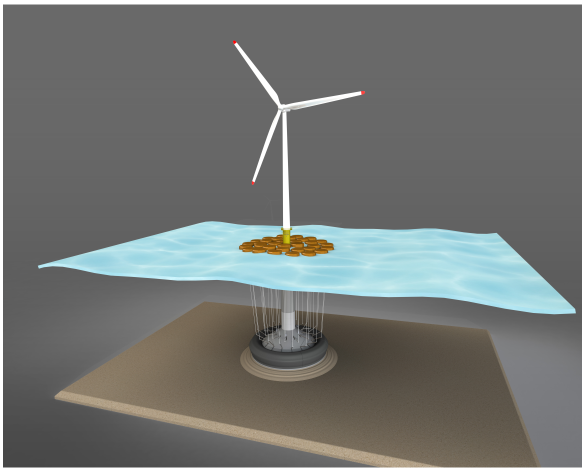

(A) Ocean grazer render[20]

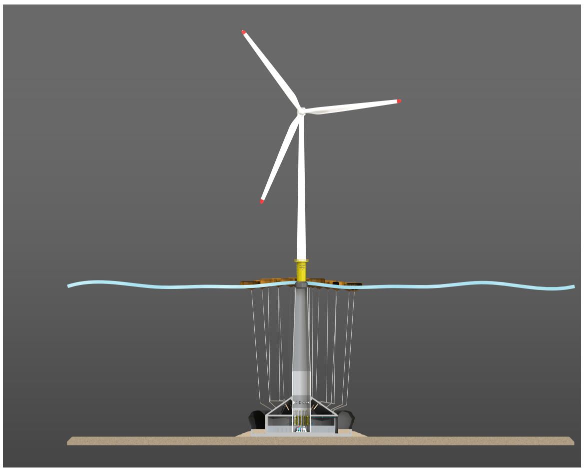

(B) Ocean grazer, mid section[20]

FIGURE 1.12: Ocean grazer version 2, concept 3.0

pumps, turbine, and basin under atmospheric pressure. The pumps pump the water from the basin to the energy storage. This energy storage is a rubber bag/bellows type of storage vessel. Since the energy is stored in a flexible rubber reservoir that interacts directly with the high hydrostatic pressure from the ocean water in its surrounding.

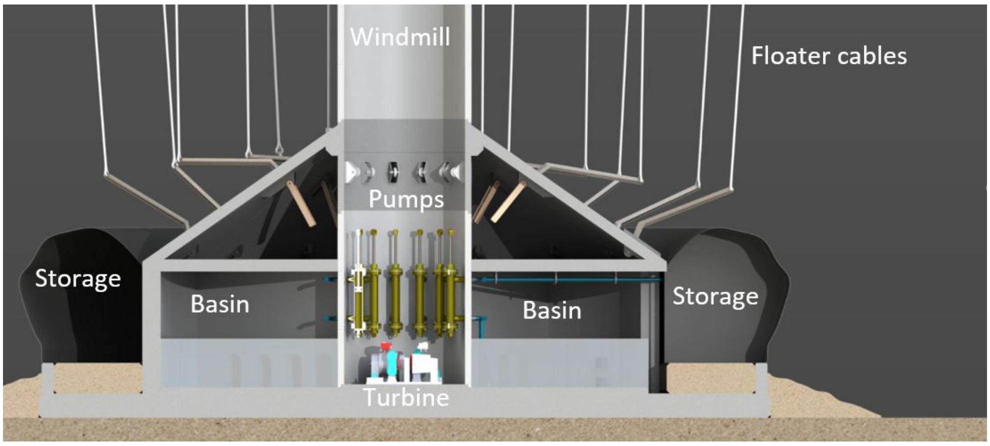

FIGURE 1.13: Ocean grazer working principle, surrounding the flexible rubber *storage* bladder, is ocean water, using the hydrostatic pressure to keep the working fluid in the *storage* bladder under pressure.

1.3 Background and context of the Assignment

The ocean grazer is a concept that depends heavily on its configurable pumps to ensure energy capture maximization, along with its basin that can release the loss-less stored energy at the right time. The big advantage and unique selling point of the ocean grazer is its ability to produce electricity almost instantly on demand, enabling the device to control its electricity production and thereby can sell its electricity to the energy markets at moments when prices are high.

To enable the ocean grazer to capture and sell the energy efficiently, the ocean grazer system requires a control system capable of maximizing energy output for a series of floaters in a setting with irregular sea waves. Research has shown that model predictive control is the best control option for the Ocean Grazer system. To design, test and implement the in earlier research advised model predictive control, the port-Hamiltonian model needs to be scaled up to accomodate an array of floaters. In this research, the focus is not on the controller of the system itself, but on expanding the knowledge on the process that will mimic the real behavior of the system. These simulations are important for the ocean grazer concept since it is one step towards the goal of maximizing the extraction of available wave energy. Modeling of a port-Hamiltonian system

1.4 Earlier Research

Earlier research by the members of the Ocean grazer group has resulted in a very tractable port-Hamiltonian model that has been validated against WEC-Sim, a wave energy converter model[21]. WEC-Sim itself is validated against several simulators and wave tank tests. The developed port-Hamiltonian simulation models the position of two floater bodies on a regular wave. The researchers chose the port-Hamiltonian framework since it is, numerically speaking, the most stable simulation mechanism.

1.5 System of research

The system considered in this research is displayed at the top of Figure 1.14. The system boundaries are set at the generation of waves and up to the PTO system.

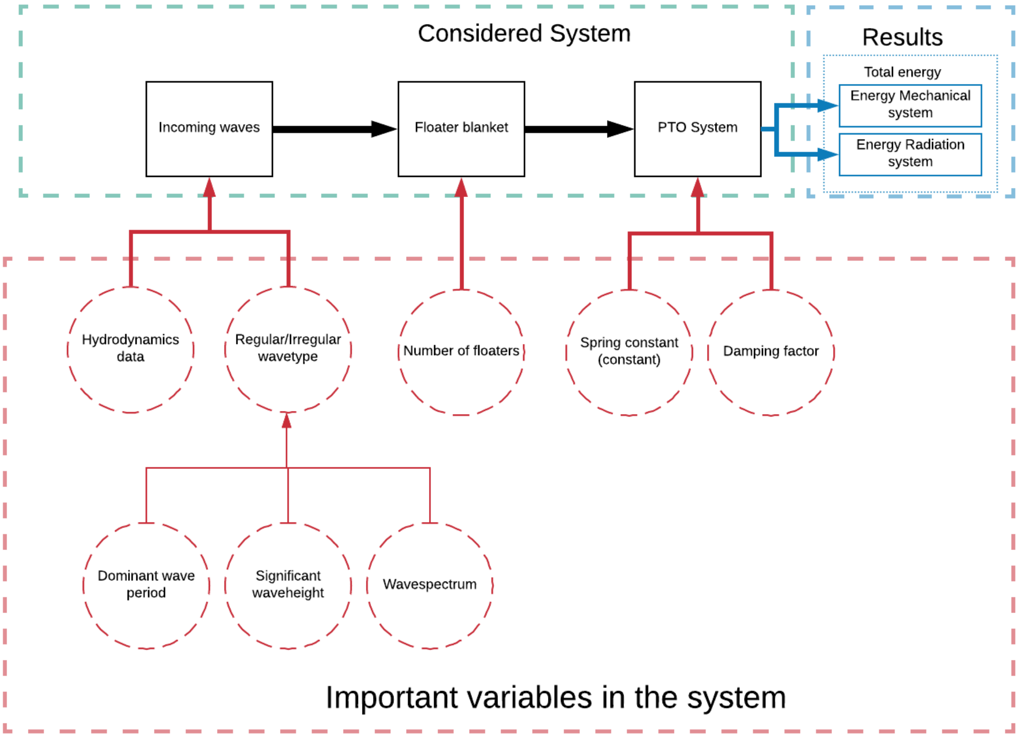

FIGURE 1.14: The researched system, the upper block shows the considered system, the block underneath the system defenition shows the variables that are important in this research. The results are shown exiting the system and consist of energy of the mechanical system, energy of the radiation system, together forming the total energy.

The *"considered system"* is to be modelled using the port-Hamiltonian framework. The, for this research, important variables are shown in the block below the system definition and are further elaborated. On the right of the considered system in the illustration are the results that are gained through this research. By calculating the values of the two Hamiltonians, that are presented in chapter 3, the energy of the mechanical system and the energy of the radiation system give information about the amount of energy is absorbed from the system.

1.5.1 Explanation of the variables

The variables of Figure 1.14

- The Hydrodynamical data
  The hydrodynamical data was obtained using NEMOH, this data is kept constant over every test, the developed model should accept these results as input.

- Regular/irregular wavetype
  The incoming waves used in the simulations can be of regular or irregular nature. The model should be able to incorporate different wave data sets as input, one at the time.

  - Dominant wave period
    Waves can be characterized by their dominant wave period. The model be able to encorporate a specific wavetype.
  - Significant wave height
    The significant waveheight differs per wavespectrum, the model should be able to accept different significant waveheigts as input, one at the time.
  - Wavespectra
    The wavespectrum caracterizes the waves generated, the model should be able to accept different wavespectra as input, one at the time.

- Number of floaters
  The number of floaters used in the floater blanket. In this research the number of floaters is 10, this number is kept constant, due to the influence on the time it takes to solve the problem. The model should accept any arbitrary number of floaters as input.
- Spring constant
  The spring constant is of an important influence to the PTO system, the value of this constant is kept at 0 throughout this research.
- Damping factor
  The damping factor is a design parameter of the PTO system, the model should allow the damping factor as an input, one at the time.

1.6 Research goal of this thesis

The problem statement is defined as:
"Current models of wave energy convertors cannot easily be controlled or extended. A tractable generic port-Hamiltonian model needs to be developed and validated for both regular and irregular wavetypes. Furthermore information is lacking on the power capture under regular and irregular waves subject to various linear PTO configurations."

The intent of this research is to solve this problem. This results in the following two goals:

1. **"The goal is to develop a generic port-Hamiltonian model for describing the wave interactions of the ocean grazer floater blanket that is subject to both regular and irregular wave."**
2. **"Evaluate the power capture under regular and irregular waves subject to various linear PTO configurations."**

When the first goal is achieved, the second goal focusses on giving insight into the effect PTO damping has on the power captured by the floater blanket.

1.6.1 Research questions

1. **How to define regular and irregular waves?**
With this question, regular parameters of different wavetypes are established, that are used in the model and presented in the research. This research question is answered in Chapter 2.

2. **What method can be used to simulate irregular waves?**
This question tries to answer what methods exist and what is neccessary to make irregular waves? This question is answered in Chapter 2.

3. **How can the total energy of the earlier defined system be calculated using the port-Hamiltonian framework?**
Both the system and the definition of total energy are defined using Figure 1.14. Using this question, this research tries to answer how the theory mentioned in [21] can be used to develop a generic model in the port-Hamiltonian framework. This question also guides in how the energy can be calculated and is answered in chapter 3

4. **What is the influence of PTO damping properties on the energy the system under regular and irregular waves?**
This research question is answered in chapter 4 and is connected to the second research goal. Answering this question is done by applying the results of earlier research questions.

1.7 Scientific contribution

This research's main scientific contributions are the theory behind, and the results of, the validated generic port-Hamiltonian model under regular and irregular wave scenarios, as wellass the results of the study on the power capture using various PTO configurations using a port-Hamiltonian framework under regular and irregular wave scenarios.

To my best of knowledge no other wave energy converter has been modeled in the port-Hamiltonian framework than the Ocean Grazer's and no earlier research featured more than two floaters in the port-Hamiltonian framework nor a wave energy converter modeled using irregular waves that are synthesized using white Gaussian noise using either FIR IIR or FIR and IIR bandpass filter combinations.

Regarding the ocean grazer project contribution; the generated irregular wave can be used for multiple other projects. The port-Hamiltonian model can be further expanded and used for other research.

Chapter 2

Irregular waves

When speaking about waves, a distinction can be made between regular and irregular waves. Regular waves have a constant wave period and wave height while irregular waves do not meet such characteristics. In this chapter, we will present the time-series modeling of realistic irregular waves which will be used in a later chapter

2.1 Waves

Generally speaking, waves are oscillations (or disturbances) of the water surface that can be observed in any type of water basin such as lakes, seas and oceans and are primarily generated by local wind, seismic oscillations of the earth due to seismic activities, atmospheric pressure gradients and gravitational attraction between the Earth, Sun and Moon. Minor influences are the capillary effect, the Coriolis effect, the Earths gravity and boundary effects like the influence seabeds[22][23].

2.1.1 Ocean waves

Ocean waves are mostly generated by wind blowing over the water surface, and the wave height may vary from capillary waves (or ripples, due to their shortwave period, as shown in Figure 2.1) to waves with roughly 30-meter wave height. The surface tension of water has in capillary waves a more substantial role [24]. These higher gravity waves will try to restore the equilibrium between the atmosphere and ocean. Wind-generated waves generally follow the direction of the winds, Swell waves are waves that are created by strong winds which blow for several hours, and have absorbed enough energy that they sustain in unidirectional winds.

2.1.2 Shallow water waves

Waves influenced by the rising sea floor, are named shallow water waves (or merely shallow waves), the free orbital movement is disrupted, and water particles no longer return to their original position as shown. As the water becomes shallower, below the swell becomes higher and steeper, ultimately assuming the familiar sharp-crested wave shape [22] as is shown in Figure 2.2.

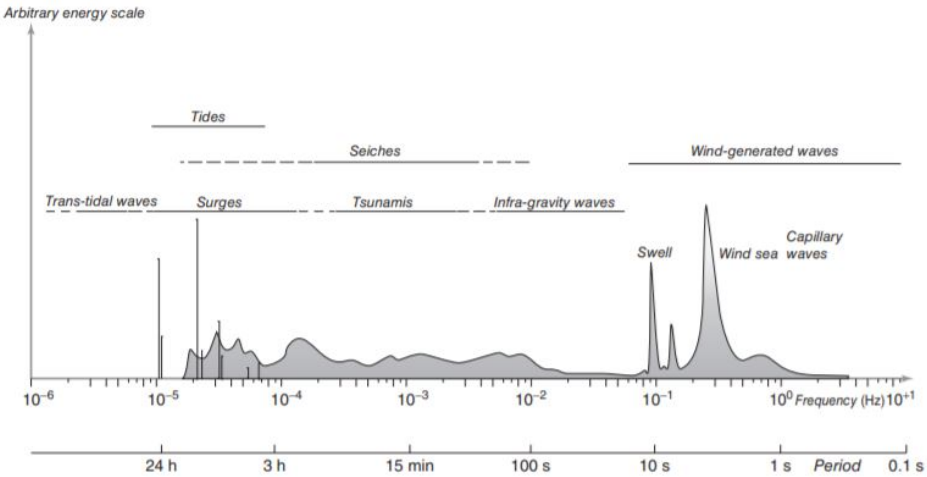

FIGURE 2.1: Illustration of various wave spectra according to the primary sources, it is taken from [23], copyright Cambridge University Press

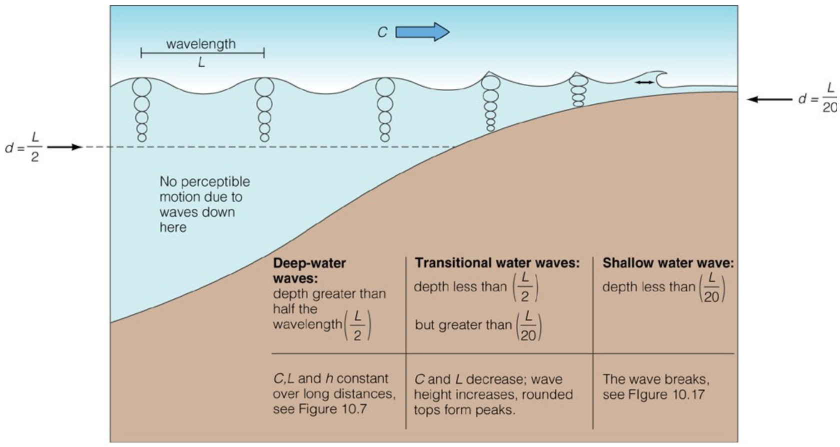

FIGURE 2.2: This figure illustrates that there are different waves depending on depth of the water and the wave lenght[25]. In particular; "deep water waves", "Transitional water waves" and "Shallow water waves".

2.2 Wave spectra

There are several parameters that specify how the charasteristics of wave, such as, wave height and wave period. In order to compute the average wave height, all waves will have to be classified into groups and counted on how often they have occurred over the measured interval, and divided over the total number of waves. Another way to classify the specific height is using the significant wave height, this method is the mean of the third largest waves and is used to classify wave spectra because the largest waves are often more significant than the smaller ones.

As the larger waves pack more energy, these are used to classify the waves at hand [26]. As is shown in Figure 5.1, the significant wave height is shown as the average of the third largest waves. We remark that the abscissa in the diagram is the wave height, and not the wave number/frequency.

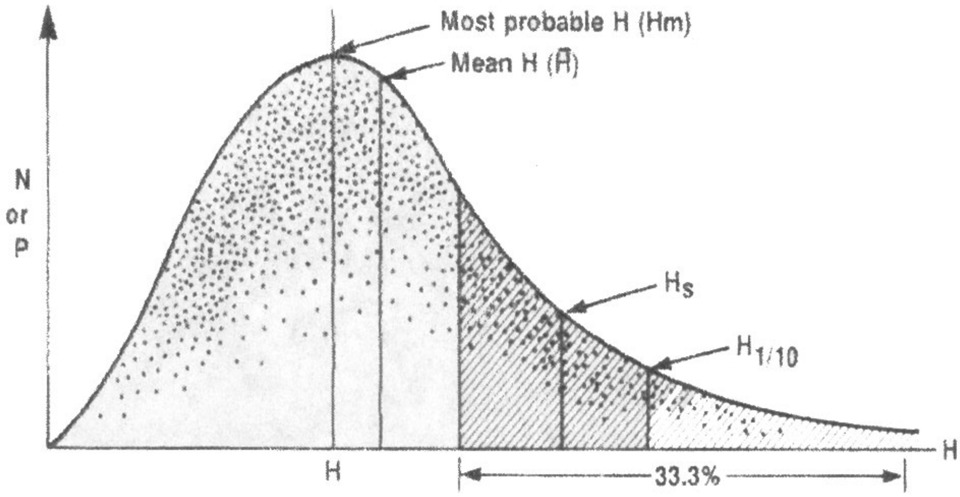

FIGURE 2.3: significant wave heigths [26], this figure shows the count (N) or chance (P) vs the waveheight (H), with the most probable wave (Hm), the averate waveheight, and the significant waveheight as defined in equation (2.1)

The significant wave height can be calculated using

$$H_{1/3} = \frac{1}{N/3} \sum_{j=1}^{N/3} H_j \tag{2.1}$$

in this equation, that is to be used on a dataset of waveheights sorted from heighest recorded wave to lowest recorded wave, $H_{1/3}$ is the significant wave height, N the total number of measurements, H_j is the one waveheight measurement from that dataset, j is the so-called waverank. Waverank 1 is the first highest wave, waverank 2 is the second highest wave. The equation thus uses the third highest waves to calculate the significant waveheight, as indicated by Figure 5.1.
Based on the linear model of waves with a narrow energy spectrum, research has shown that the heights of waves with a narrow spectrum obey the Rayleigh distribution [27]. Since the Rayleigh distribution has one scale parameter and no shape parameter, fixed ratios exist between the wave heights. To limit the calculation time the significant wave height can be approximated by dividing the root mean square by the fixed ratio; $H_s/H_{rms} \approx 1.416$. Where H_s is the significant wave height and H_{rms} is the root mean square of the wave[28].

One additional way to classify a wave is by the waveperiod, the calculation of the waveperiod is similar to that of the waveheight. This can be calculated by

$$T_{1/3} = \frac{1}{N/3} \sum_{j=1}^{N/3} T_j \tag{2.2}$$

in this equation, that is to be used on a dataset sorted from longest waveperiod to shortest waveperiod, $T_{1/3}$ is the significant wave height, N is the total number of records, T_j are the individual records, j is the so-called waverank. Waverank 1 is the longest waveperiod, waverank 2 is the second longest waveperiod.

There are several wave spectra known, and research still produces specific derivations and subtypes of several spectra. Previous research by the Ocean grazer group focussed on the following wave spectra[29]:

1. Pierson-Moskowitz
2. JONSWAP
3. Bretschneider

As these models were developed with a specific industry or science domain in mind (think of for instance ship design or shoreline engineering), the application of that particular wave spectra is also connected to those forms of industry and science domains. This influences the way the models differ by taking into account different sea states (swelling, retracting or fully developed) and what portion of varying wave types they take into account.

2.2.1 The Pierson-Moskowitz spectrum

The Pierson-Moskowitz spectrum is an empirical relationship between wind speed and wave height that was derived in 1964 using wind and wave data of British weather ships. It is only applicable to a developed, deep water sea and assumes that after some time the wind speed and wave height are in equilibrium. The Pierson-Moskowitz spectrum can mathematically be described by

$$S(\omega) = \frac{\alpha g^2}{\omega^5} \exp\left(-\beta\left(\frac{\omega_0}{\omega}\right)^4\right) \tag{2.3}$$

where $\omega = 2\pi f$, f is the wave frequency in Hertz, $\alpha = 8.1 \times 10^{-3}$, $\beta = 0.74$, $\omega_0 = g/U_{19.5}$ and $U_{19.5}$ is the wind speed at a height of 19.5m above the sea surface, the height of the anemometers on the weather ships used by [30].

2.2.2 The JONSWAP spectrum

Another well-known spectrum is the JONSWAP wavespectrum which is developed from observations by the JONSWAP(Joint North Sea Wave Observation Project) research group. This research project measured and analyzed data from July 1 to July 31, 1968, with some experiments redone from the first of August to the 15th of August, 1969 on the island of Sylt. The research was done using 13 research stations placed in a 160 km long line from the cost outward, using increasing intervals (1km, 2km, 4km, 6.5km, 9.5km, 14km up to 160km).

The purpose of the JONSWAP project was to derive wave patterns on a systematic basis, analyzing the data by spectral methods and parameterizing the resulting spectra in a Pierson-Moskowitz form. In general, the JONSWAP spectrum contains more peak energy than the corresponding Pierson-Moskowitz spectrum for the same values of α and f_o [31].When comparing the results of the research of Holthuijsen, Figure 2.1, the absence of capillary waves (around 1 Hertz according to [23]) makes this a primarily wind generated, developed, deep water seas. The JONSWAP spectrum can be found in a modified form, known as the TMA spectrum, to fit shallow water [32]. The JONSWAP spectrum can be applied to deep water, developed, coastal, wind generated seas[33][34]. The Jonswap spectrum can be expressed as

$$S(\omega) = \frac{\alpha_s H_s^2 \omega_p^4}{\omega^5} \exp\left(\frac{-5(\frac{\omega_p}{\omega})^4}{4} \lambda\beta_s\right) \tag{2.4}$$

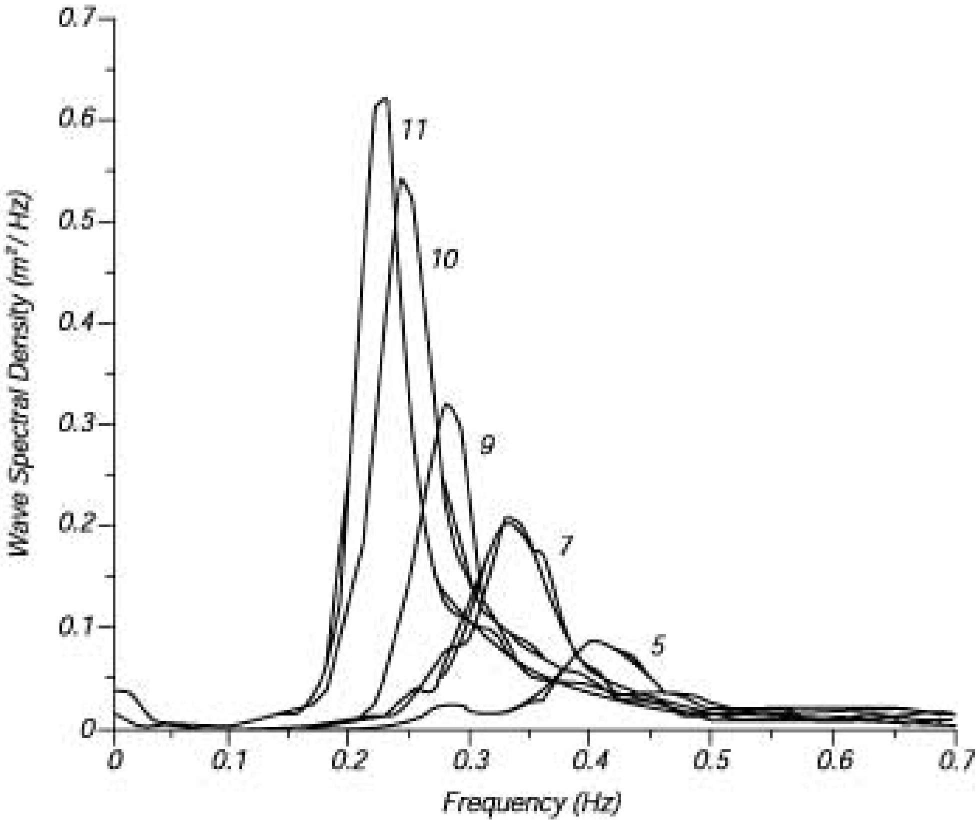

FIGURE 2.4: JONSWAP spectrum according to[33]

where λ is the peak enhancement factor, H_s is the significant wave height in meters, ω is the angular frequency in radians per second, ω_p is the peak frequency in radians per second. Research has shown that in the North Sea α aproximates 0.048, the peak enhancement coefficient, λ, ranges from 1 to 7, with an average value of 3.3, and $\sigma(\omega)$ equals between 0.07 and 0.09 depending on the frequency.

2.2.3 The Bretschneider spectrum

The Bretschneider spectrum, also known as the Modified Two-Parameter Pierson-Moskowitz Wave Spectrum, is a well-known wave spectrum and it is accepted by the ISSC (International Ship Structures Congress) and ITTC (International Towing Tank Congress) as a standard for seakeeping calculation and model experiments. For this reason, it is also known as ISSC or ITTC spectrum. It is primarily derived from model observations, combines developed sea states with a stronger influence of capillary waves. The Bretschneider spectrum can be regarded as being *"reasonably suitable"* for partially developed sea states [35]. For the choice of the spectrum, one must consider that the waves never approach a fully developed state. On the other hand, one can question if the Bretschneider spectrum, mostly derived from model observations[35], completely applies to a full-scale sea. ISSC recommends this spectrum therefore with observed periods. Due to the broad applicability of the Bretschneider spectrum, and its industry acceptence into standards, this spectrum is used in this research.
The Bretschneider spectrum can mathematically be described as

$$S(\omega) = \frac{5}{16}\frac{\omega_m^4}{\omega^5} H_{1/3}^2 e^{-5\omega_m^4/4\omega^4} \tag{2.5}$$

where ω is the radian frequency, ω_m is the modal frequency, and $H_{1/3}$ is the significant waveheight[36].
.

2.3 Wave synthesis

There are, according to [37], five main ways to synthesize irregular waves. We remark that there are also other ways that are expounded in [38] which are beyond the scope of this research.

1. Super-positioning of a finite number of sine waves;
2. Prototype measurement of wind wave time series;
3. Deterministic irregular wave trains (DSA method);
4. Non-deterministic irregular wave trains (NSA method);
5. The white noise digital filtering method (WNDF method);

The first method, super-positioning of a finite number of regular sine waves, is an often used method of simulating irregular waves. Some regular sine waves are stacked to produce a specific spectrum that can be closely matched, and while this method is adequate for estimating average power consumption[39][40], this method does have some drawbacks. According to well-cited research, this method does not correctly represent wave groupings correctly[41]. Waves itself, when observed in nature, are intrinsically random, approximating this using regular waves is criticized as it is not the same thing.
Prototype measurements of wind-wave time series, the second method, is using real-world data and scale this data required for input. This method is generally ineffective since it requires multiple, long-term, readings at the site of interest before it can be statistically representative[38].
The third and forth method have inaccuracies in the generated wavetrains because large waves are not accurately represented by linear wave theory, for the purpose of wave synthesis [42].
The last method, generating white Gaussian noise, passing this through a digital filter and amplifying the result obtained, is mentioned as being a 'better' way of generating irregular waves, due to its intrinsic 'real' randomness and is therefore used in this research.

2.4 Filtered noise-based irregular wave

Wave generation based on white Gaussian noise has been done in other research by generating white Gaussian noise, amplification and digital filtering using the wave spectrum of choice[43], [44]. In this research we consider the filtered noise-based irregular wave generation as shown in figure 2.5.

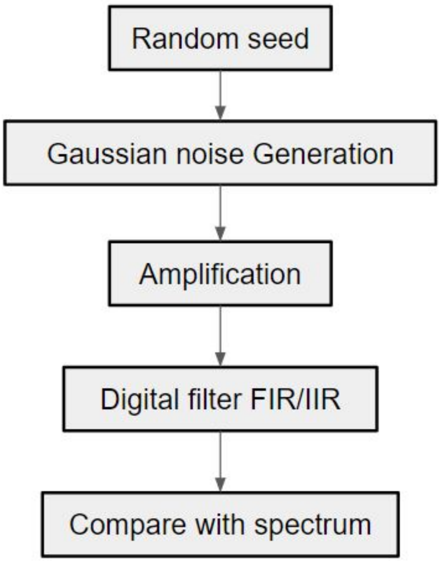

(A) Manual adjustment of the filter

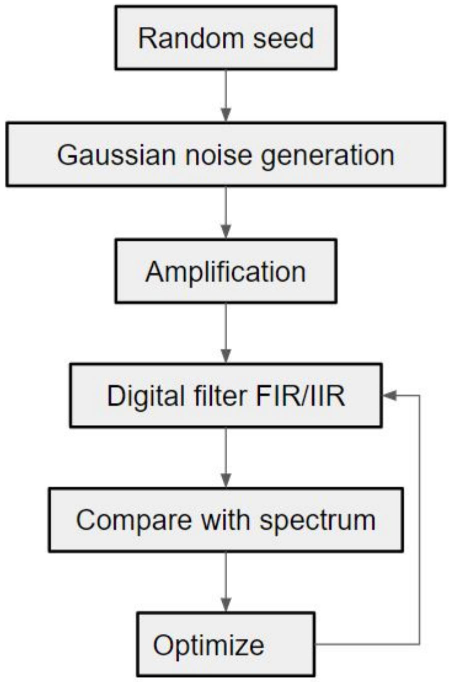

(B) Optimized adjustment of the filter

Figure 2.5: Wave generation using Gaussian noise

For the generation of the irregular wave in this research, an installation of Matlab, version 2017a is used alongside Matlab's digital filtering toolbox. In Matlab two methods of generating white Gaussian noise where implemented, one where a random seed is generated, amplified, filtered and compared with a spectrum, shown in Figure 2.5a, and one in addition of 2.5a an optimization step, that adjusts the digital filter to better match spectra. This method, shown in 2.5b, is used to generate parameters, these are used to control the filters in Figure 2.5a, that is used to produce the same irregular wave for further tests repeatedly.

2.4.1 Random seed and White Gaussian noise

A random time-series is said to be white noise if its autocorrelation series is an impulse time-series (with a non-zero elemnet only at the origin) and it has a probability distribution with zero mean and finite variance[45]. The reason this noise is called white is that the power spectral density is the same at all frequencies, analogy to the frequency spectrum of white light[46]. The basis for generating the white noise in the Matlab software is the "*randn*" function[47], this is a random number generator, that accepts a seed. The random seed generates the same random white noise sequence for repeated testing, within the boundary conditions sketched earlier. The number 124432221 is used throughout this research as the random seed.

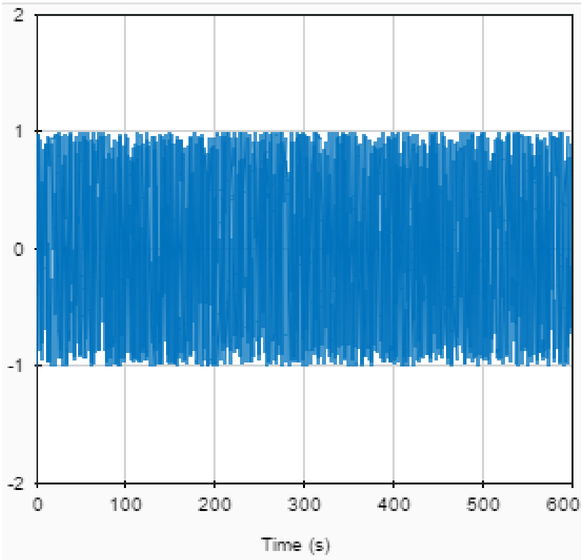

(A) Generated white noise; values over time

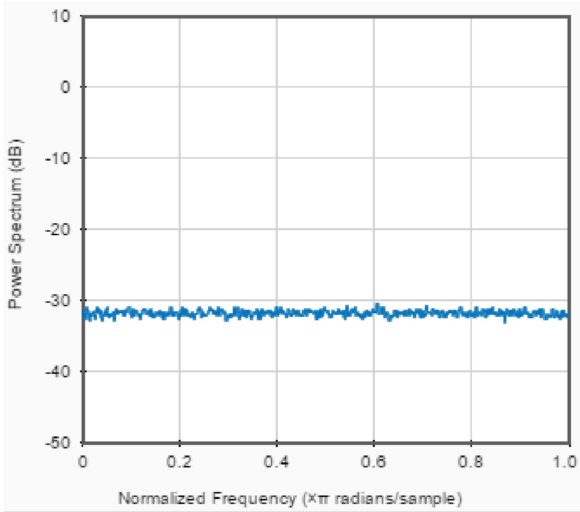

(B) Fourierspectrum of the generated white noise

Figure 2.6: White Gaussian noise generated using the number 124432221 as seed, 10000 samples, samplerate: 10 hz

As can be seen in Figure 2.6a the generated white noise is evenly distributed between 1 and -1, and with a mean of 0 and a finite variance. The power spectrum Figure 2.6b appears to be equal/more or less equally throughout the entirety of its power spectrum, and therefore we can speak of white Gaussian noise.

2.4.2 Amplification and Digital filtering

The white noise is then amplified uniformly to match the significant wave height of the wave spectrum. The digital filter in this research uses the Bretschneider wave spectrum. Based on the linear model of waves with a narrow energy spectrum, research has shown that the heights of these waves obey the Rayleigh distribution [27]. Since the Rayleigh distribution has one scale parameter and no shape parameter, fixed ratios exist between the wave heights, $H_s/H_{rms} \approx 1.416$. In this ratio H_s is the significant wave height and H_{rms} is the root mean square of the wave[28].
Since the connection between the amplification factor and the root mean square of the same wave heights is linear, this does not need solving, allowing flexibility to make waves as high as required.

A digital filter is designed by computing the time domain terms hi called filter coefficients. There are several methods of designing the filters, using Biesel functions for instance[48]. For this research, we focus on the FIR and IIR filters within Matlab, since Matlab is used for the port-Hamiltonian simulation. The difference between FIR (finite impulse response) and IIR (infinite impulse response) based filters is that the IIR filter contains an extra term in the difference equation that describes the output of these filters.

FIR filters have some advantages over IIR filters[47]; FIR filters can be, in general, more easily implemented into hardware and are always stable, and have a linear phase response[49]. IIR filters, on the other hand, can be implemented more efficiently[50].
The difference equations for FIR and IIR filters, for the input sequence $x[n]$ and output sequence $y[n]$ are, respectively, given by

$$y[n] = \sum_{k=0}^{M} h[k]x[n-k], \tag{2.6}$$

$$y[n] = \sum_{l=1}^{N} a_l y[n-l] + \sum_{k=0}^{M} b_k x[n-k], \tag{2.7}$$

where $h[k]$ is the impulse response, and a_l and b_k are the filter coefficients. The transfer functions in the z-domain for the FIR and IIR filter are, respectively,

$$H(z) = \sum_{k=0}^{M} h[k]z^{-k}, \tag{2.8}$$

$$H(z) = \frac{\sum_{k=0}^{M} b_k z^{-k}}{1 - \sum_{l=1}^{N} a_l z^{-l}} \tag{2.9}$$

For this research Matlab's filter toolbox is used to generate the filtercoefficients. For IIR and FIR are multiple filter types/subtypes available. This research uses an Equiripple type FIR filter, and a Butterworth IIR filter. These filter types are chosen for their general availability, and both have distinct magnitude responses. To match the spectrum a bandpass filter is used. This bandpass filter consists of a highpass and a lowpass filter and is set up as shown in Figure 2.7 as wel as the individual filters(Figure 2.8, Figure 2.9).

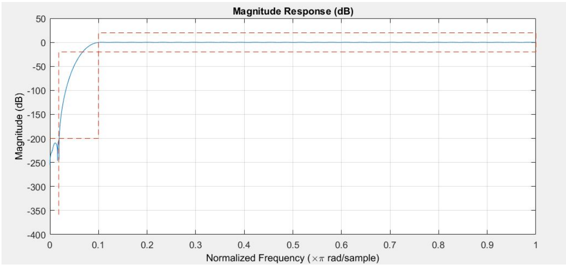

(A) Highpass Equiripple FIR filter, starting condition

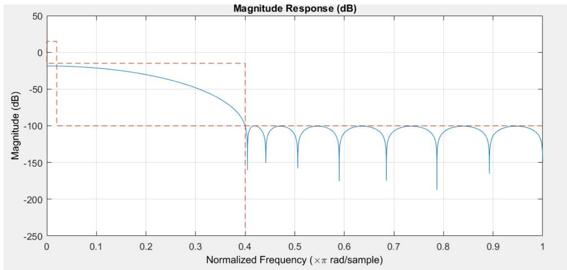

(B) Lowpass Equiripple FIR filter, starting condition

FIGURE 2.7: This illustration shows the individual components of the bandpass FIR filter in their starting condition

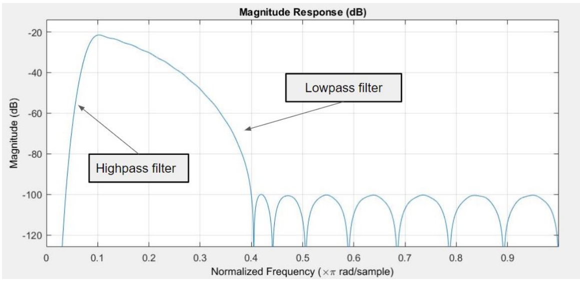

(A) Magnitude response FIR Bandpassfilter

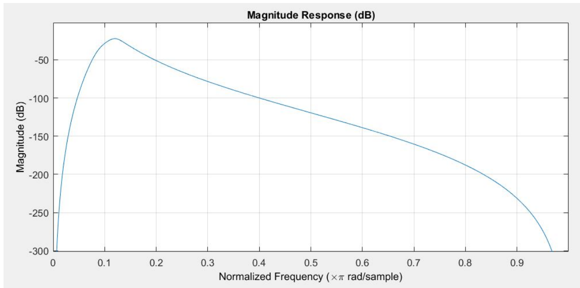

(B) Magnitude response IIR Bandpassfilter

FIGURE 2.8: Filter setup of the bandpass filters, showing the result of a manually fitted bandpass filter

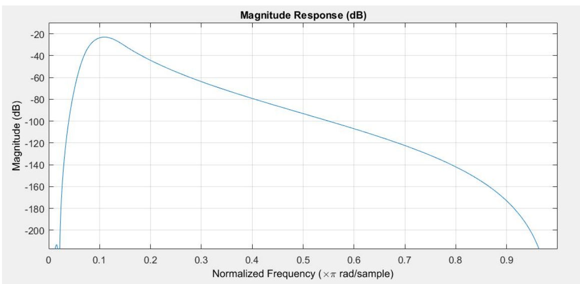

(A) Magnitude response FIR/IIR hybrid Bandpassfilter

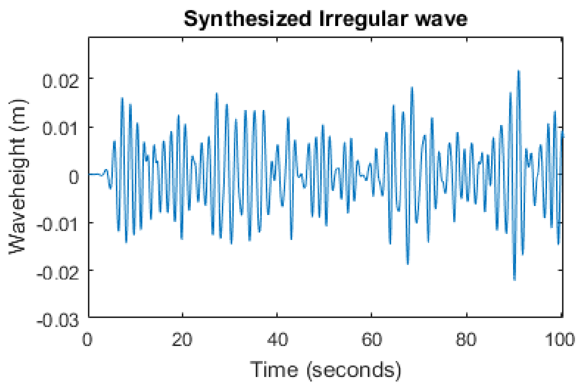

(B) Example of a synthesized wave form, the signal is ramped up during the first five seconds of the simulation to make sure any solvers in the simulation can converge. Since the filters are adjusted to fit a specific wavespectrum, the resulting synthesized waves are different in minor details.

FIGURE 2.9: Filter setup of the FIR/IIR bandpass filter, with the result of filtering

2.4.3 Optimization

Matlab's optimizer, "fmincon", was used to minimize the objective function. The objective function was defined as

$$y(\omega) = \int_0^1 (f(\omega) - k(\omega))^2 d\omega \tag{2.10}$$

which is the sum of the difference between the desired spectrum and the actual value squared In this function, the $f(\omega)$ is the output of the actual spectrum at frequency ω, $k(\omega)$ is the output of the desired spectrum at frequency ω, by squaring this any negative differences become positive. Frequency ω is the frequency in π *radians/sample*. The sample-rate used in this experiment was 10 samples per second. This objective function focusses on finding a fit with regard, to the filter parameters, the amplification factor is not part of the results, since the root mean square of the wave is linear with the wave height, this allows one to synthesize waves with whatever significant wave height. In the Table 2.1 shown below, boundary conditions can be seen.

Table 2.1: Optimizer boundary conditions

Nr	Parameter	Boundary conditions
1	Highpass Filter stopband frequency (normalized)	$0 < x < 1$ $\pi rad/sample$
2	Highpass Filter passband frequency (normalized)	$0 < x < 1$ $\pi rad/sample$
3	Lowpass Filter stopband frequency (normalized)	$0 < x < 1$ $\pi rad/sample$
4	Lowpass Filter passband frequency (normalized)	$0 < x < 1$ $\pi rad/sample$
5	Highpass stopband attenuation	$0 < x < 200$ dB
6	Highpass passband ripple	$0 < x < 200$ dB
7	Lowpass stopband attenuation	$0 < x < 200$ dB
8	Lowpass passband ripple	$0 < x < 200$ dB

Matlab's parameters, like step-size and stopping conditions, were left default. For the generation of the FIR filter, the following parameters where found; as can be seen in Table 2.3.

Table 2.2: Solver results, first experiment Fir bandpass filter, FIR/IIR hybrid, IIr bandpassfilter

Parameter	Highpass Filter	Lowpass Filter
filtertype	FIR Equiripple	FIR Equiripple
filterordermode	Minimum	Minimum
stopband frequency	0.018 $\pi rad/sample$	$0.5\pi rad/sample$
passband frequency	$0.689\pi rad/sample$	$0.08\pi rad/sample$
stopband attenuation	200 dB	100 dB
passband ripple	60 dB	20 dB

Parameter	Highpass Filter	Lowpass Filter
filtertype	FIR Equiripple	IIR Butterworth
filterordermode	Minimum	Minimum
stopband frequency	$0.022\pi rad/sample$	0.5 $\pi rad/sample$
passband frequency	$0.144\pi rad/sample$	$0.08\pi rad/sample$
stopband attenuation	200 dB	200 dB
passband ripple	1 dB	1 dB

Parameter	Highpass Filter	Lowpass Filter
filtertype	IIR Butterworth	IIR Butterworth
filterordermode	Minimum	Minimum
stopband frequency	0.018 $\pi rad/sample$	$0.55\pi rad/sample$
passband frequency	$0.1\pi rad/sample$	$0.05\pi rad/sample$
stopband attenuation	200 dB	100 dB
passband ripple	40 dB	30 dB

The resultant wave spectra are more or less comparable, as can be seen in Figure 2.10. The IIR filters magnitude response (Figure 2.9a) appears to become more squared in form when the stopband frequency and the passband frequency are close together. This is particularly an issue with the highpass filter. In order for the IIR highpass filter to recieve a rounder form, the difference between passband and stopband frequencies is increased, as shown in Table 2.3. This in turn required the signal to be amplified (using the passband ripple) and Matlab's solver took longer to find a feasible solution. The FIR solution or the FIR/IIR hybrid, where both highpass filters are following the FIR principle, do not experience that problem. These happen to adhere better to the spectrum as can be seen in Figure 2.10. The claimed performance difference is not noticable in matlab, both FIR and IIR algorithms in the tested timeframe, 5500 datapoints, 550 seconds of actual wave time, are filtered fast, with small differences between IIR and FIR techniques, IIR filters, on average, rougly 1/8th of a milisecond faster, while the setup time is more then double that of an FIR filter. In terms of fit, the best filter is the FIR filter, second FIR/IIR, third IIR. During the optimization we found that the optimizer's stepsize became larger than the frequency it was trying to manipulate and that there are multiple minima, due to the overlap of the two filters, and the passband attenuation that the solver is allowed to change.

Table 2.3: Five timed runs, Filter setuptime vs Filter execution time, IIR is fastest to execute, but slowest to setup, FIR is slowest to execute, fastest to setup. The FIR/IIR hybrid is inbetween.

Filter algorithm comparison			
Parameter	IIR	FIR/IIR Hybrid	FIR
Setuptime run 1 [ms]	501.9	308.3	204.3
Setuptime run 2 [ms]	560.8	295.2	219.9
Setuptime run 3 [ms]	503.5	280.1	213.1
Setuptime run 4 [ms]	526.2	333	237.4
Setuptime run 5 [ms]	495.9	280.5	223.4
Mean [ms]	517.7	299.4	219.6
Standard deviation [ms]	24	20	11
Executiontime run 1 [ms]	7.2	8.1	7.8
Executiontime run 2 [ms]	7.7	8.3	7.3
Executiontime run 3 [ms]	6.2	7.3	8.2
Executiontime run 4 [ms]	8.1	8.3	7.9
Executiontime run 5 [ms]	6.1	7.7	9.6
Mean Executiontime [ms]	7.06	7.94	8.16
Deviation in Executiontime [ms]	0.8	0.39	0.78

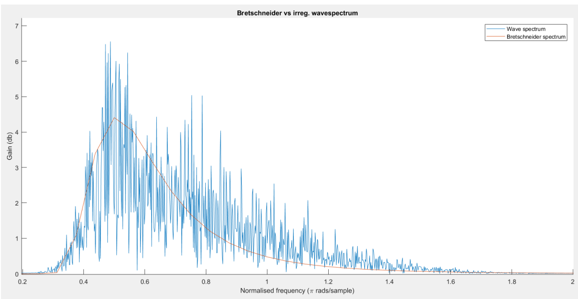

(a) Magnitude response shown in blue, thin red line shows Bretschneider spectrum, FIR filter

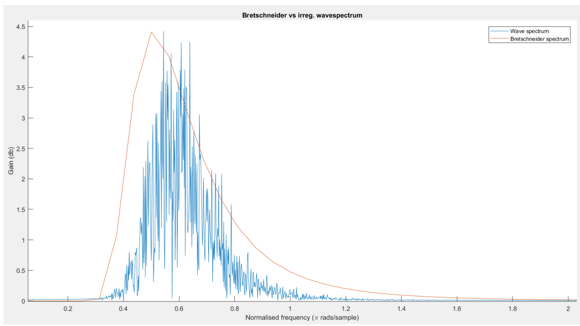

(b) Magnitude response shown in blue, thin red line shows Bretschneider spectrum, IIRfilter

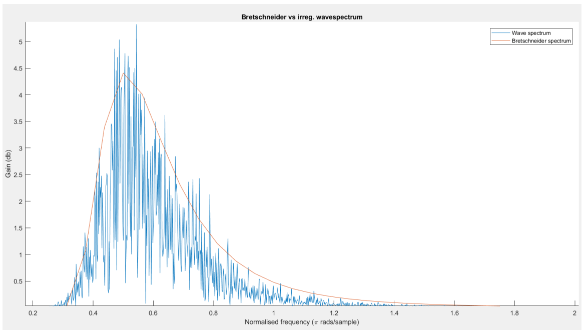

(c) IIR/FIR hybrid filter, Magnitude shown in blue, thin red line shows Bretschneider spectrum,

Figure 2.10: Spectrum result

Chapter 3

Model Introduction

3.1 Modeling process

The modeling process of the floater array system, of the Ocean Grazer WEC, consists of (1) modeling the wave-structure interaction between the wave surface and the floating bodies; (2) floater-to-floater interaction; and (3) floater-to-PTO interaction. For this purpose, the well-known Cummins equation will be used as the basis of the modeling. The reason for using this equation is that the Cummins equation is an approach for the time-domain representation of the first-order radiation and diffraction of a floating body. This equation takes into account information from the buoyancy and excitation forces (1) produced by contact between the wave surface and the floater body, the waves moving the structure and radiation forces (2) produced by the movement of the structure itself. Other external forces, such as those produced by moorings and in this case, PTO systems (3), can also be included in the equation.

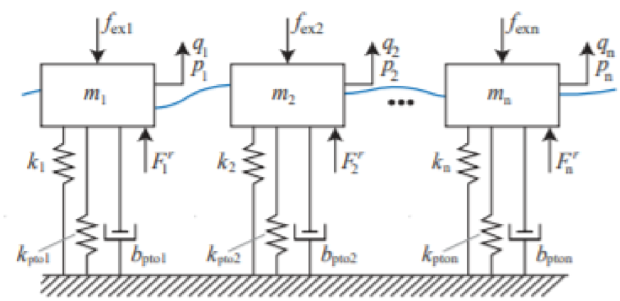

FIGURE 3.1: Modeling principle of multi-floating body system [51]

3.2 Cummins equation

The Cummins equation that was proposed by WE Cummins in 1962[52], describes the behavior of floating bodies. The dynamics of a floating body connected to a PTO unit, in one degree-of-freedom (1-DoF) can be described by

$$m\ddot{q}(t) = f_b(t) + f_r(t) + f_{\text{ex}}(t) + f_{\text{pto}}(t) \tag{3.1}$$

where t represents time, m is the floater mass, q is the floater displacement, f_b is the buoyancy restoring force, f_r is the radiation force due to its structure motion, f_{ex} is the excitation force, and f_{pto} is the PTO force.

3.2.1 The buoyancy force

The first force component of the Cummins equation is the buoyancy restoring force that is described by Figure 3.3. In buoyancy, the mass does not directly play a part. However, the mass determines

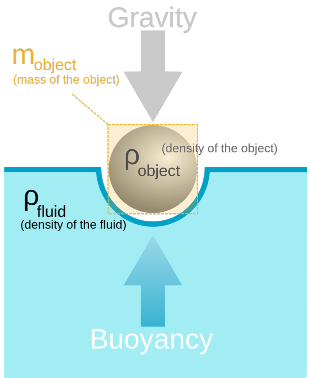

FIGURE 3.2: The principle of buoyancy restoring forces, copyright Wikimedia

how much the floater is initially submerged, due to the gravity acting upon the object, determining the density. The buoyancy restoring force can be expressed as

$$f_b(t) = -\rho_{\text{sw}} g A_f q(t) = -kq(t). \tag{3.2}$$

where ρ_{sw} is the sea water density, g, is the gravitational acceleration constant and $A_f q$ is the volume of submerged part of the body.

3.2.2 The radiation force and excitation force

The radiation and excitation forces are the main hydrodynamics component of the Cummins equation. The radiation forces are forces that are formed by the motion of floater bodies and thus have an influence on the other nearby floating bodies. One can imagine these radiation forces in a pond as rings around a bobbing object in the water. If there is a second object floating in the pond, it will move due to the radiation forces formed by the first object. These interactions happen on a larger scale in the ocean grazer.
The radiation force and the excitation force are given by:

$$f_r(t) = -m_\infty \ddot{q}(t) - \varphi_r(t) * \dot{q}(t), \tag{3.3}$$
$$f_{\text{ex}}(t) = \varphi_{\text{ex}}(t) * \eta(t) \tag{3.4}$$

where $m_\infty > 0$ is the constant added mass at infinite frequency, $\eta(t)$ is the sea-wave elevation, φ_r and φ_{ex} are the IRF of the radiation force and the excitation force, respectively, and $*$ denotes the convolution operator.
The radiation and excitation forces are frequency dependent. However, in this work, we only take the added mass at an infinite frequency and use the IRF instead of frequency response function in order to simplify the time-domain simulation. These components are usually obtained through numerical tools that are specifically designed for solving hydrodynamics problems, for instance, Aquaplus[53] and NEMOH [54].

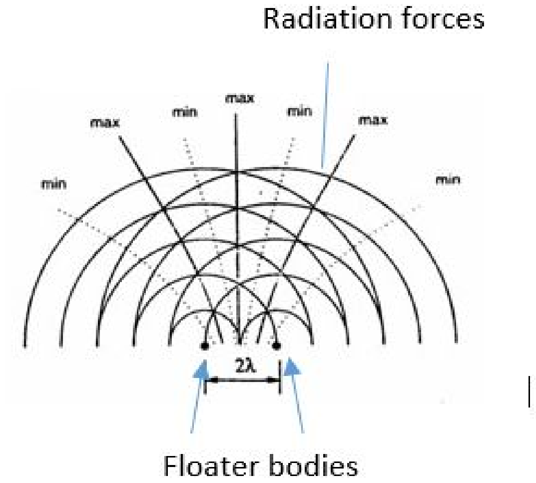

FIGURE 3.3: The principle of Radiation forces, one body radiates, others get irradiated, but radiate themselves as well, copyright Springer AG

3.2.3 Linear PTO forces

In this work, the PTO force, f_{pto}, is described using simple mechanical coupling elements, such as linear springs and dampers.

$$f_{\text{pto}}(t) = k_{\text{pto}} q(t) + b_{\text{pto}} \dot{q}(t), \tag{3.5}$$

where the stiffness constant $k_{\text{pto}} > 0$ and damping constant $b_{\text{pto}} > 0$.

3.2.4 Multiple Floaters

In order to describe the behavior of the multi-floater system, the generalized variables that correspond to the variables used in equations (3.4), (3.3), (3.2) and (3.5) are introduced, namely, the diagonal matrices M ,K, B_{pto}, and K_{pto} of dimension $n \times n$ corresponding to the floaters mass, buoyancy force coefficient, PTO damping coefficient and PTO stiffness coefficient, respectively. M_∞ is a positive definite matrix indicating the added mass at infinite frequency, Q is the displacement vector, $\mathcal{F}^r$ is generalized convolution term of the radiation component and F_{ex} is the excitation force vector. Then the generalized Cummins' equation for a multi-floater system with linear power take-off can be written by

$$(M + M_\infty)\ddot{Q} + \mathcal{F}^r + B_{\text{pto}}\dot{Q} + (K + K_{\text{pto}})Q = F_{\text{ex}}. \tag{3.6}$$

3.3 port-Hamiltonian modeling of floaters array

In port-Hamiltonian systems, different elements are interfaced using energy, listing their interactions in a Port-based system. This port-based system is made up of energy storing, dissipating and routing elements. The Hamiltonian is a matrix in which all energy is organized. The interactions are organized in some components, connected by flows and efforts (f and e respectively) shown in the equations 3.7

In this work, we are interested in a particular case of port-Hamiltonian model described by the following equations.

$$\begin{cases} \dot{x} &= [J(x) - R(x)]\frac{\partial H(x)}{\partial x} + G(x)u, \\ y &= G^T(x)\frac{\partial H(x)}{\partial x}). \end{cases} \tag{3.7}$$

Here $J(x)$ is a skew-symmetric interconnection matrix, $R(x)$ is a positive semi-definite dissipation, matrix $G(x)$ represents the input matrix and $H(x)$ is the Hamiltonian or the energy function of the system.

3.3.1 From Cummins equation to port-Hamiltonian

In order to construct the port-Hamiltonian modeling, the Cummins equation can be described as an interconnection between mechanical and radiation subsystem depicted in Figure 3.4.

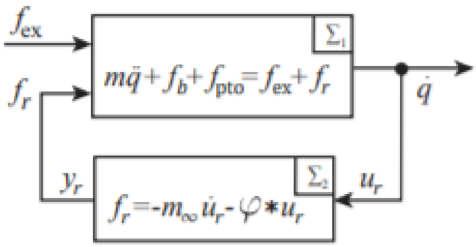

FIGURE 3.4: Schematic overview of the Cummins' equation where Σ_1 describes the mechanical component and Σ_2 describes the radiation component of the Cummins' equation in a different subsystem [51].

Following Figure 3.4 and using equation (3.6), first we can reformulate the mechanical system Σ_1 into port-Hamiltonian by introducing the state variable $x_1 = \left[\begin{smallmatrix} Q \\ P \end{smallmatrix}\right]$ with $P = M\dot{Q}$ and the Hamiltonian function

$$H_1(x_1) = \frac{1}{2}P^\top M^{-1}P + \frac{1}{2}Q^\top(K + K_{\text{pto}})Q. \tag{3.8}$$

Using this Hamiltonian function, the port-Hamiltonian model of the mechanical system, Σ_1, is given by:

$$\begin{cases} \dot{x}_1 &= (J_1 - R_1)\frac{\partial H_1(x_1)}{\partial x_1} + \begin{bmatrix} 0_{n\times n} \\ I_{n\times n} \end{bmatrix} u_1 \\ y_1 &= \begin{bmatrix} 0_{n\times n} & I_{n\times n} \end{bmatrix} \frac{\partial H_1(x_1)}{\partial x_1} \end{cases} \tag{3.9}$$

In this model, the input u_1 is given by $F_{\text{ex}} + F_r$, the output y_1 is the velocity $\dot{Q}$ and the matrices $J_1 = \left[\begin{smallmatrix} 0 & I \\ -I & 0 \end{smallmatrix}\right]$ and $R_1 = \left[\begin{smallmatrix} 0 & 0 \\ 0 & B_{\text{pto}} \end{smallmatrix}\right]$. I is the identity matrix. Earlier research has shown that the convolution term of the radiation system $\Sigma_r : \dot{Q} \mapsto -\mathcal{F}^r$ can be approximated by a port-Hamiltonian model using the state variables Z, Hamiltonian function $H_r(Z)$, interconnection and damping matrices J_r and R_r, respectively, and the input matrix G_r[51]. where $x_2 = \left[\begin{smallmatrix} Z \\ P_\infty \end{smallmatrix}\right]$ with $P_\infty = M_\infty\dot{Q}$. The Hamiltonian function will subsequently be:

$$H_2(x_2) = \frac{1}{2}P_\infty^\top M_\infty^{-1}P_\infty + H_r(Z) \tag{3.10}$$

The port-Hamiltonian of Σ_2 will then be

$$\begin{cases} \dot{x}_2 &= \left(\begin{bmatrix} J_r & G_r \\ -G_r^\top & 0 \end{bmatrix} - \begin{bmatrix} R_r & 0 \\ 0 & 0 \end{bmatrix} \right) \frac{\partial H_2(x_2)}{\partial x_2} + \begin{bmatrix} 0_{n\times n} \\ I_{n\times n} \end{bmatrix} u_2 \\ y_2 &= \begin{bmatrix} 0_{n\times n} & I_{n\times n} \end{bmatrix} \frac{\partial H_2(x_2)}{\partial x_2} \end{cases} \tag{3.11}$$

[51] has shown that both Σ_1 and Σ_2 are passive systems, the time-derivative of their respective hamiltonians does not exceed the feedrate, thus their interconnection is also passive, that is $\dot{H}_1 + \dot{H}_2 \leq \dot{Q}F_{\text{ex}}$.

The energy of the radiation system, Σ_2, consists of two parts a storage part, and a kinetic part. This can be mathematically expressed by

$$H_{storage}(x_2) = H_r(Z) = \frac{1}{2} Z^\top W Z \tag{3.12}$$

$$H_{kinetic}(x_2) = \frac{1}{2} P_\infty^\top M_\infty^{-1} P_\infty = \frac{1}{2} \dot{Q}^\top M_\infty \dot{Q} \tag{3.13}$$

where $H_{storage}$ and $H_{kinetic}$ are Hamiltonians, W is a positive definite matrix, and Z is the matrix with state variables, introduced earlier.

The port-Hamiltonian model will be used for simulations, the energy of the mechanical system, Σ_1, expressed by $H_1$and the energy of the radiation system Σ_2, expressed by H_2, together form the total energy in the system. The energy of the radiation system

3.4 Calculation speed vs Precision

Significant for the simulation of the port-Hamiltonian model is the tradeoff of computational speed at which the model can be calculated versus the precision that the results require. The simulations can, for instance, be set up in such manner that the calculation of the port-Hamiltonian simulation model becomes time-consuming. During this research significant effort was made in reducing the total simulation time.

Frameworks on computational efficiency found in research often focus on a specific embedded system or focus on the fastest implementation of a specific algorithm or subroutine. General guidelines for computational efficiency[55] advice to enhance parallelism, minimize the instructions needed for different tasks or distribute and minimize the dependency on specific hardware components. The current model is not bound to a specific hardware platform, and while Matlab supports limited parallelism, the most gain can be expected from minimizing execution and memory needed for tasks.

One of the calculation time gains was achieved through the reduction of the order of the approximation of the radiation forces. Earlier work used a fixed order that dictates the size of the calculation matrix. Since this matrix is multiplied with other matrices, any increase in size will expand subsequent calculations. The results presented in Table 3.1 are showing the effect of the order of the approximation of the radiation forces to the time it takes for a solver to converge.

TABLE 3.1: This table shows how the different solver order influence the time needed to solve a problem, vs the error and the number of function evaluations.

Solver order	Time 1 [s]	Time 2 [s]	Iterations [-]	Function evaluations [-]	Remaining error
1	2.1531	2.3790	45	713	8.610017×10^3
2	2.2932	2.4270	96	2815	4.707791×10^3
3	4.7397	4.7424	174	7185	3.149808×10^3
4	11.3714	11.6082	316	16820	2.228653×10^3
5	20.1191	20.2834	402	26012	2.228679×10^3
6	20.5428	21.5551	307	23614	1.206851×10^3
7	50.7578	51.9610	613	54542	9.396140×10^2
8	45.7593	45.8947	400	40285	9.371351×10^2
9	59.8793	60.1419	449	50670	6.042212×10^2
10	79.9711	81.2391	488	60886	5.074643×10^2
11	75.3210	73.4639	392	53729	4.304708×10^2
12	96.7308	100.1854	453	67289	4.306624×10^2
13	249.9939	249.9939	1000	150004	3.271893×10^2

In this table the solver order is an indication of size of the calculation matrix, Time 1 represents the first time sample done and Time 2 is the mean of three subsequent time measurements. The time measurements were done using Matlab's tic-toc mechanism and deviate due to computation speed of the electronics involved. The iterations are the number of successive steps the solver takes toward the minimization of the objective function; the number function evaluations are the number of calculations done in the feasible region. We can observe that the increased matrix size increases the accuracy of estimation by reducing the remaining error, that is the remainder of the objective function after

Data: hydrodynamic coefficients, a guessvalue
Result: fastest converging order of radiation approximation
int x_1=$guessvalue$;
solutions=[]struct;
for $j \leftarrow x_1$,$i \leftarrow 1$ **to** $j \leq 20,\ i \leq 4$ **do**
    solutions(j)=Fit the obtained IRF with passive transfer function with a small amount of iterations;
    if $residual(i) > residual(i-1)$ **then**
        $i++$;
        continue;
    else
        $i--$
    end
end
x_2=find the best performing solution in the solutions;
return x_2;

Algorithm 1: This algorithm, tries to compute the best performing order of the approximation of the radiation energy by trying several orders

minimization. For this purpose, that is, to speed up the simulation while maintaining precision, we propose an algorithm to explicitly choose the order of the radiation forces.
Using algorithm 1, the simulation can be ran faster. Since matrix multiplication is essential for the port-Hamiltonian simulation, any change in matrix dimension will affect the total computational efficiency due to inherited influence. In this work, further efficiency gains were achieved by exporting and importing variables that would give the same intermediate results. This resulted are, case[1] dependent, reduction of the calculation time from 4 hours, 32 minutes, 22 seconds, to 19 minutes, 52 seconds [2].

[1]10 floaters under a regular wave with an initial wave sample rate of $10Hz$, for a total of 100 seconds.
[2]Using a Lenovo P50, with an I7-7700HQ processor, 32 Gb of RAM, M2 256gb SSD, other results may vary.

Chapter 4

Simulations, analysis and validation

4.1 Simulation procedure

Several simulations were conducted using the port-Hamiltonian model. In these simulations, the damping constant is varied under the regular and irregular wave. The output of these simulations are the floater displacements and the results of the port-Hamiltonian model; energy of the mechanical system, energy of the radiation system energy of the kinetic part of the radiation system

The following experiments are defined:

TABLE 4.1: The following parameters where used in the experiment.

Experiment	Description	Dampening constant$[kg/s]$
1	Earlier Ocean Grazer experiments [21]	1.1530×10^6
2	Ocean Grazer experimental setup scaled [56]	1.6526×10^4
3	No damping	0
4	Sweep experiment	1×10^2
5	Sweep experiment	1×10^4
6	Sweep experiment	1×10^5
7	Sweep experiment	1×10^6
8	Sweep experiment	1×10^7
9	Sweep experiment	1×10^8

1. **Ocean Grazer experimental setup scaled**
   The first experiment uses the findings of experimental data on the Ocean Grazer's experimental setup, [56]. In this research the damping coefficient applies to $5m$ pipe-length, to provide compatibility with the other experiments this is linearly scaled to $100m$ pipe-length.

2. **Earlier Ocean Grazer experiments**
   This experiment uses the damping coefficient used in earlier Ocean Grazer research [21][51][57].

3. **No damping**
   This experiment forms the control experiment; the model follows the input wave and the model shows an ideal scenario.

4. to 9. **Parameter sweeps**
   The goal of the sweep is to show the influence of a parameter is to the model.

The following general parameters are used in the experiments:

TABLE 4.2: The following parameters where used in the experiment.

Property	Regular wave	Irregular wave
Exitation solver order	8	8
Estimated pipelength	$100m$	$100m$
Significant wave-height	$4m$	$6.22m$
Wave-period	$10s$	Bretschneider spectrum
Time-step dt	$0.01s/step$	$0.01s/step$
Water density	$1025kg/m^3$	$1025kg/m^3$
Floater cross-sectional area	$49m^2$	$49m^2$
Body mass	$45000kg$	$45000kg$
Hydrostatic restoring force coefficient	4.9271×10^{-5}	4.9271×10^{-5}
Working fluid viscosity	$0.0734Pa \times s$	$0.0734Pa \times s$
Separation between piston and cylinder	$400 \times 10^{-6}m$	$400 \times 10^{-6}m$
PTO piston radius	$0.01m$	$0.01m$
PTO piston height	$0.01m$	$0.01m$

For the irregular wave, the simulation uses the FIR/IIR irregular wave following the values of chapter3. This experiment uses the hydrodynamics data that was obtained using NEMOH.

The following experimental setup is used;

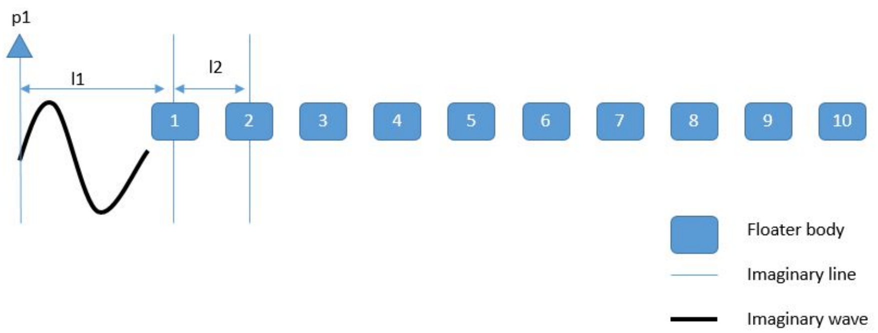

FIGURE 4.1: The following experimental setup was used; p1 is the point where waves are generated, l1 an offset added to make WEC-sim comparable to the port-Hamiltonian simulation, l2 is the distance between floaters.

The 10 floaters are positioned in a row. Wave generator p1 generates either a regular or irregular wave. After the wave travels distance l1, the wave hits the first floater. The distance between each subsequent floater is l2. For the experiments $l1 = 0m$[1].

[1] For the validation this l1 is of a dynamic length but based on WEC-Sim. In WEC-Sim cannot handle a value of $0m$, and its specific value it might be depending on an ODE Time-step

4.2 Simulation results

Using the parameters provided in Table 4.2 and 4.1, the following results were generated, (1) displacements, (2) energy of the Kinetic subsystem (a subsystem of the radiation system), (3) energy of the Storage subsystem (a subsystem of the radiation system), (4) energy of the radiation system, (5) Energy of the mechanical system and (6) energy of the total port-Hamiltonian system.

The results of the Ocean Grazer and the sweep, experiments 1-3 and 3-9, are presented in different graphs to more distinctively present the results.

4.2.1 Displacements

In Figure 4.2 the displacements of body 1 are shown for the regular wave.

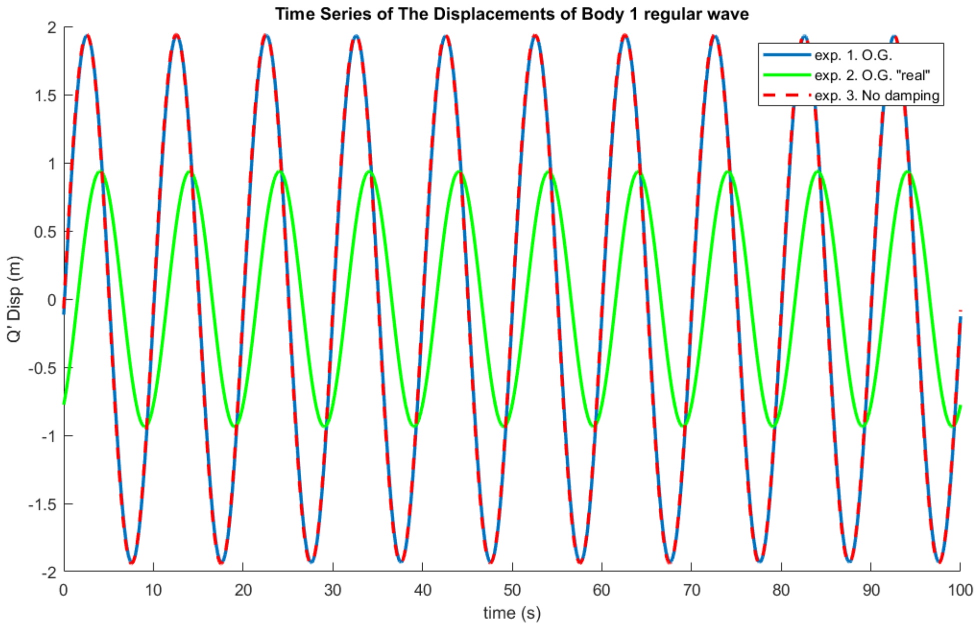

FIGURE 4.2: In this illustration the displacements of body 1 for experiments 1-3 under regular wave

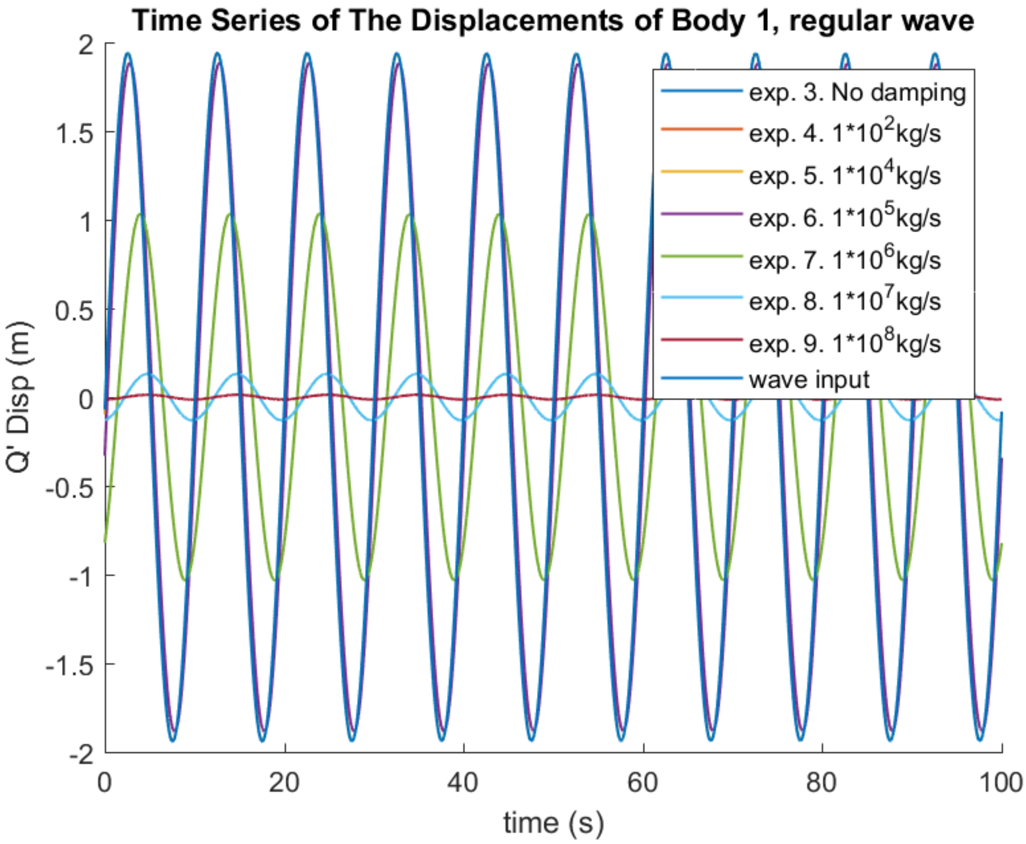

FIGURE 4.3: Sweep, Regular wave, regular wave, displacement of body 1

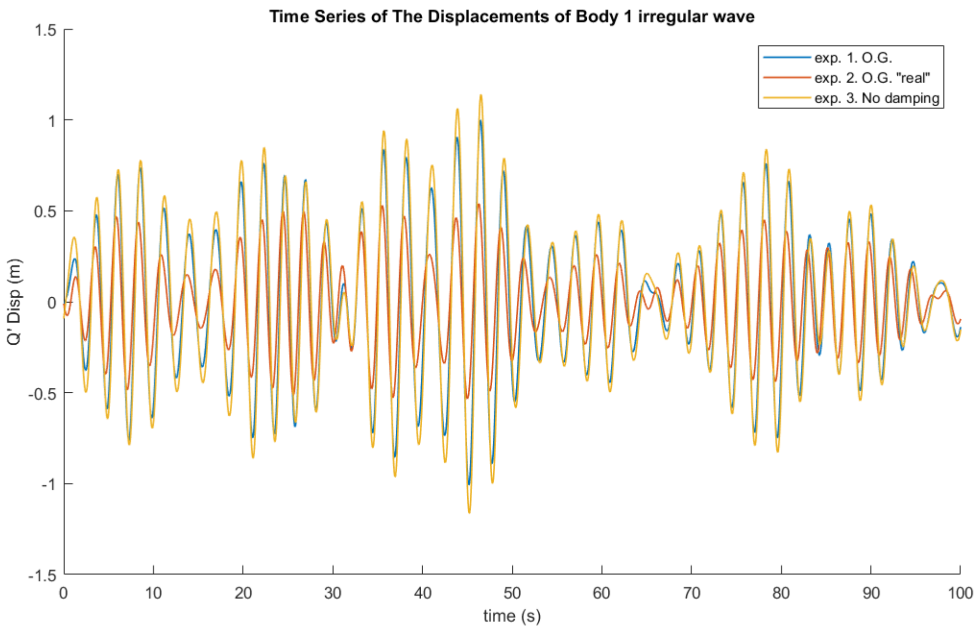

FIGURE 4.4: Ocean Grazer performance,irregular wave, displacement of body 1

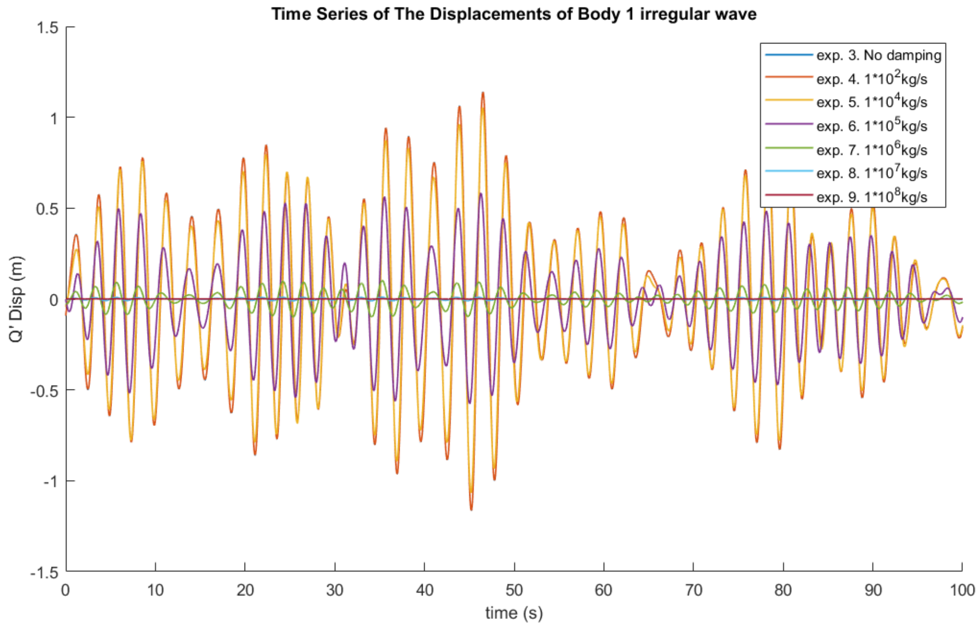

Figure 4.5: Sweep irregular wave, irregular wave, displacement of body 1

The results of floater bodies other than body 1 can be found in Appendix A.

The displacement behavior of the model to the sweeps, Figure 4.3 Figure 4.5, is as expected. The experiment without damping (experiment 3) follows the input wave in both regular and irregular waves. Since the damper is mechanically connected to the floater, it will directly influence the displacement of the floater. In Figure 4.2 and 4.3, at higher damping orders, decreased displacement follows. The model, at higher damping orders, cannot follow the irregular wave at $t = 30s$ and $t = 65s$, and the overshoot is higher as the damping increases.

4.2.2 Energy of the Radiation system

Stored energy

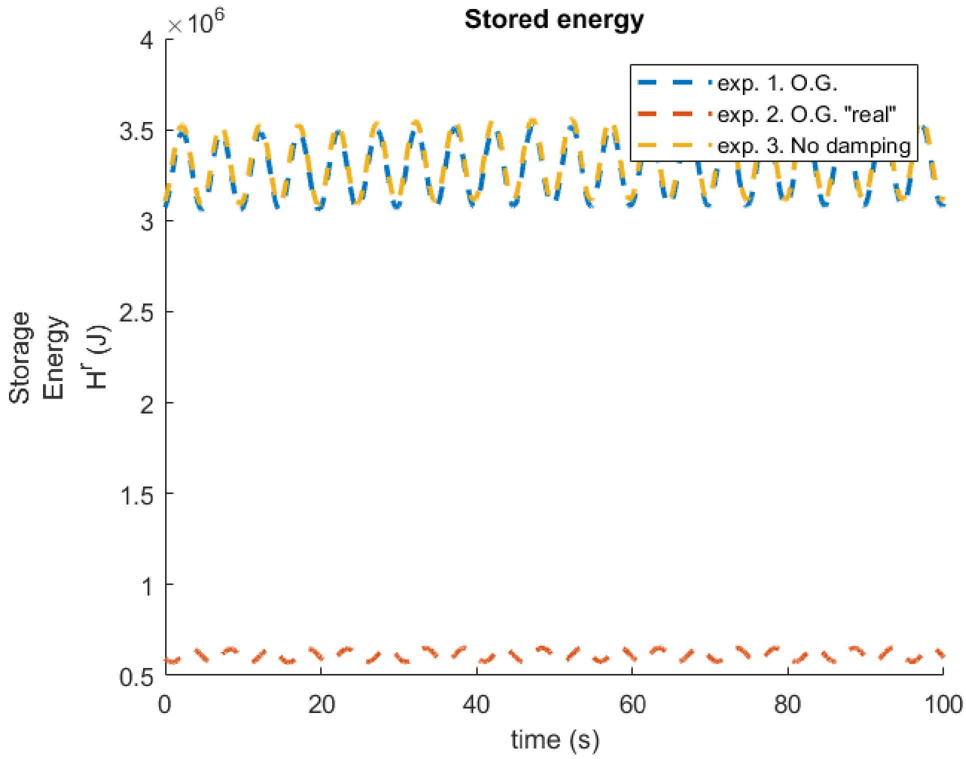

(A) Ocean Grazer, regular wave, stored energy

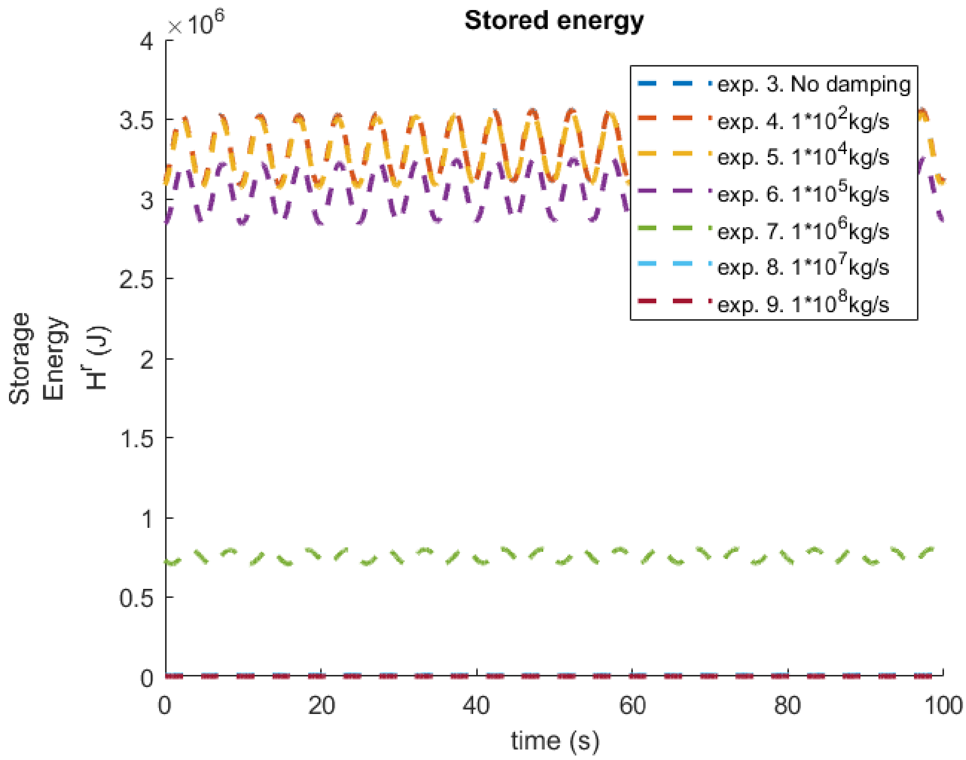

(B) sweep, regular wave, stored energy

Figure 4.6: Stored energy, regular wave

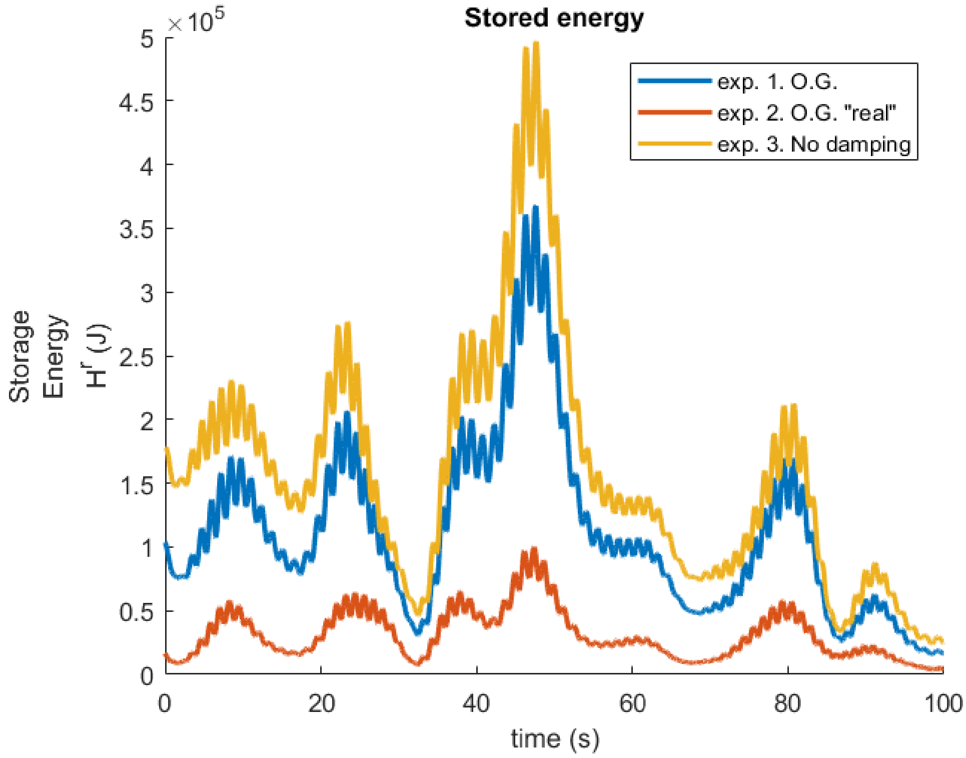

(A) Ocean Grazer, irregular wave, stored energy

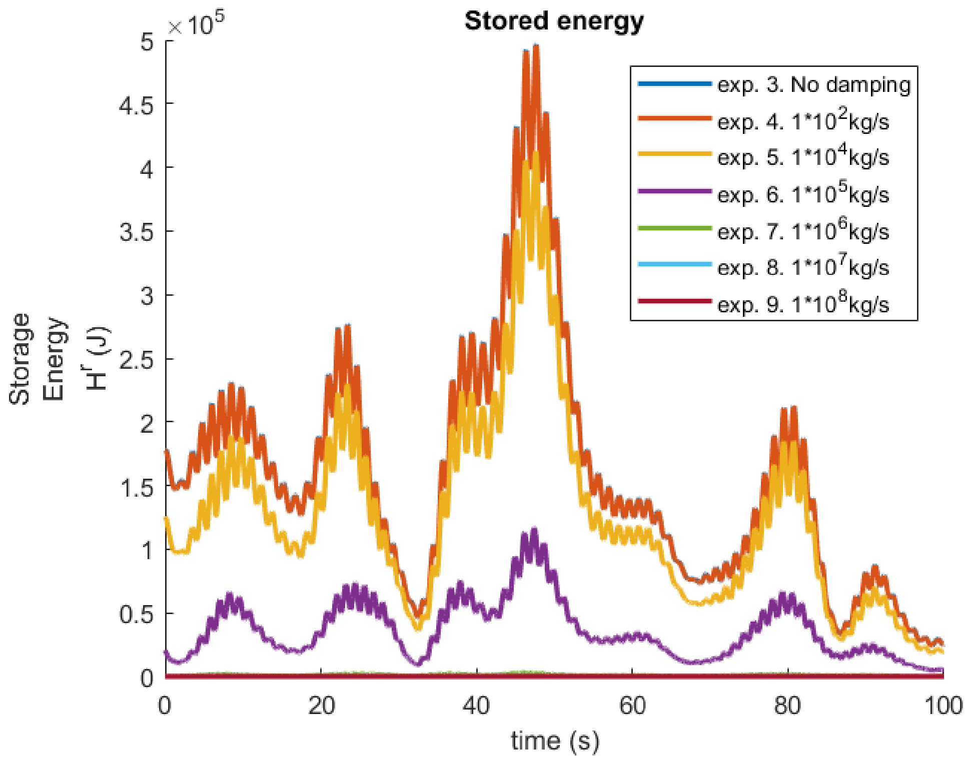

(B) sweep, irregular wave, stored energy

FIGURE 4.7: Stored energy, regular wave

Kinetic energy

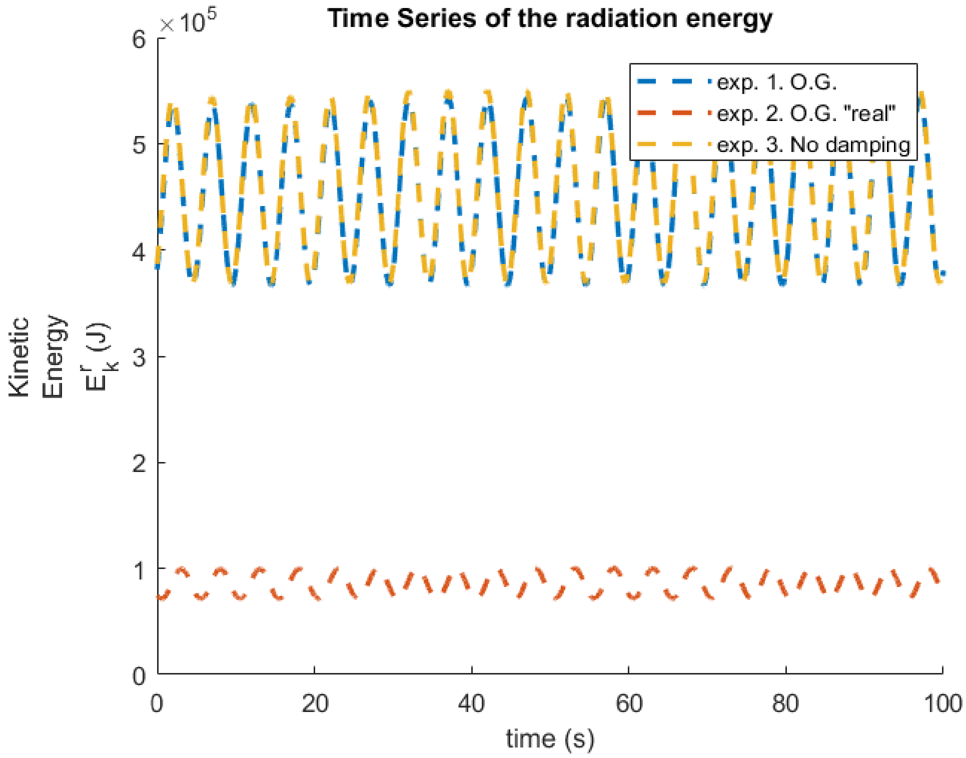

(A) Ocean Grazer, regular wave, kinetic energy

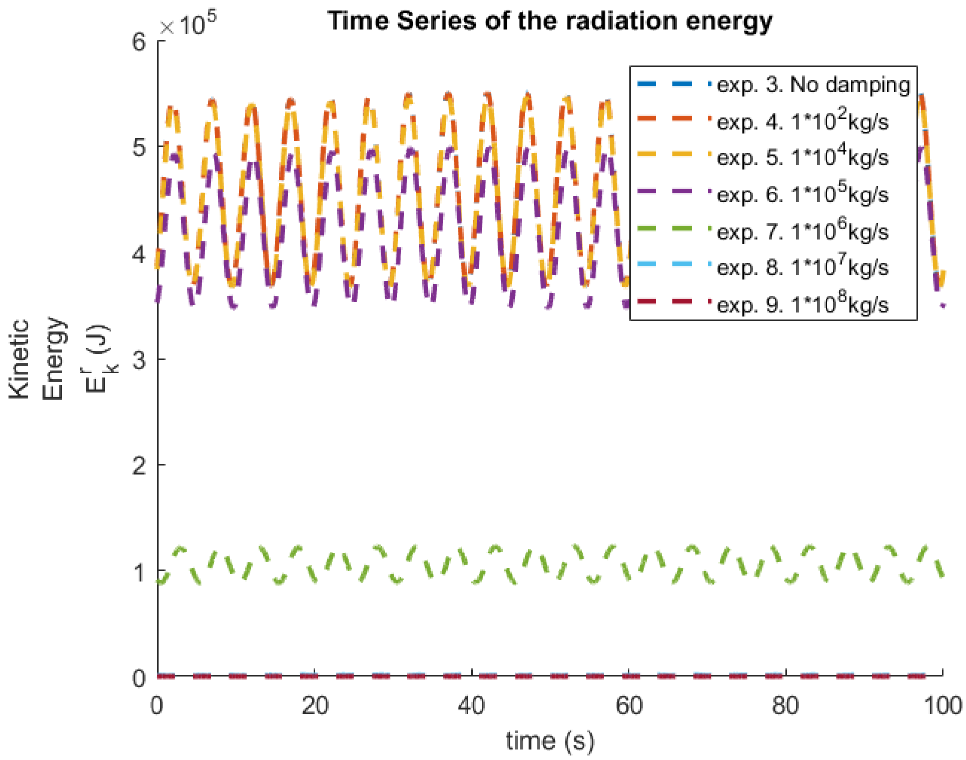

(B) sweep, regular wave, kinetic energy

FIGURE 4.8: Kinetic energy, regular wave

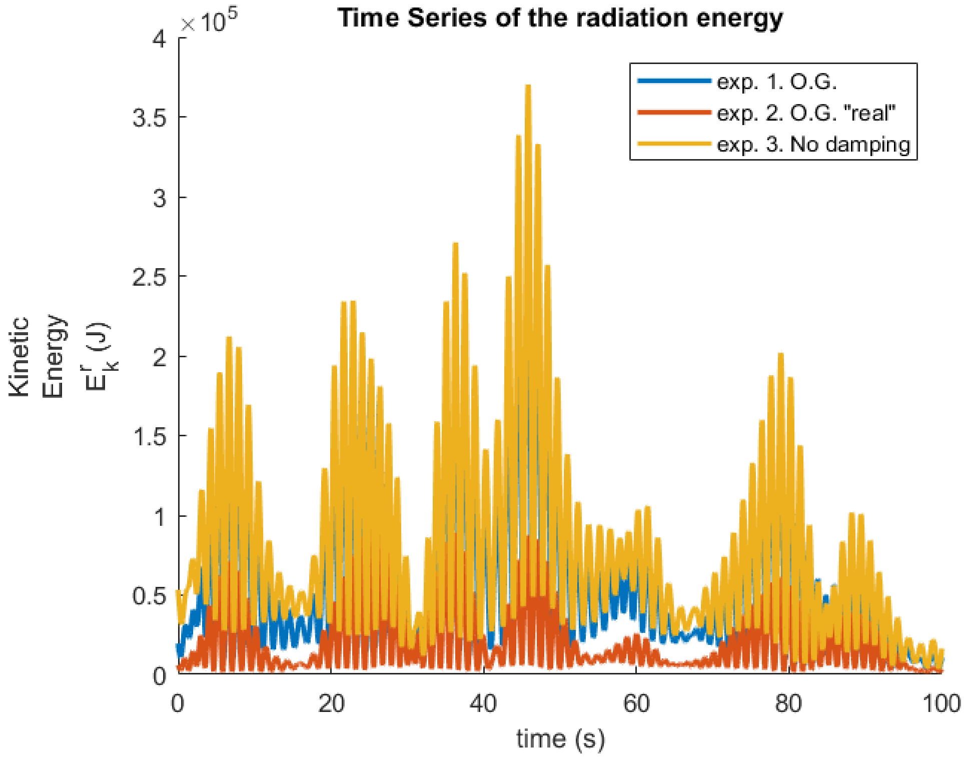

(A) Ocean Grazer, irregular wave, kinetic energy

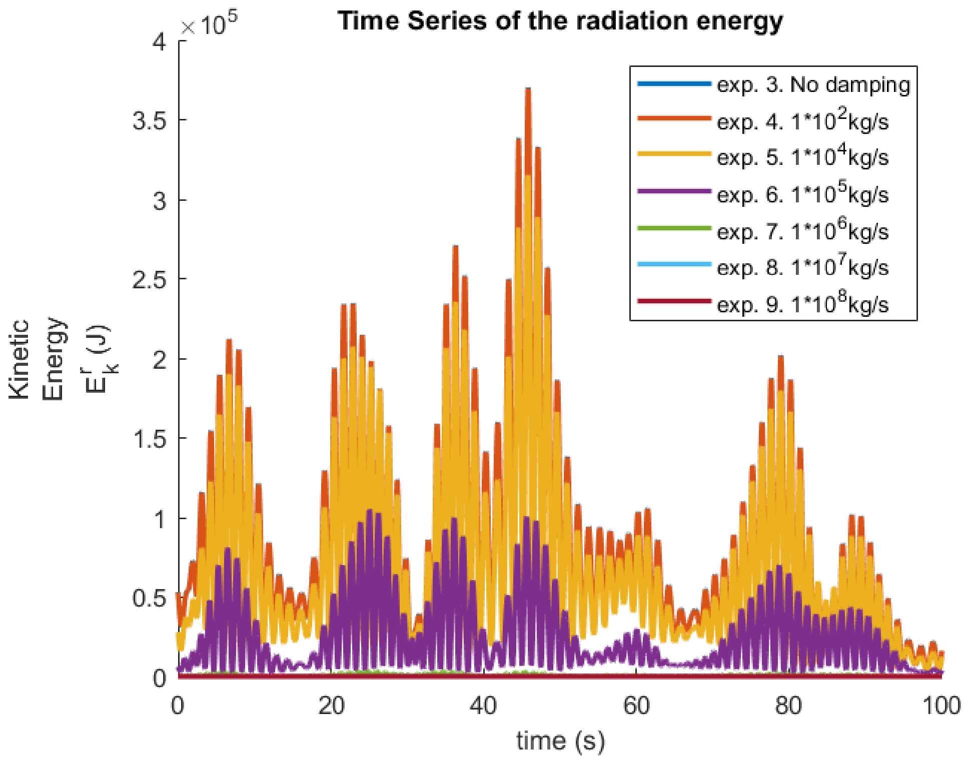

(B) sweep, irregular wave, kinetic energy

FIGURE 4.9: Sweep Kinetic energy, irregular wave

Sum of kinetic and stored energy of the radiation system

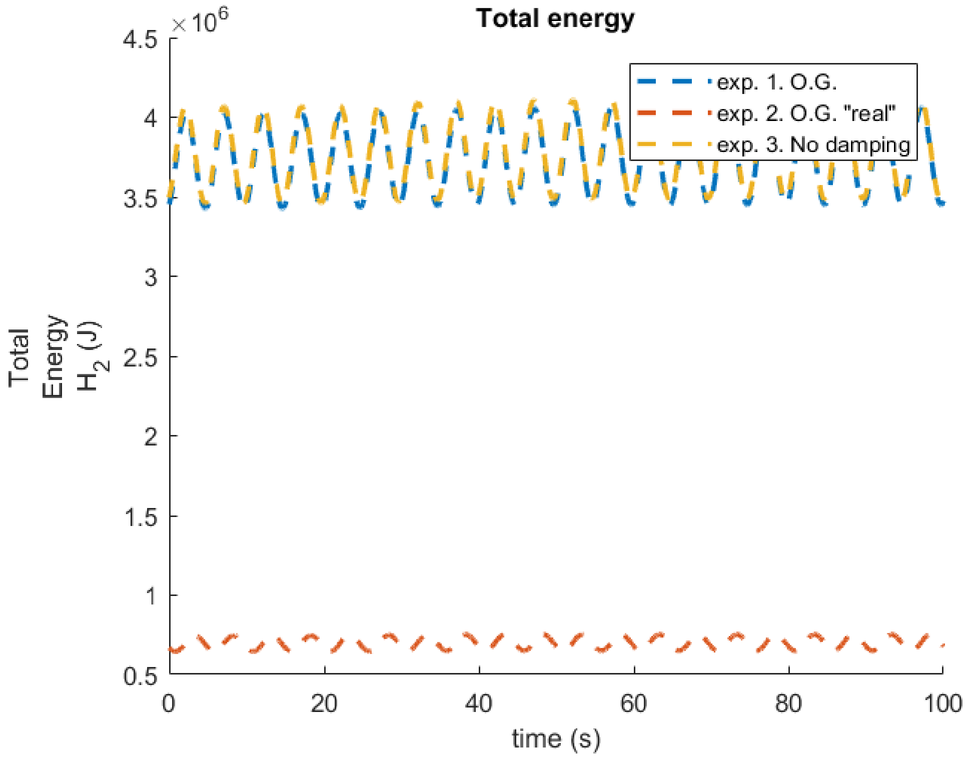

(A) sweep, regular wave

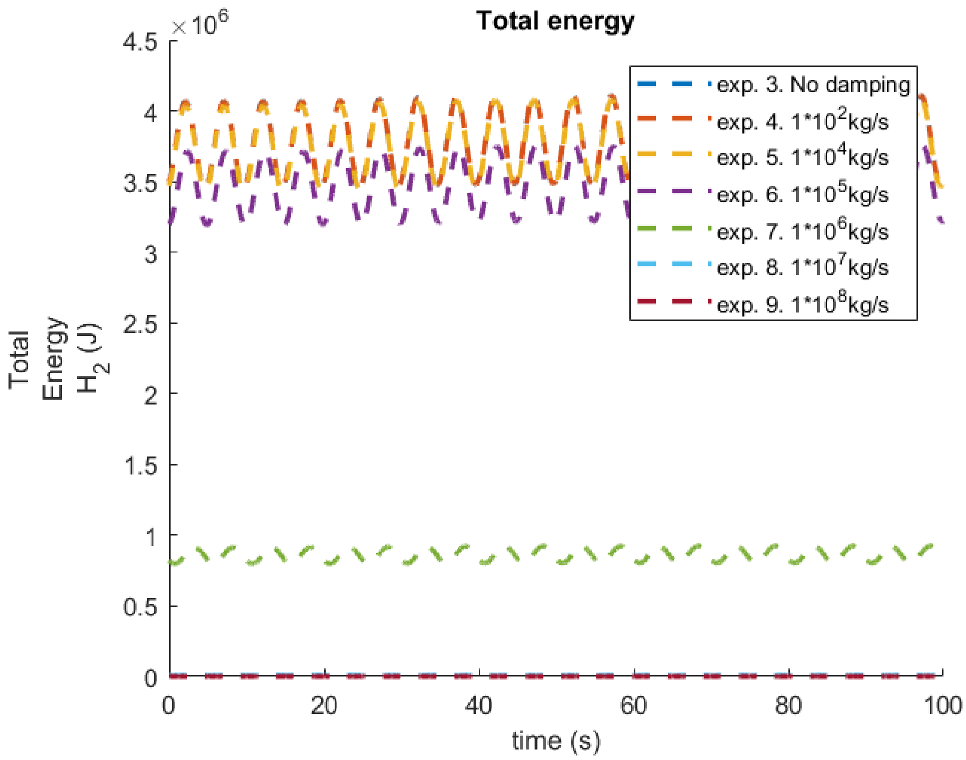

(B) sweep, regular wave

FIGURE 4.10: Sum of kinetic and storage energy of the radiation system, regular wave

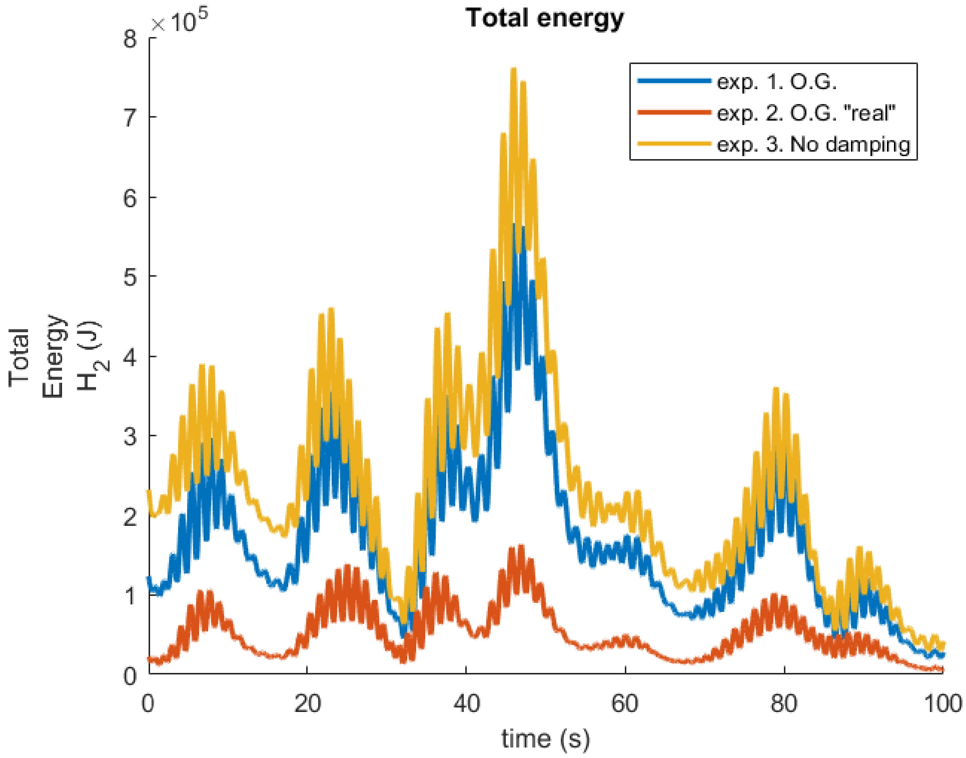

(A) Ocean Grazer, irregular wave

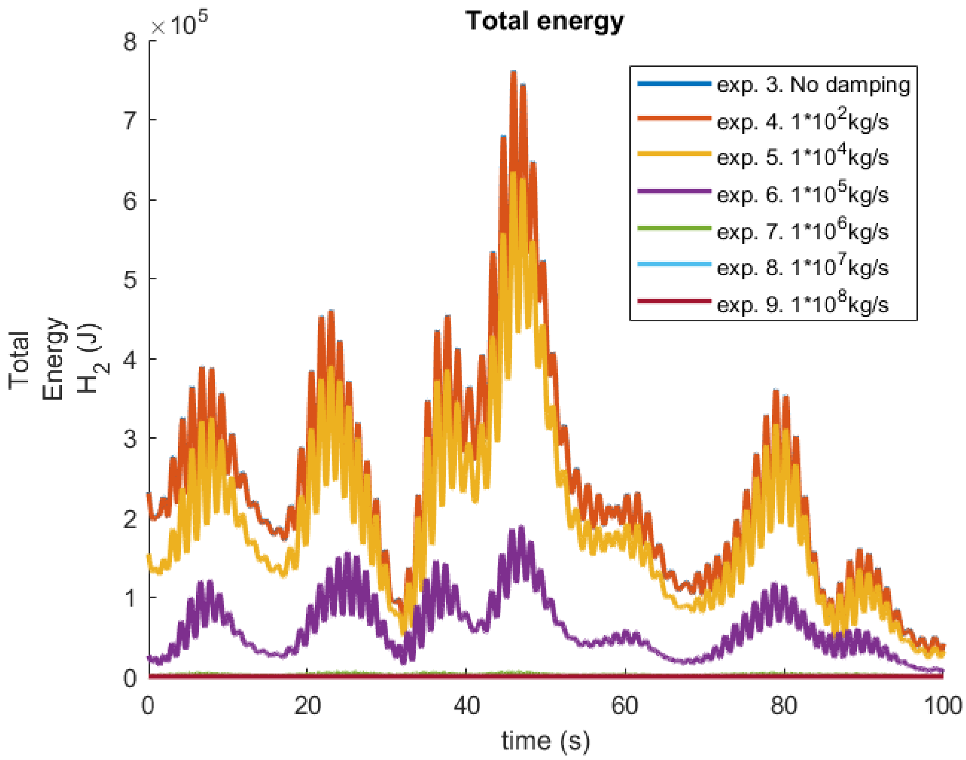

(B) sweep, irregular wave

FIGURE 4.11: Sum of kinetic and stored energy of the radiation system, irregular wave

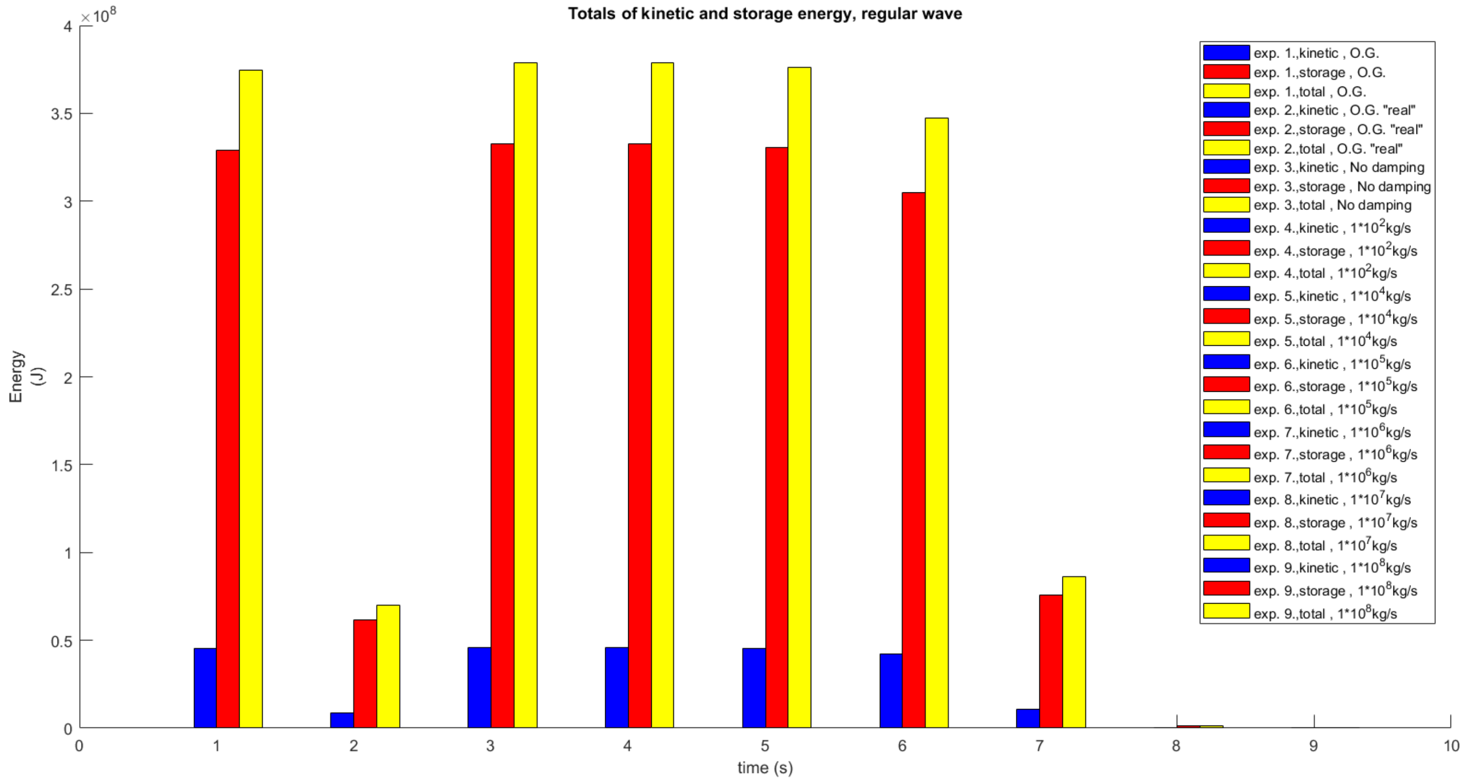

FIGURE 4.12: Total energy of the radiation system over the observed timeframe of 100 seconds, regular wave. In this bar-graph the blue bars illustrate the energy of the kinetic part of the radiation system, the red bars illustrate the energy storage part of the radiation system and the yellow bars illustrate the total energy of the radiation system

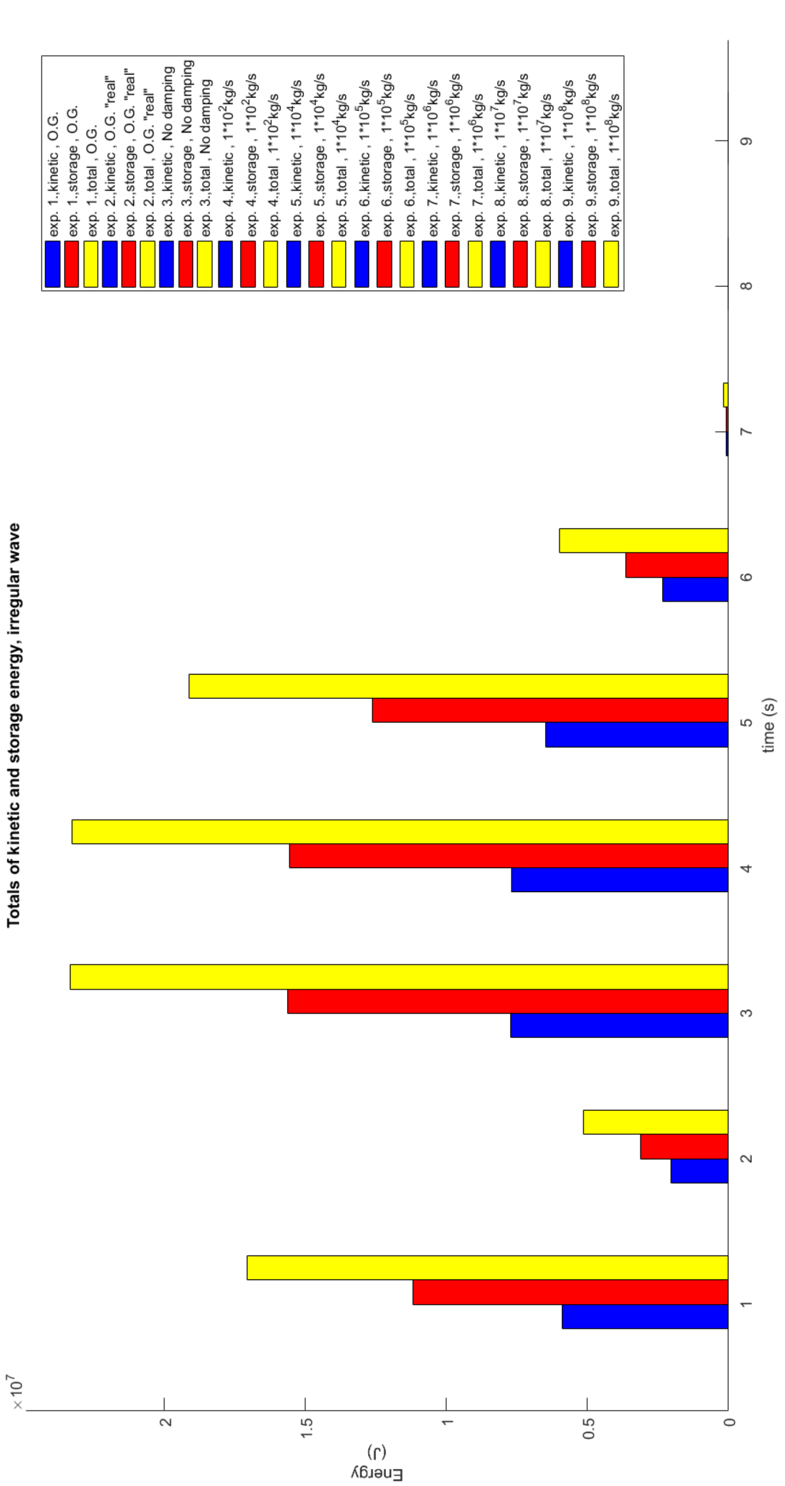

FIGURE 4.13: Total energy of the radiation system over the observed timeframe of 100 seconds, irregular wave. In this bar-graph the blue bars illustrate the energy of the kinetic part of the radiation system, the red bars illustrate the energy storage part of the radiation system and the yellow bars illustrate the total energy of the radiation system

The results of the radiation energy of the Ocean Grazer under regular and irregular waves show that the energy of the kinetic subsystem is less than the energy of the storage subsystem. When the model uses the regular wave as input the difference in energy between the storage and kinetic subsystem is about factor 8.75, for the irregular wave this difference is, with factor 2, lower. The parameter sweeps show that at higher frequencies and fluctuating waves heights the experiments with higher damping orders capture less energy, as can be seen in Figure 4.6 and 4.13.

4.2.3 Energy of the mechanical system

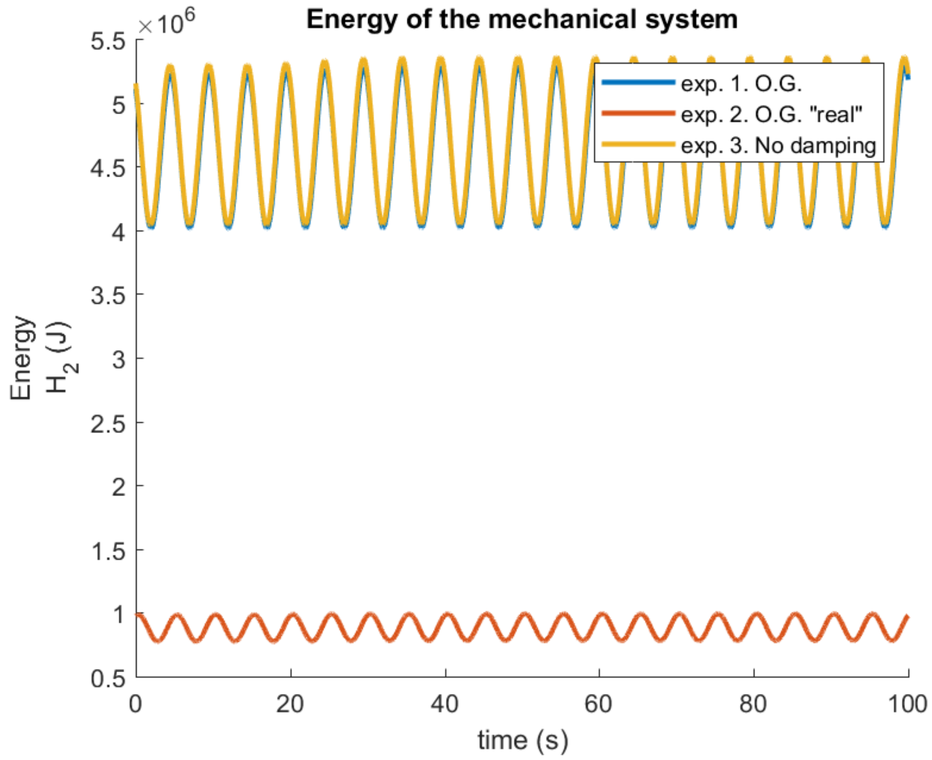

(A) Energy of the mechanical system, regular wave

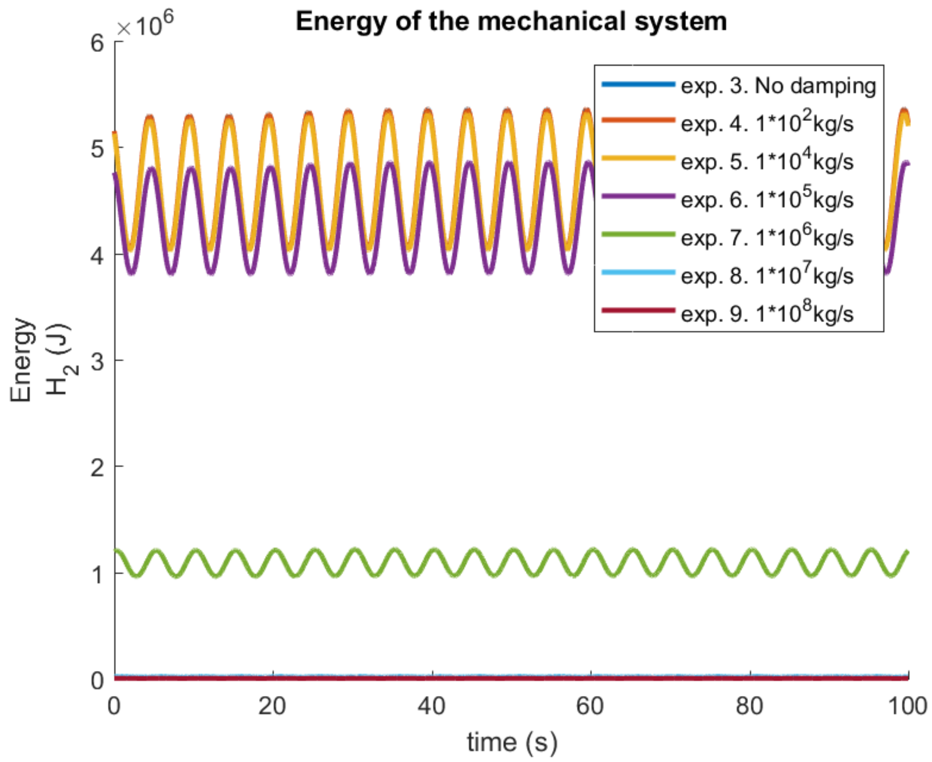

(B) Energy of the mechanical system, regular wave

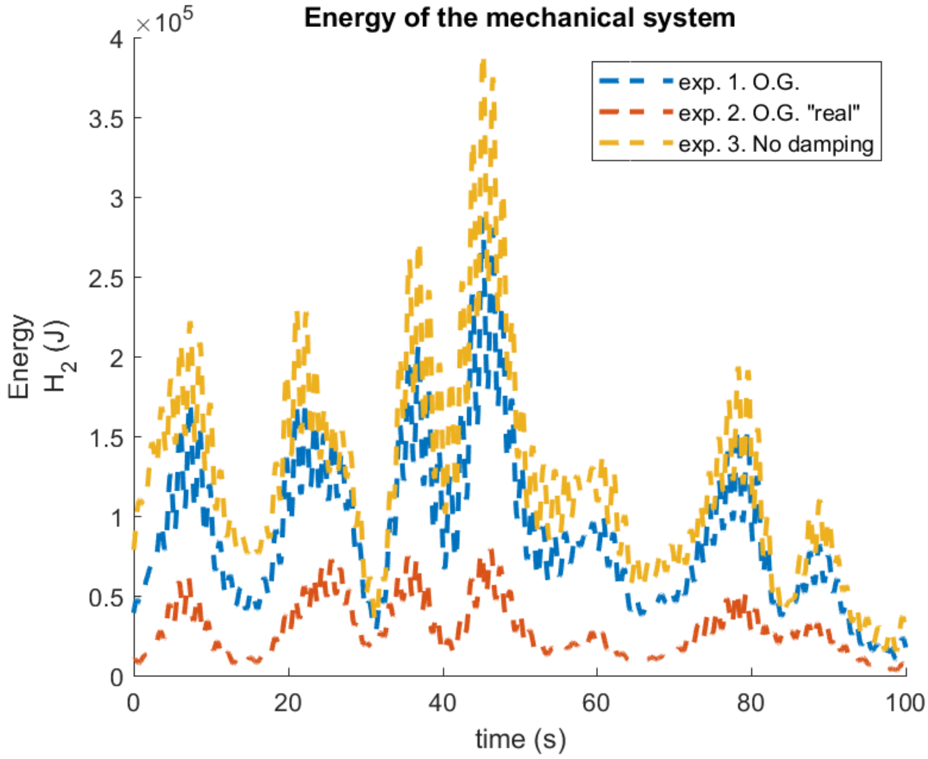

(A) Energy of the mechanical system, irregular wave

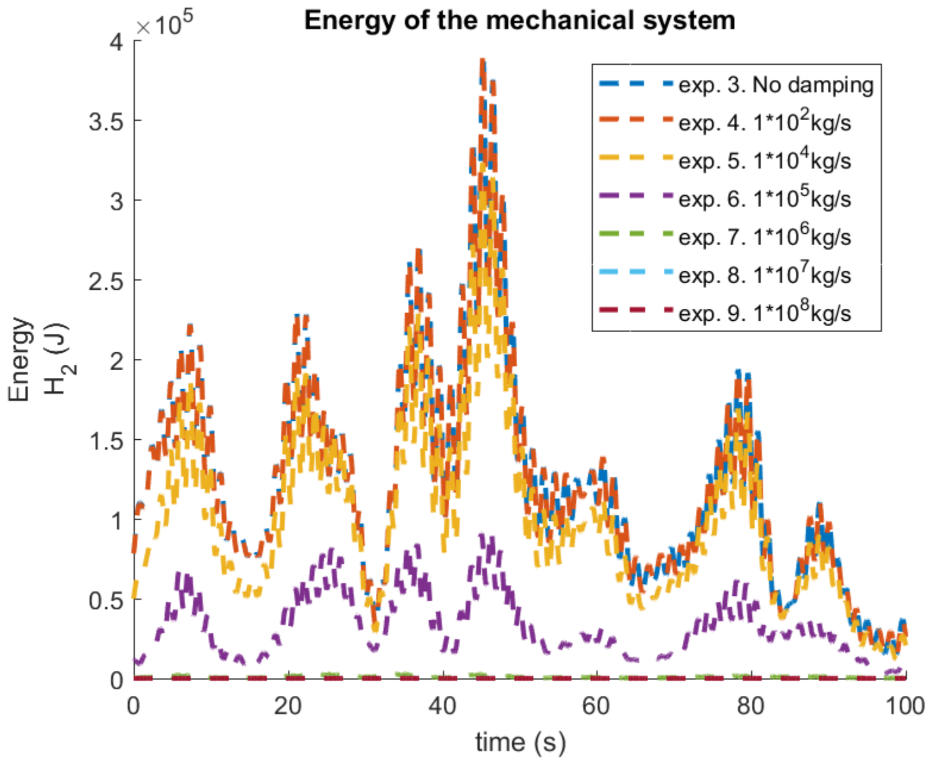

(B) Energy of the mechanical system, irregular wave

The model's behavior of the mechanical system under the regular and irregular wave is comparable to that of the radiation system; as expected the experiment without damping (experiment 3), receives most energy. The scaled lab test (experiment 2) performs less than the damping coefficient of earlier research (experiment 1). The experiments with regular and irregular waves show that experiment 3,4,5 have similar energy capture characteristics. What is different is that the captured energy of the mechanical system is less than the captured energy of radiation system for the irregular wave, while under the regular wave, the energy of the mechanical system exceeds the energy of the radiation system.

4.2.4 Energy of the total port-Hamiltonian system

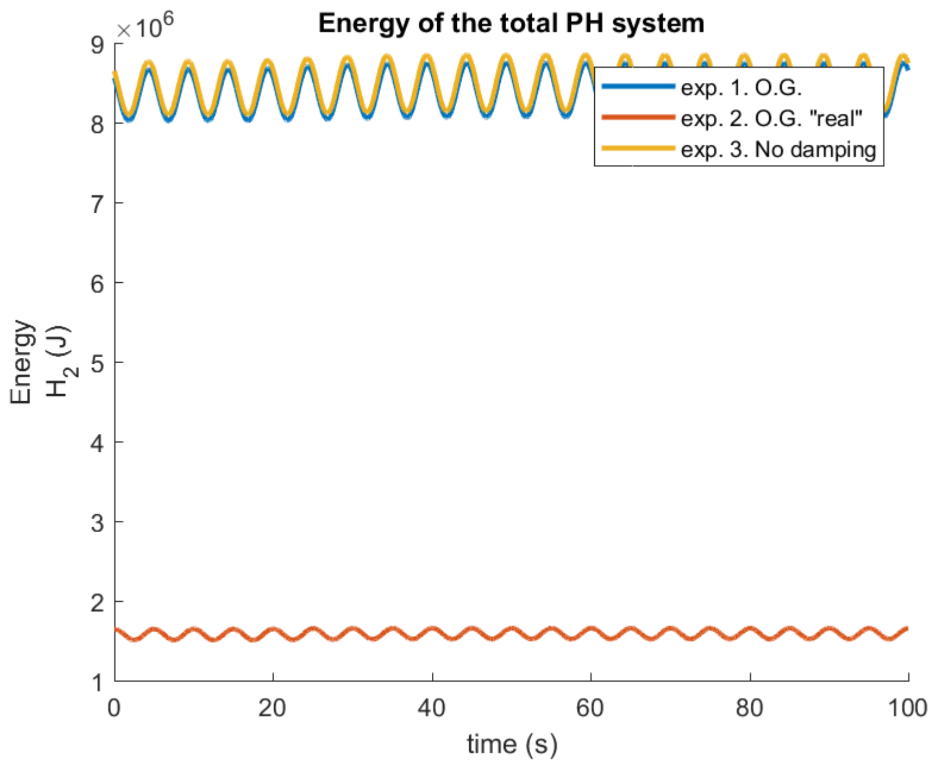

(A) Total energy of the port-Hamiltonian model, regular wave

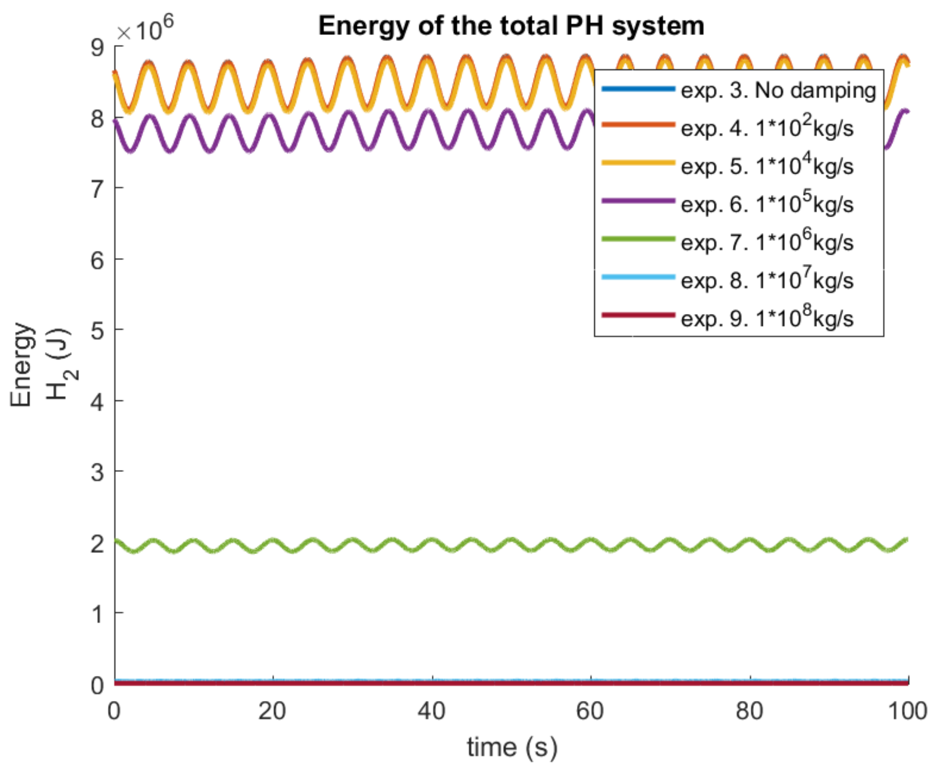

(B) Total energy of the port-Hamiltonian model, regular wave

FIGURE 4.16: The total energy of the port hamiltonian simulation, the total energy is defined as the sum of the energy of the radiation and mechanical systems, in this case under the regular wave.

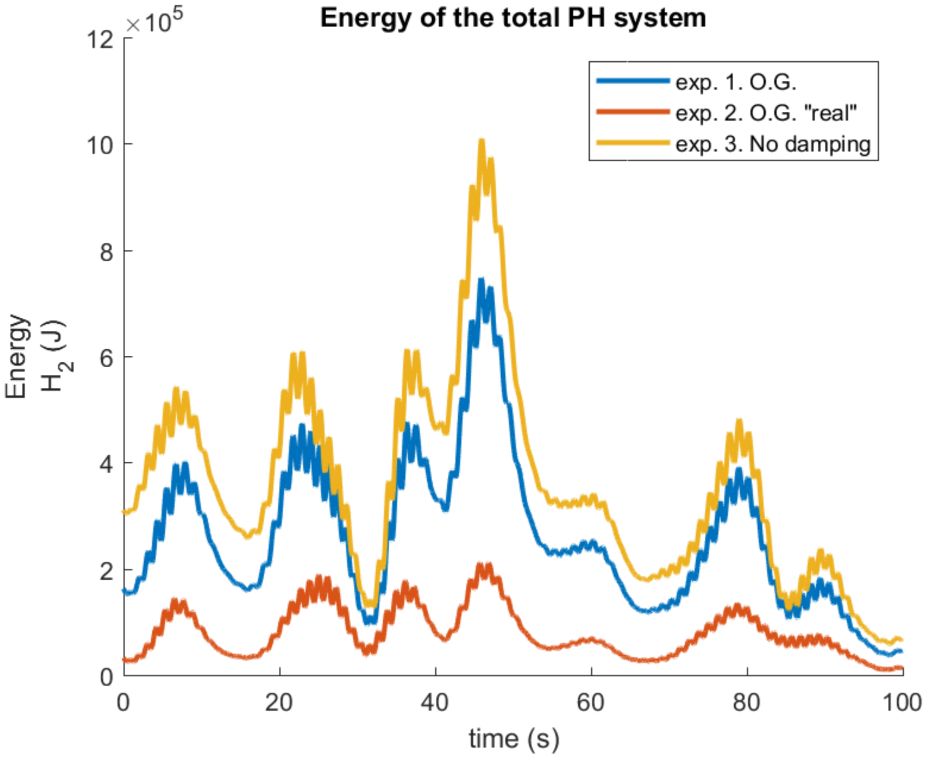

(A) Total energy of the port-Hamiltonian model, irregular wave

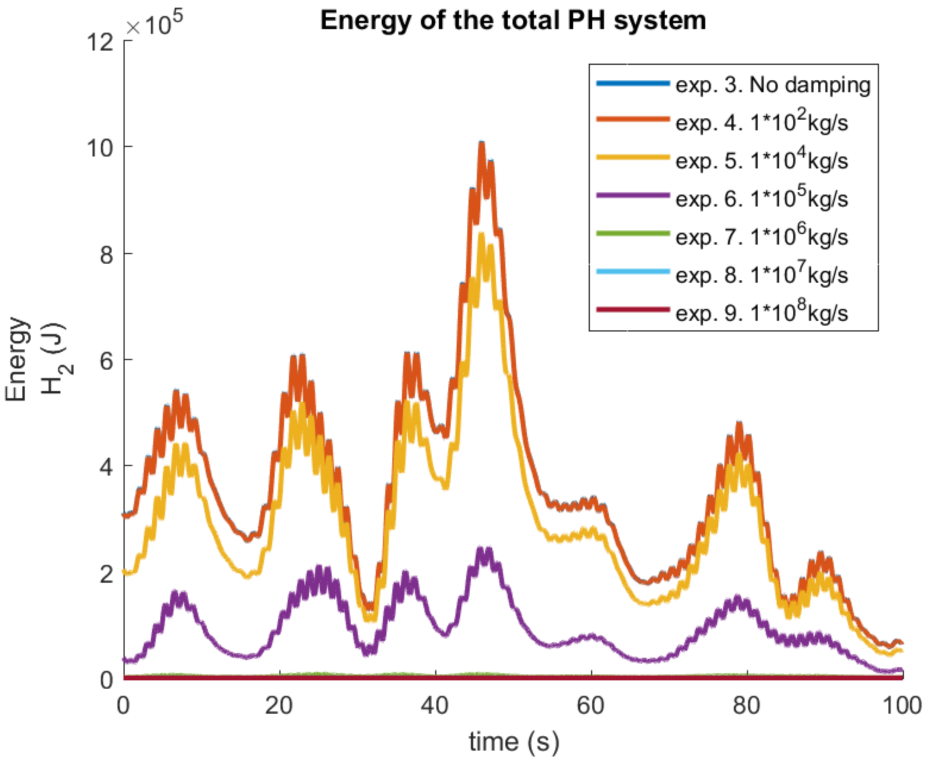

(B) Total energy of the port-Hamiltonian model, irregular wave

FIGURE 4.17: The total energy of the port-Hamiltonian simulation, the total energy is defined as the sum of the energy of the radiation and mechanical systems, in this case under the irregular wave.

Based on the earlier results and the total energy of the port-Hamiltonian system the following conclusions can be drawn. Damping coefficients larger than $1 \times 10^7 kg/s$ (experiment 8 and 9) are inefficient at capturing energy under the wave conditions specified in this test. Using a lower damping coefficient is beneficial for the amount of energy captured, a damping coefficient of $0kg/s$ is most beneficial. The results of the experiments show a sharp decline in captured energy around experiment five/six in the mechanical and radiation system under regular and irregular waves. When the model is subject to a situation with regular waves[2] the mechanical system is dominant while using the irregular wave as input, radiation system contributes more energy to the total. Considering the Ocean Grazer, the scaled lab version shows less energy captured, then was used in earlier research. However, as this experiment uses a linearly scaled dampening coefficient based on pipe length, the exact results cannot be regarded as sufficiently trustworthy due to the assumptions. Since this lab setup is used for the design and testing of Ocean Grazer components, it may be recommended to research the validity of the lab setup's parameters.

4.3 Validation

Validation of the results is in this research done using the popular model "Wave-Energy-Converter Simulator". This so-called 'WEC-Sim' has been developed by the U.S. National Renewable Energy Laboratory (NREL) and Sandia National Laboratories (SNL) as a publicly available, low cost, open-source wave energy converter modeling tool. This simulator was developed to reduce the dependency of wave energy developers on commercially available codes. The code of this project is open-source and can be acquired from Github[3]. The WEC-Sim has itself been validated against several commercial models; WaveDyn, AQWA, and OrcaFlex. The validation of WEC-Sim was done by modeling a one degree of freedom point absorber, where simulations were run with and without PTO damping. A minimal difference of approximately 0.02m between the WEC-Sim results and those of WaveDyn and AQWA. Simulations using three degrees of freedom see a maximum difference of 0.01 m and 0.03 deg with OrcaFlex[58].

Physical model validation of the WEC-Sim has been done using a FOSWEC experimental setup[59][60]. This consisted of a floating platform with two hinged flaps that rotate in pitch. The platform is free to move in heave, pitch, and surge and can be configured to lock DOFs. A wave is simulated in a wave tank, and with the same characteristics modeled in WEC-Sim. The WEC-Sim has shown good agreement with the physical experiment on heave decay, pitch decay and surge decay (wave dampening)[61].

The port-Hamiltonian model is validated by comparing the position output of the floater bodies under a regular and irregular wave with WEC-Sim. Both models used the parameters specified in Table 4.2.

[2]of the specified wave height and wave period
[3]https://github.com/WEC-Sim/WEC-Sim

4.3.1 Validation results

Both models, under the regular wave, appear to be stable, the displacement does not increase or decrease over time. This is an indication of model passivity.

To increase readability, only body 1,3,5,9 are shown to show the trend, body ten because it behaves differently than the rest.

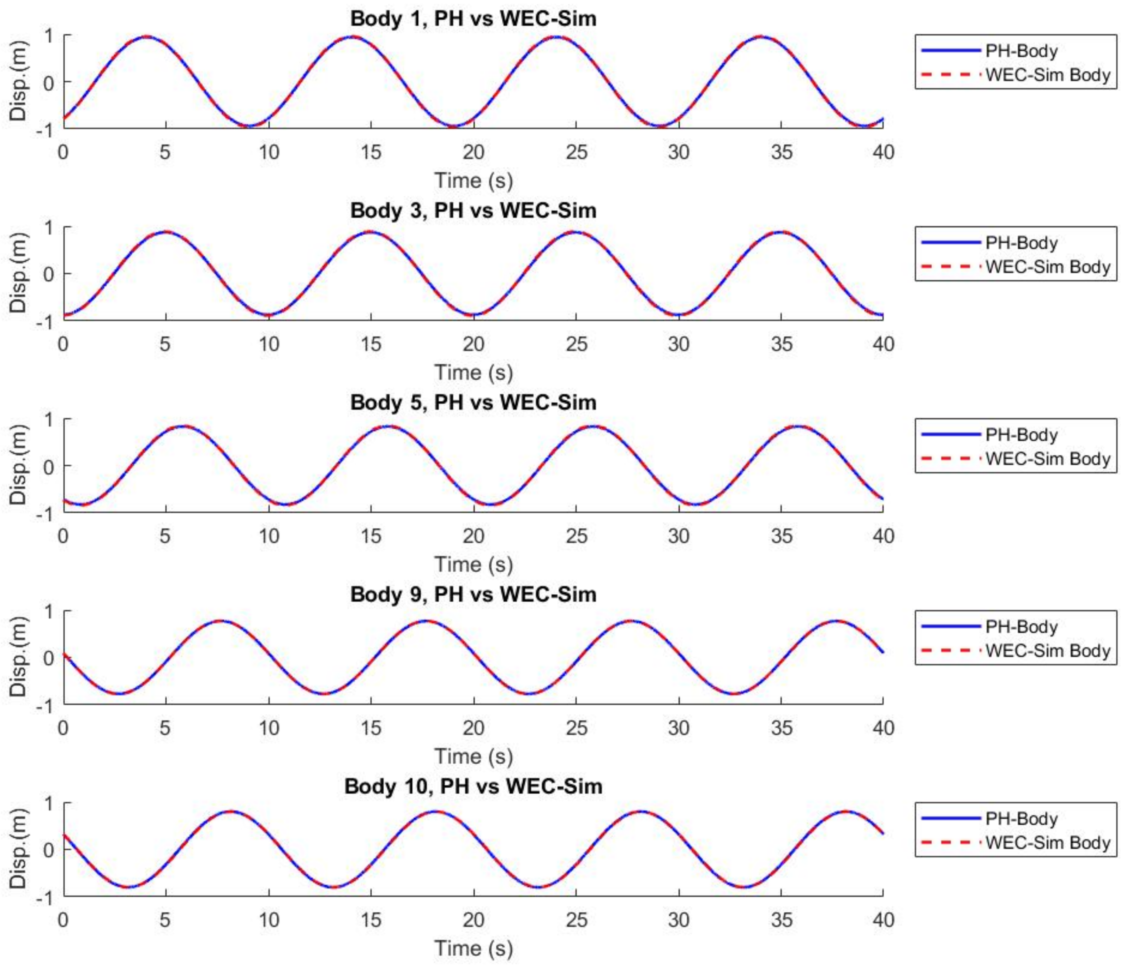

FIGURE 4.18: The relative position of floaters, using the WEC-Sim with the parameters for the regular wave as indicated before.

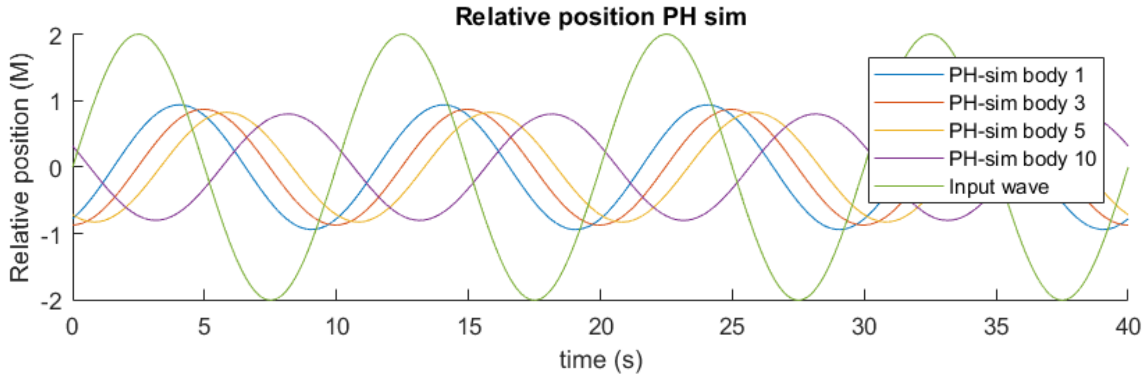

FIGURE 4.19: The relative position of floaters, using the port-Hamiltonian simulation with the parameters as indicated before.

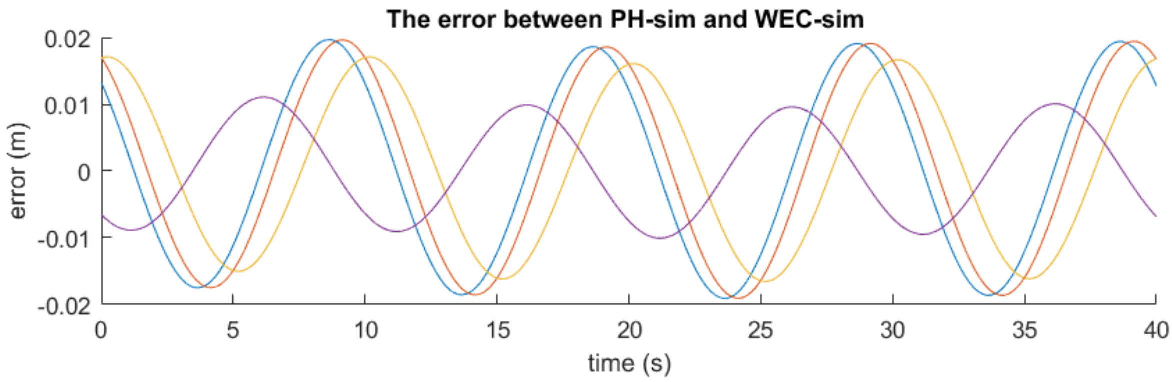

FIGURE 4.20: The error between the WEC-Sim and the port-Hamiltonian simulation, showing both model passivity, Body1 shown as the solid blue line, body 3 two shown as the solid orange line, body five shown as a yellow line, body ten is indicated by the purple line

The output of the models is comparable, the error in relative position is shown in Figure 4.20. The difference between the position of the floater bodies reported by both models is at its maximum 1.25%, or 0.0125m on a relative body displacement of 1 meters. This means that the port-Hamiltonian model under a regular wave can be considered validated with good agreement to the WEC-Sim. The size of the radiation matrix is a factor that influences both computing speed and accuracy the of the calculation; the difference between both models can be reduced at the cost of computation speed.

Validation of the irregular wave is done using the parameters of Table 4.2, except for the significant wave height. The significant wave height of the irregular wave used in the validation is $1.4m$.

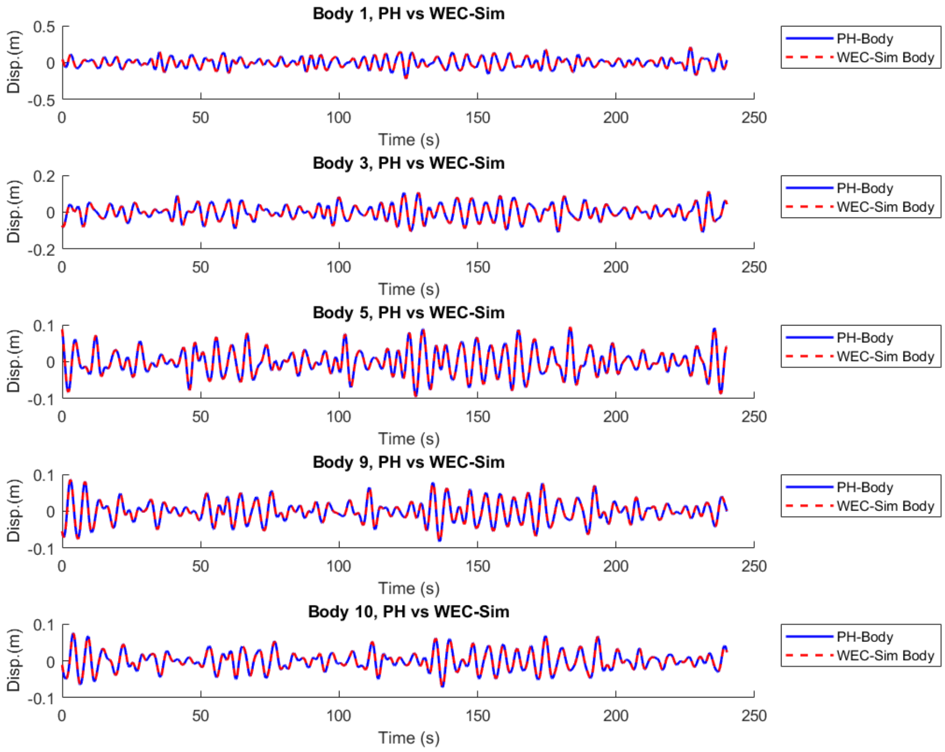

FIGURE 4.21: In this figure a comparison of several floater bodies, WEC-SIM vs PH-Sim can be seen. In the first two graphs the y-axis is of a different scale.

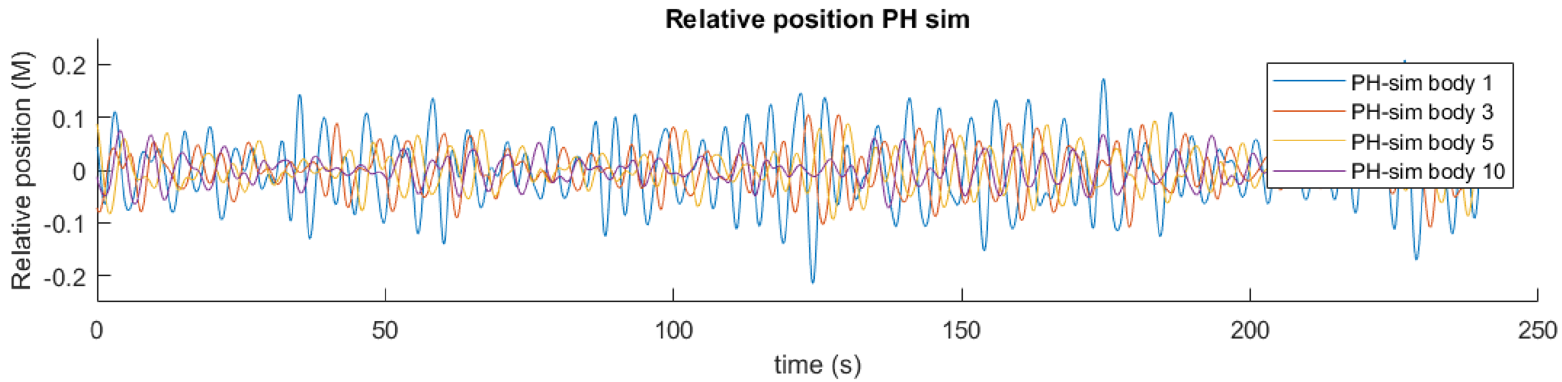

FIGURE 4.22: The Relative position of several of the port-Hamiltonian floater-bodies

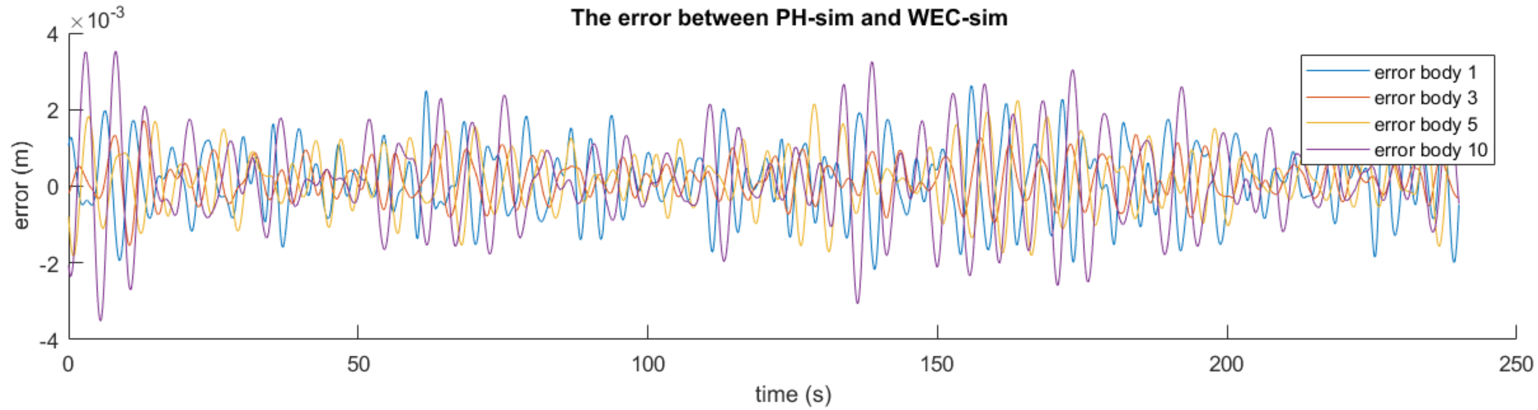

FIGURE 4.23: In this illustration, the difference between the WECSim and the port-Hamiltonian simulation kan be observed. The error is within 4 mm.

The models give for multiple floaters a comparable result. The difference in displacement of the floater bodies between both models stays within $4mm$. The difference between floater displacement is highest between 125 and 150 seconds;

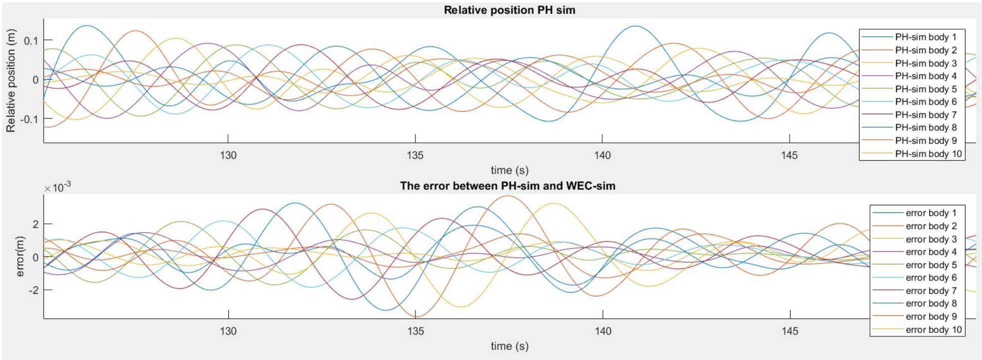

FIGURE 4.24: The error between the WECSim and the port-Hamiltonian simulation at $150 > t > 125$

Overall, the error is less than $4mm$ on a displacement of $0.2127m$ this gives an error rate of 1.88%. The experienced error rate is higher than the 1.25% of the initial regular wave; the difference is 0.53%. Since the error rates and the difference in error rate are sufficiently low, the conclusion can be drawn that both models are in good agreement with each other.

Chapter 5

Conclusions and recomendations

5.1 Conclusions

In this research thesis, we extend the previous work on the modeling of the wave-floater blanket interaction. The first contribution of the thesis is the development of a generalized port-Hamiltonian model that describes the wave-floater blanket simulation. The generic dynamical model is applied to the case of a floater blanket with ten floaters, under irregular waves, and is validated with the existing computer model using WEC-sim. The second contribution of the thesis is the performance analysis of the Ocean Grazer's floater blanket (with ten-floaters) connected to linear PTO systems. As part of our first contribution, we investigate the modeling of a realistic irregular wave based on the well-studied Bretschneider wave spectrum. In particular, we present the design of such an irregular wave generator by employing a white-noise generator coupled with a specially designed band-pass filter. These filters where constructed using three different methods, FIR, IIR and a FIR/IIR combination. FIR filters seem to have the best fitt and execution time, IIR filters have been found to show a lower setuptime. The synthesized wave has been used as input for the tests conducted in chapter 5.

Using this realistic irregular wave time series, we validated the dynamic behaviour of the ten-floater case that is modeled using our port-Hamiltonian model. The simulation is compared with the simulation results of the popular WEC-sim computer model that is widely used for simulating various wave energy converters. For the regular wave, a maximum error of 0.0125 meters on a relative body displacement of 1 meter, which corresponds to an error percentage of 1.25% For the irregular wave, the error percentage is about 1.88%

During the investigation of the performance of the floater-blanket, several experiments where conducted. Analysis learns that under irregular waveinput, concerning the the contribution of energy, the radiation system is dominant over the mechanical system. The model behaves opposite under regular wave input, where the mechanical system is dominant. During the experiments the captured energy shows a sharp decline at higher order dampening coefficients and is different under regular and irregular wave inputs. The results of experiments using Ocean Grazer's scaled lab setup, due to the assumptions, aren't regarded as suffiently accurate, but suggest a lower powercapture than assumed in previous work.

5.2 Recommendations

Several recommendations that can be made based on the research;

1. The results of experiments using Ocean Grazer's scaled lab setup, due to the assumptions, cannot be regarded as suffiently accurate. The research performed on the lab setup is used to develop parts and components of the full size Ocean Grazer. It is advisable to research the parameters of the lab setup, and look at the scalability.

2. The port-Hamiltonian model behind this research can be quite easily expanded to accomodate multiple wave spectra, a non-linear PTO, take into account rising and falling water levels, a turbine and some flow dependent resistance. It is advisable to expand the model.

3. Regarding the computational speed, if this is beneficial for the project it might be beneficial to reduce steps not exactly necessary for the simulation of the system. Matrix size reductions have a really large impact on calculation time (as in 4 hrs vs 30 min) as we have shown in chapter 4. One could try and programm the model more neatly and open for reductions.

Acknowledgements

I would first like to thank Prof. dr. B. Jayawardhana, M.Z. Almuzakki, MSc. and dr. J.D.J. Barradas-Berglind who have been closest involved in my research. The door to their office was always open when I ran into problems or got stuck. Interesting and helpful discussions helped me to get it on the right track. I would like to thank M. van Rooij MSc. for his models which I in turn was able to visualize in Zspace/Unity. I would like to acknowledge dr. A.I. Vakis as the second reader of this thesis.

I experienced a lot of great activities together with the Ocean Grazer team; Part of my research included a 3D vizualization, on a 3D viewer, that was made in less then 5 evenings to meet a presentation deadline. During this presentation we presented this work to several researchers, CEO's and the rector magnificus of the University.

FIGURE 5.1: The photo that is taken on the booth of Ocean Grazer during the day of the engineer 2018. In the picture, I (on the left) explained the Ocean Grazer concept to Elmer Sterken, Rector Magnificus of the University of Groningen

This helped me to really feel part of the team. I would therfore like to thank all other members of the Ocean Grazer group who helped and supported me towards the goal of my research project.

"The more I learn, the more I realize that I know so little.. " - Unknown

Appendix A

Body displacement

A.1 regular wave

The phase shift of the input wave and floater position, that can be seen in the graphs of Appendix A, is due to the horizontal distance of the floater to the point at which the wave is generated.

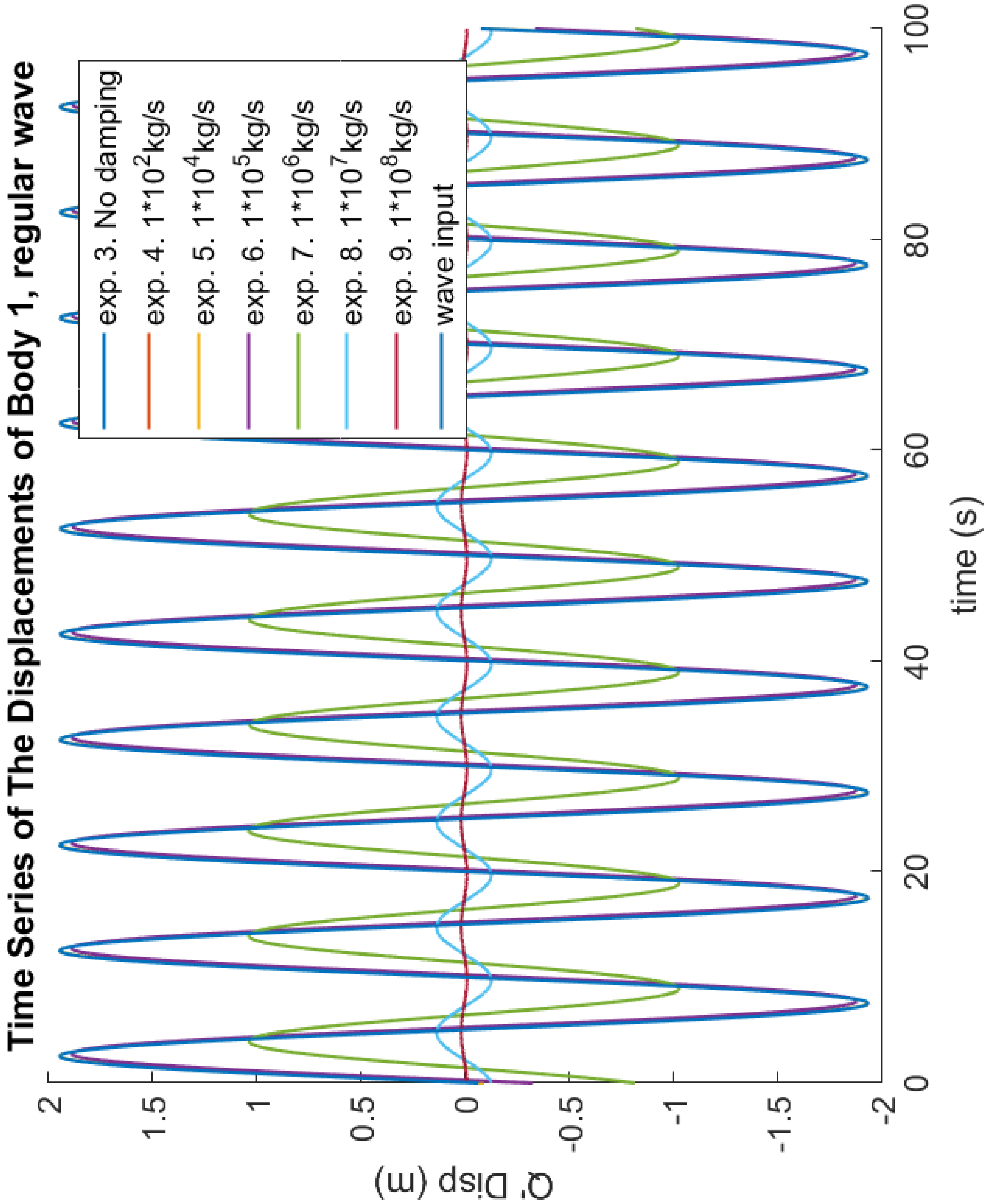

FIGURE A.1: Sweep, irregular wave, displacement of body 1

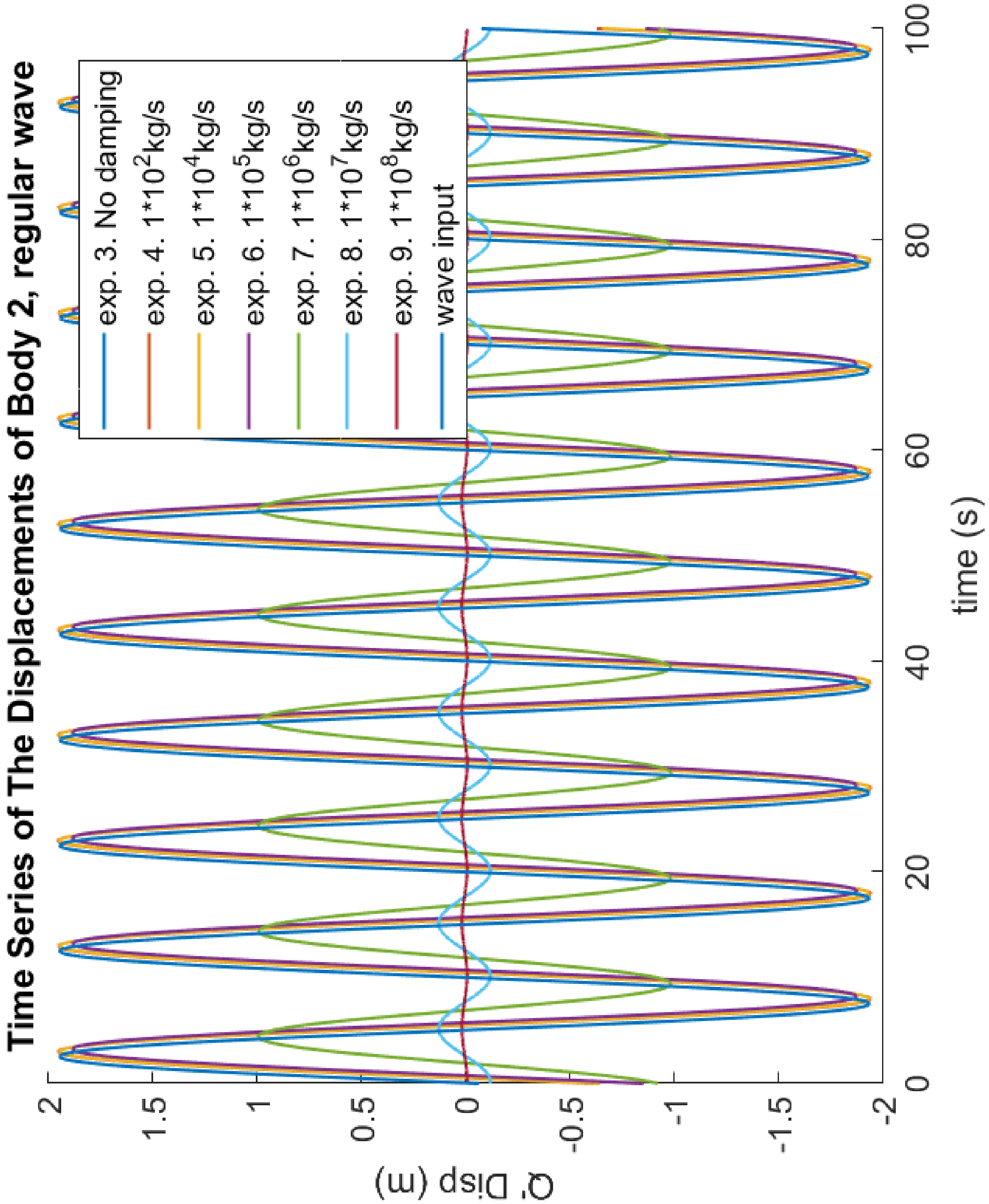

FIGURE A.2: Sweep, irregular wave, displacement of body 2

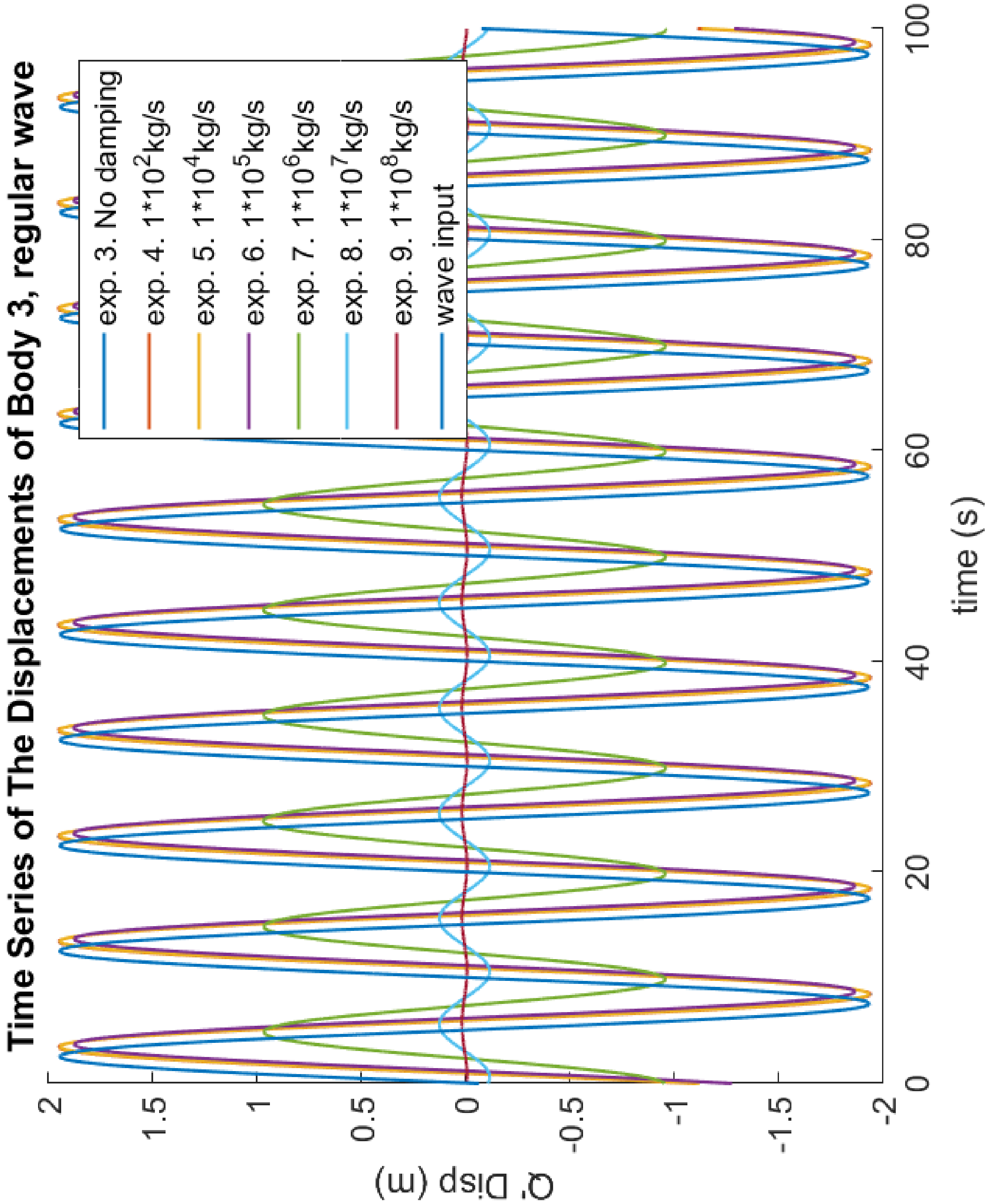

Figure A.3: Sweep, irregular wave, displacement of body 3

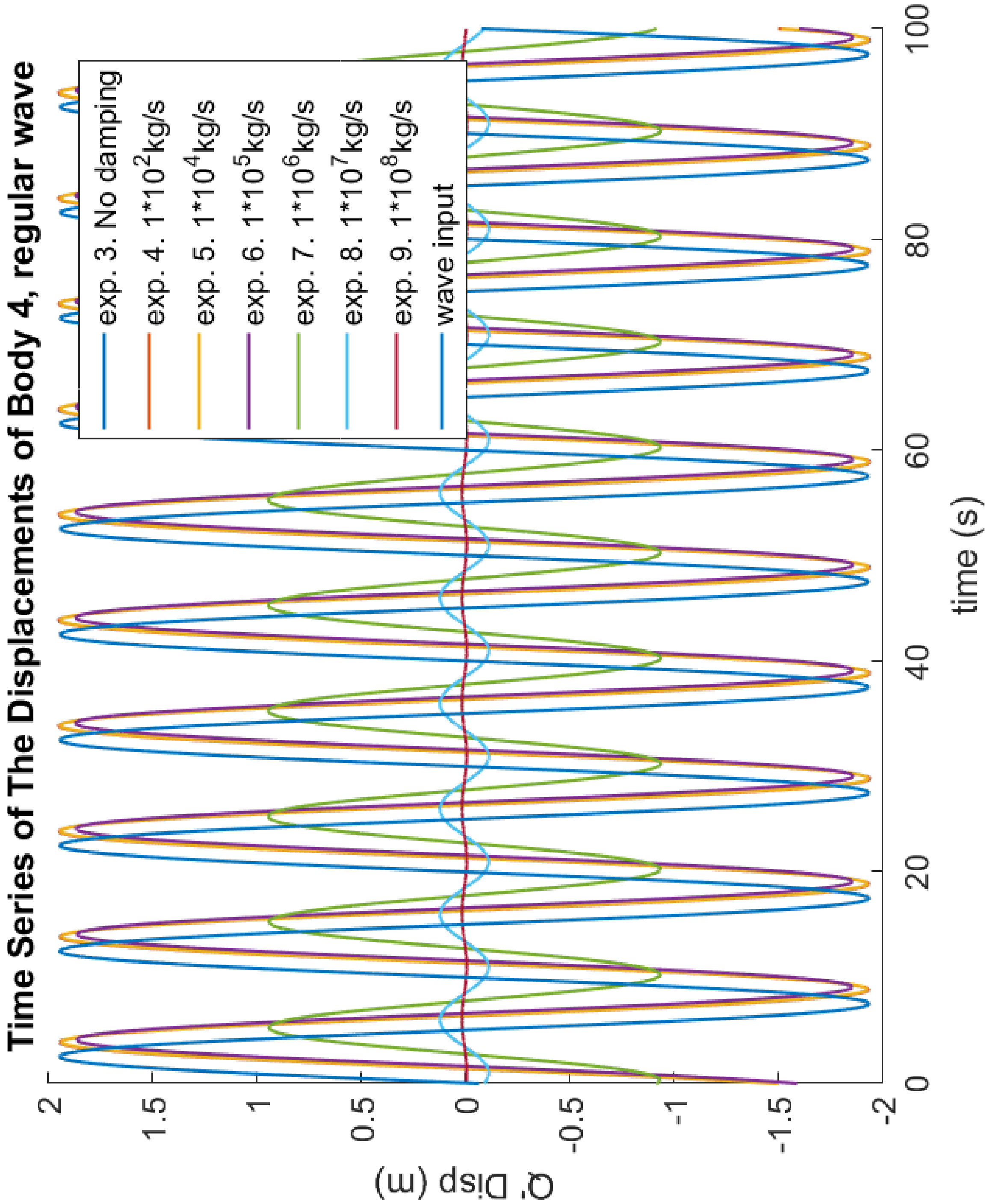

FIGURE A.4: Sweep, irregular wave, displacement of body 4

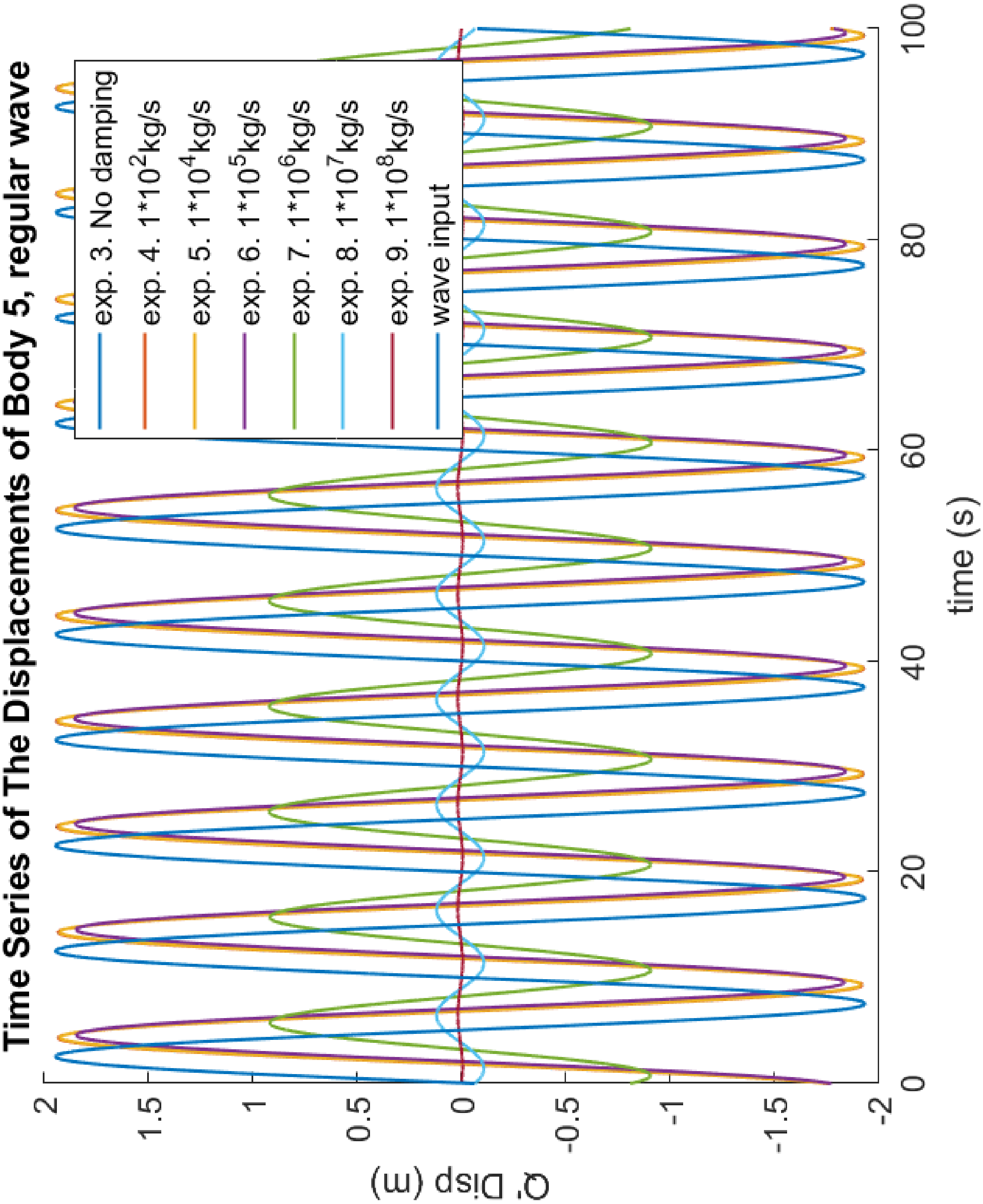

Figure A.5: Sweep, irregular wave, displacement of body 5

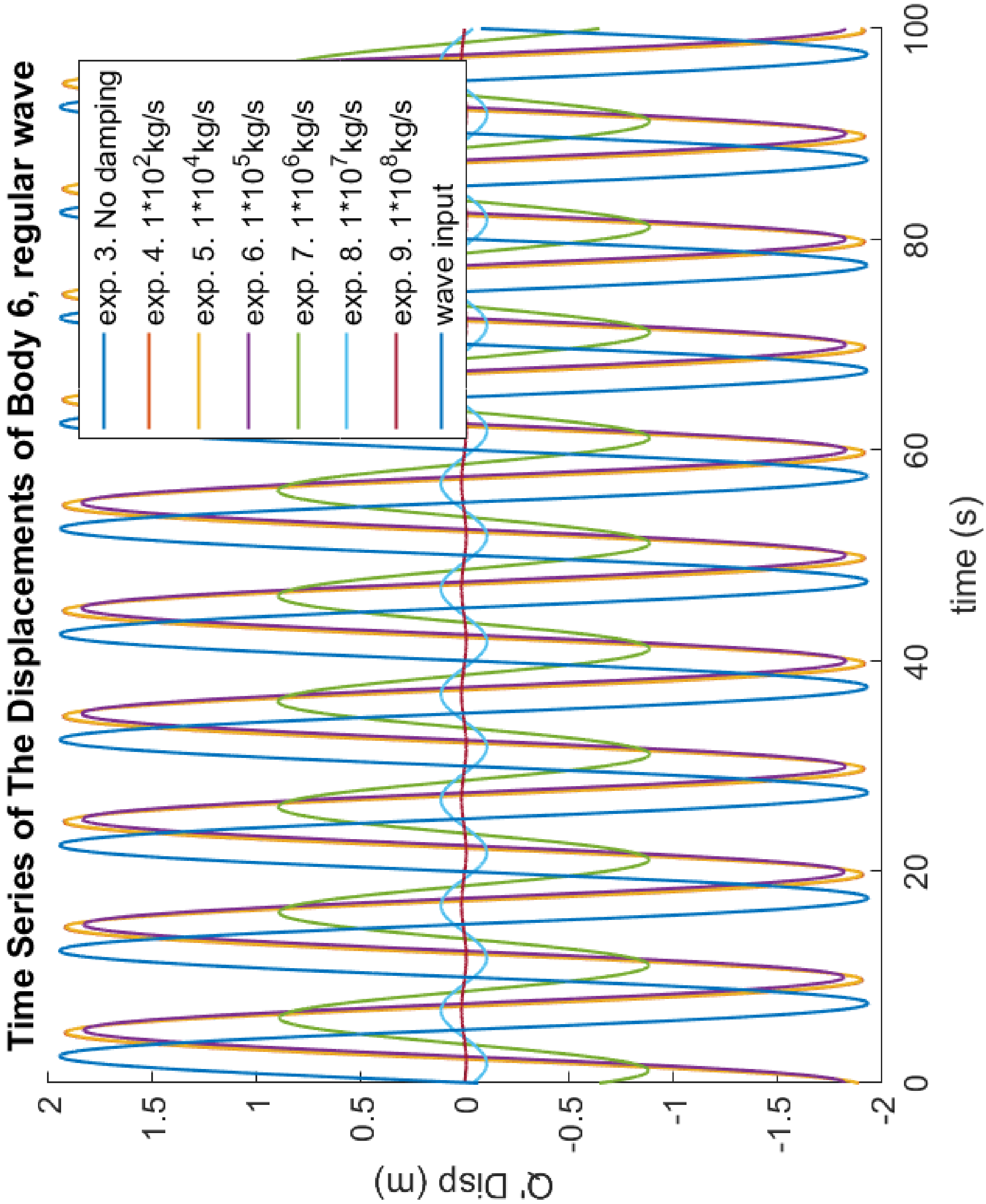

Figure A.6: Sweep, irregular wave, displacement of body 6

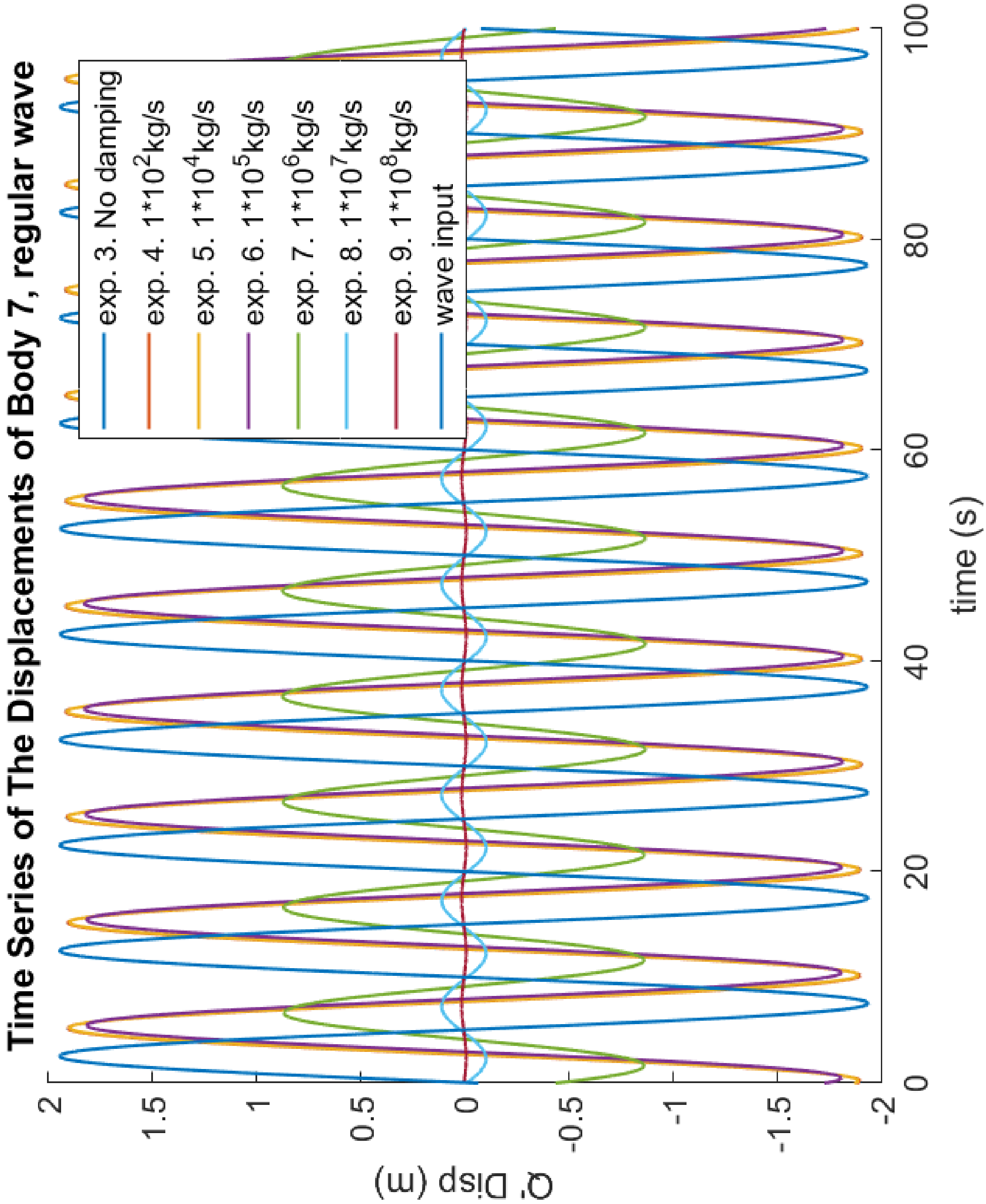

FIGURE A.7: Sweep, irregular wave, displacement of body 7

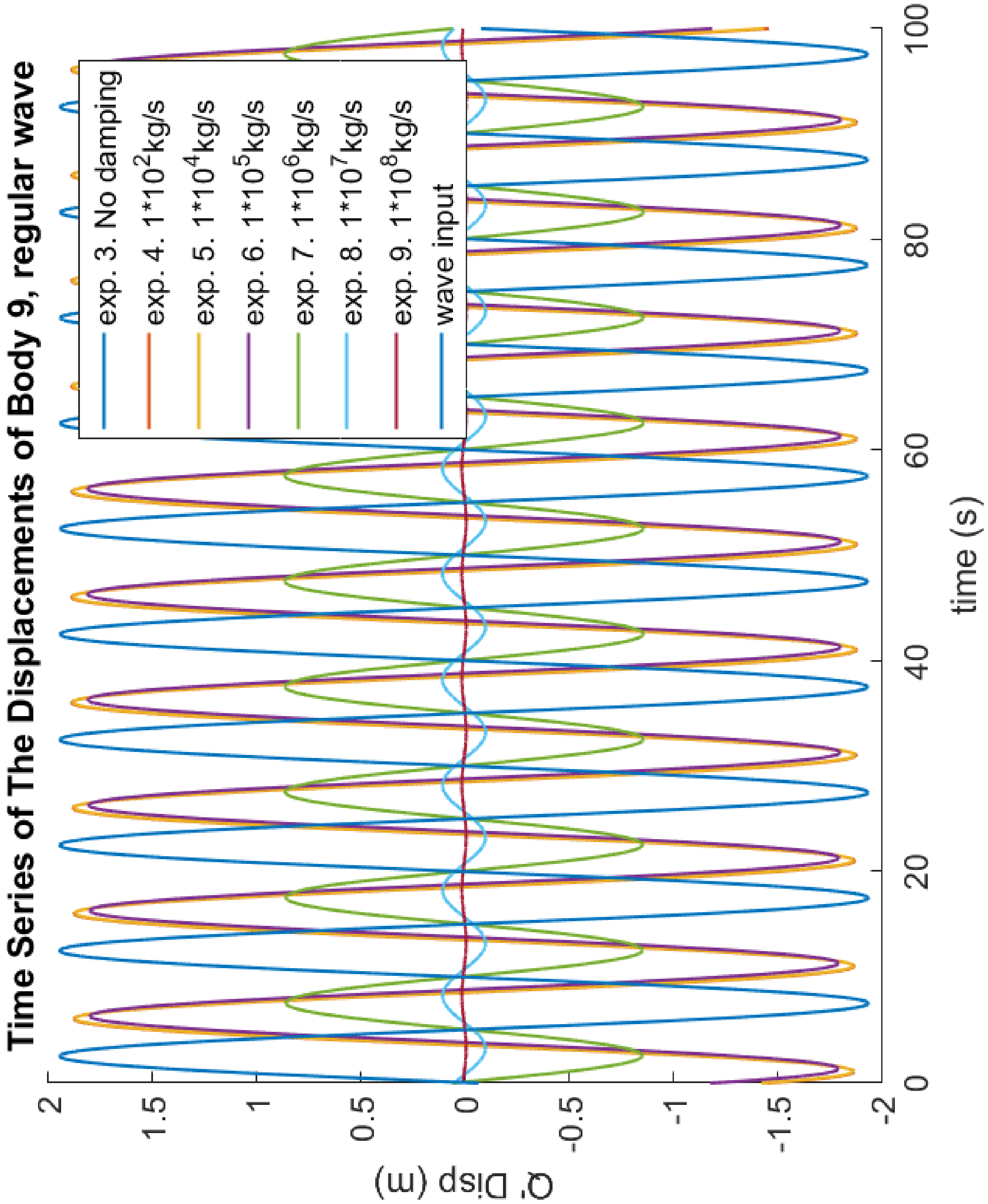

FIGURE A.9: Sweep, irregular wave, displacement of body 9

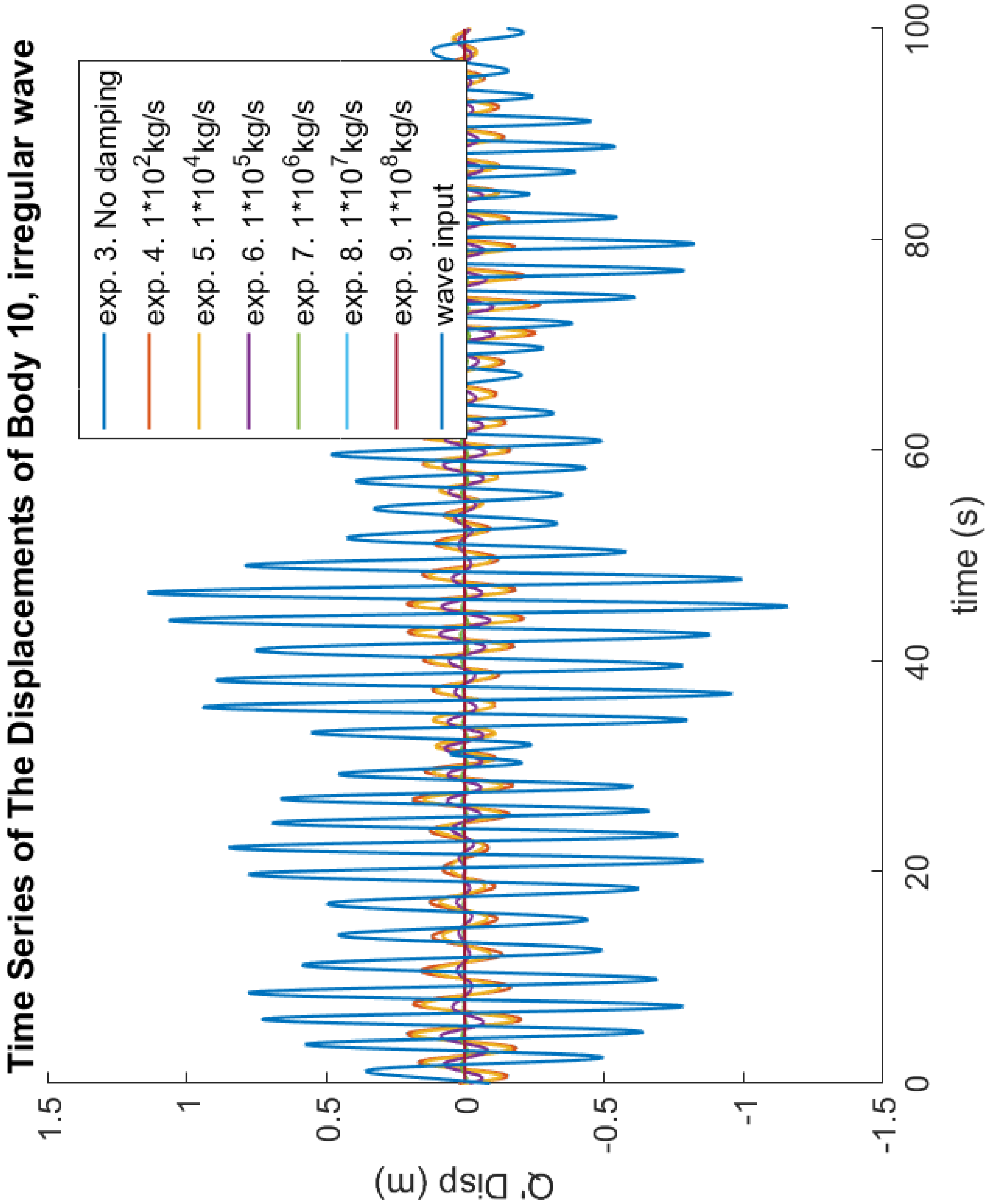

Figure A.10: Sweep, irregular wave, displacement of body 10

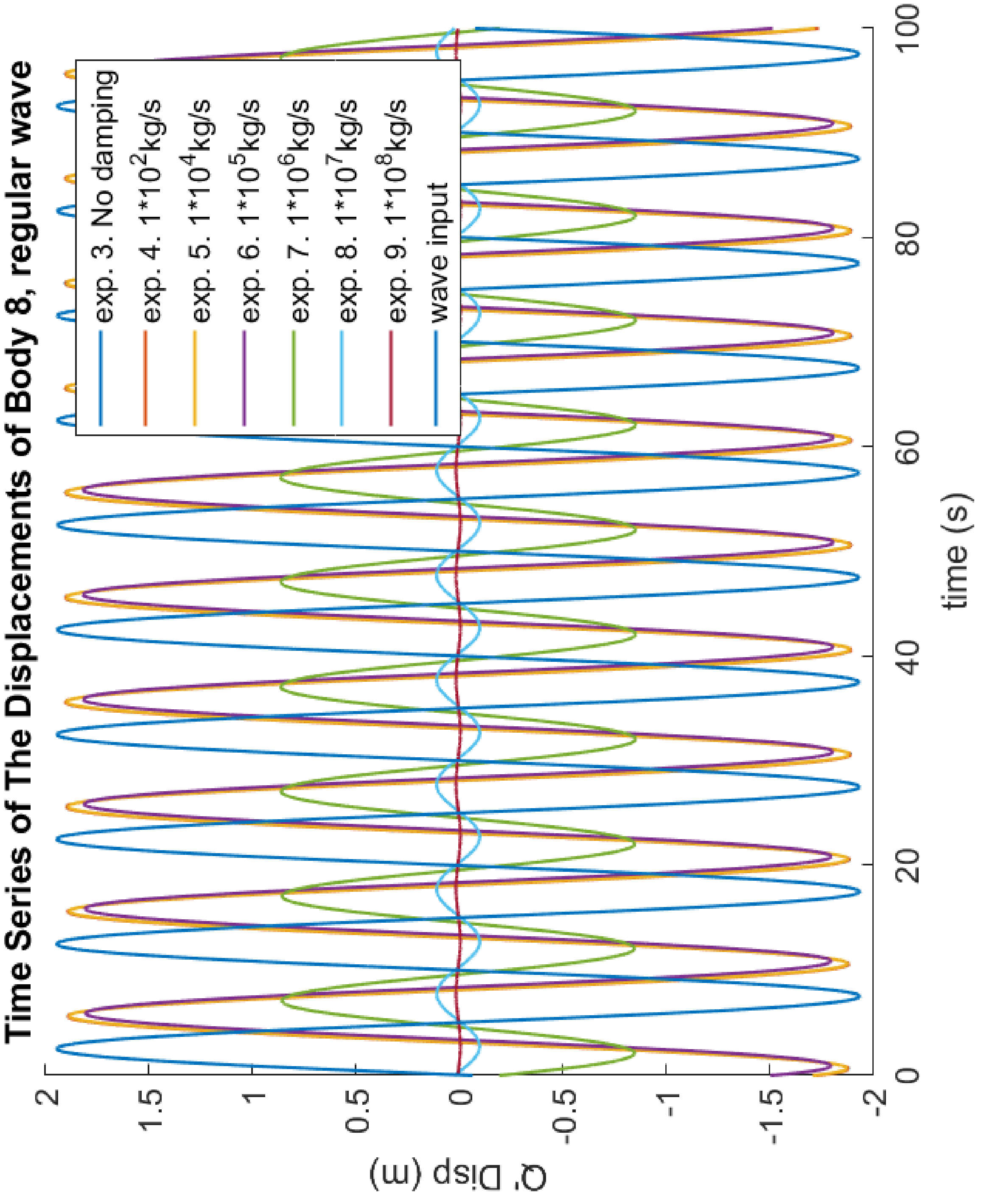

FIGURE A.8: Sweep, irregular wave, displacement of body 8

A.2 Irregular wave

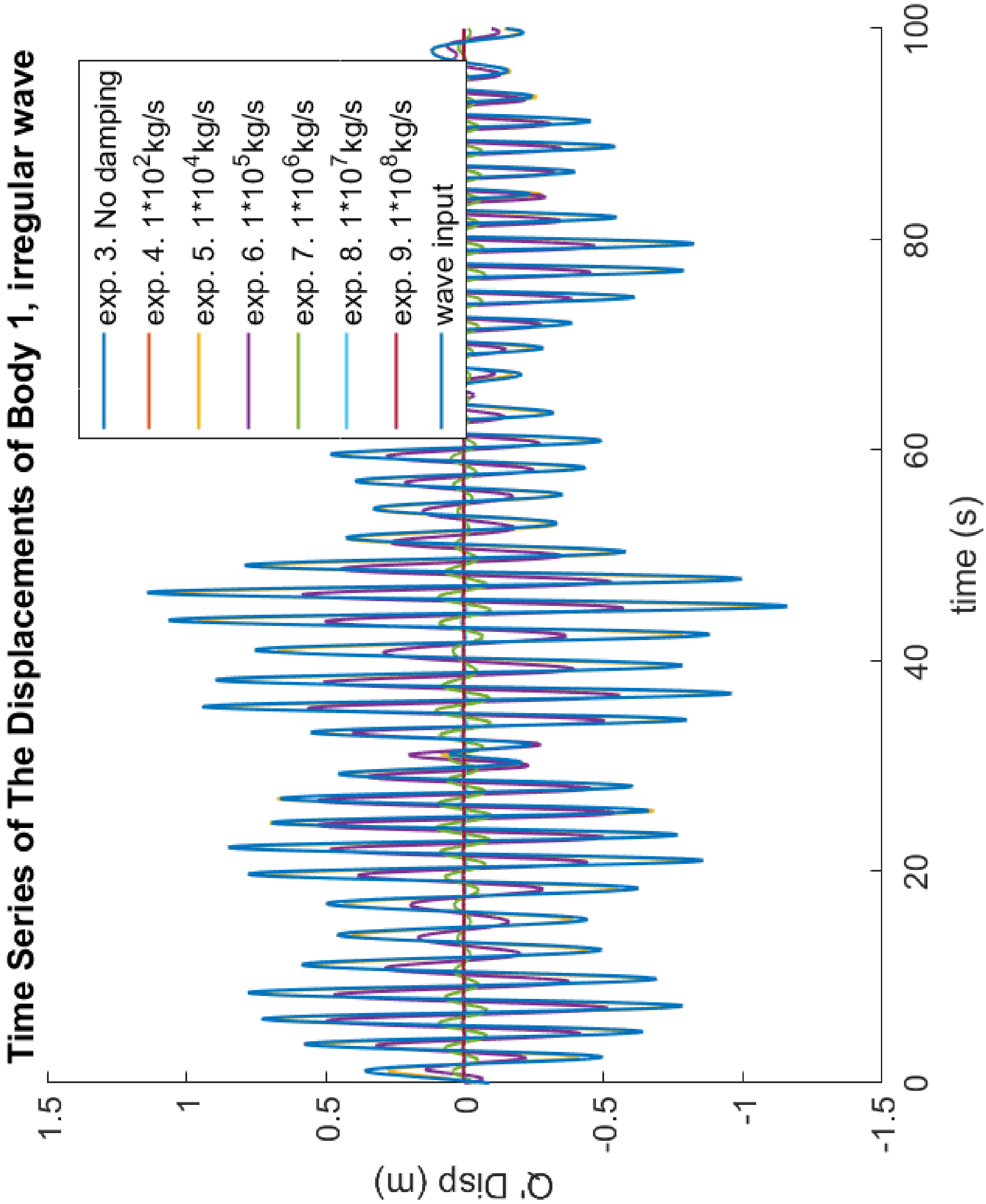

FIGURE A.11: Sweep, irregular wave, displacement of body 1

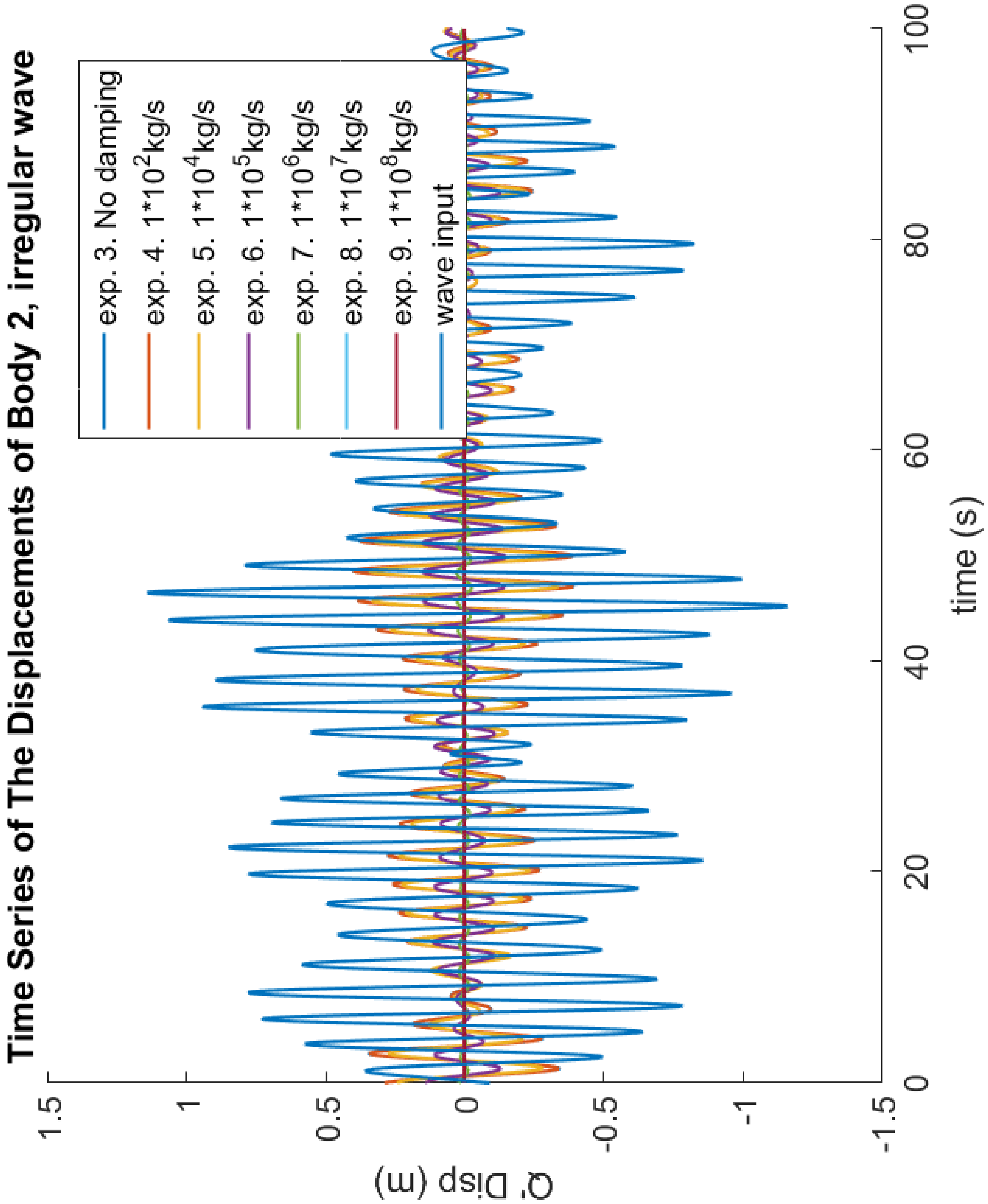

Figure A.12: Sweep, irregular wave, displacement of body 2

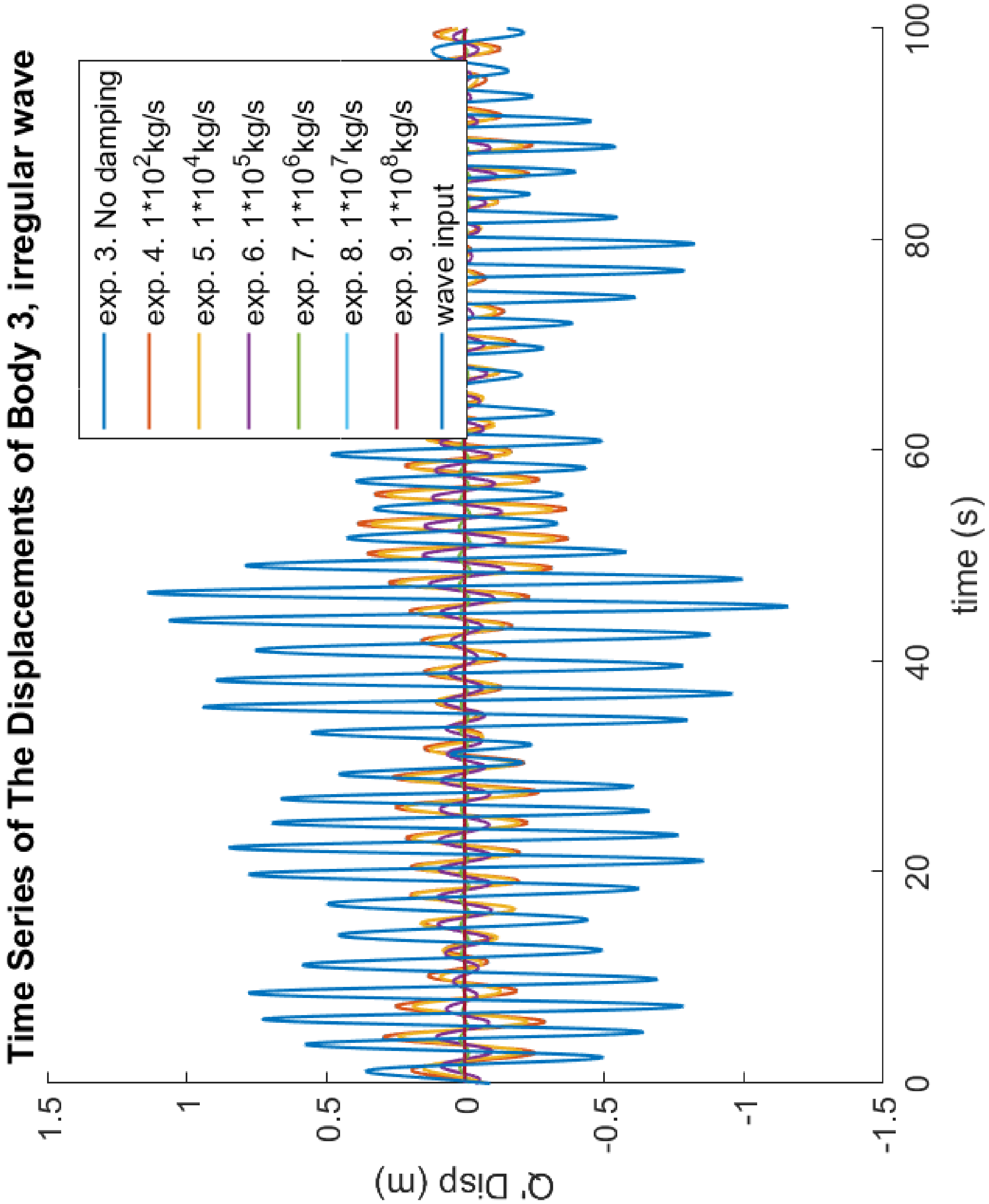

Figure A.13: Sweep, irregular wave, displacement of body 3

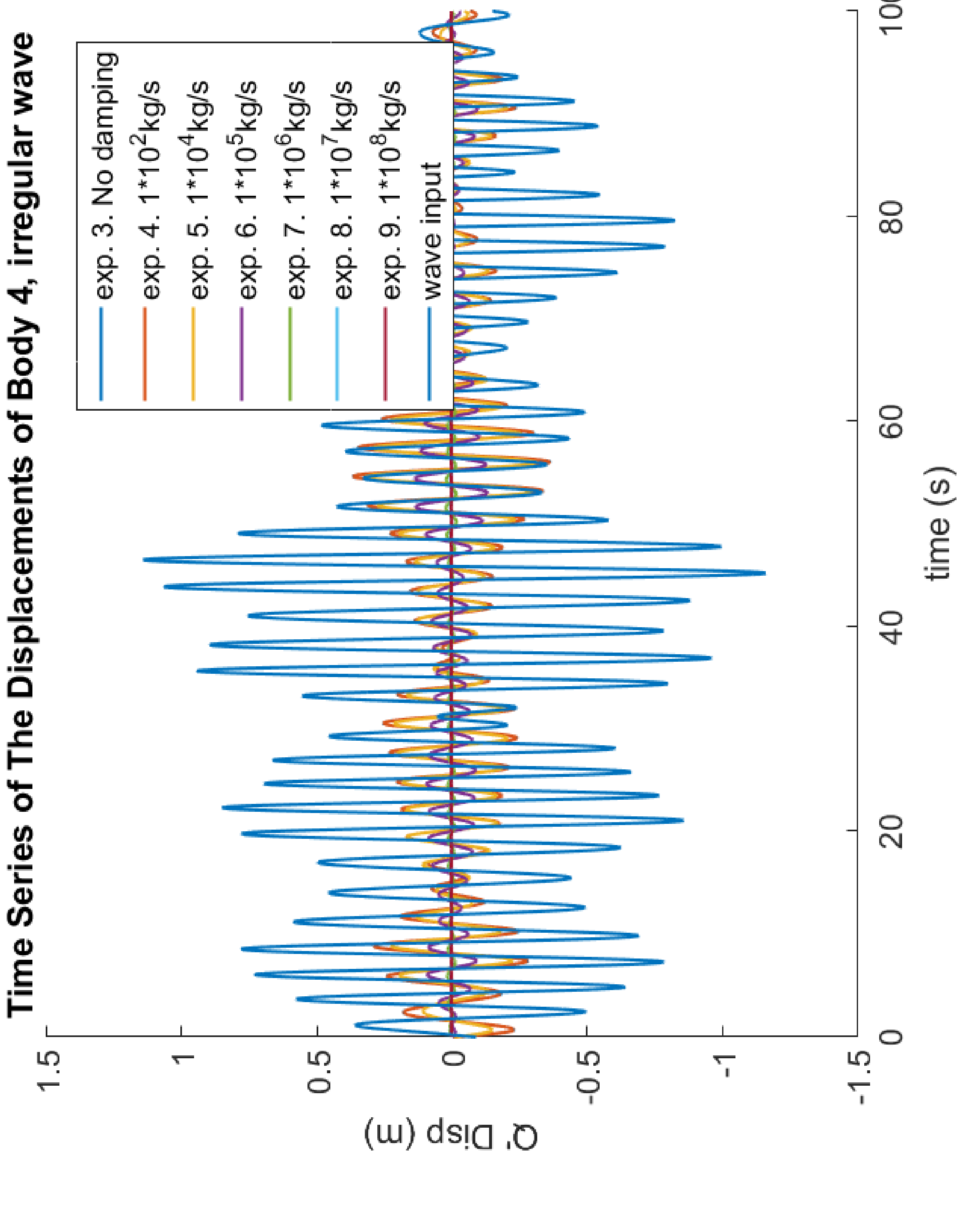

FIGURE A.14: Sweep, irregular wave, displacement of body 4

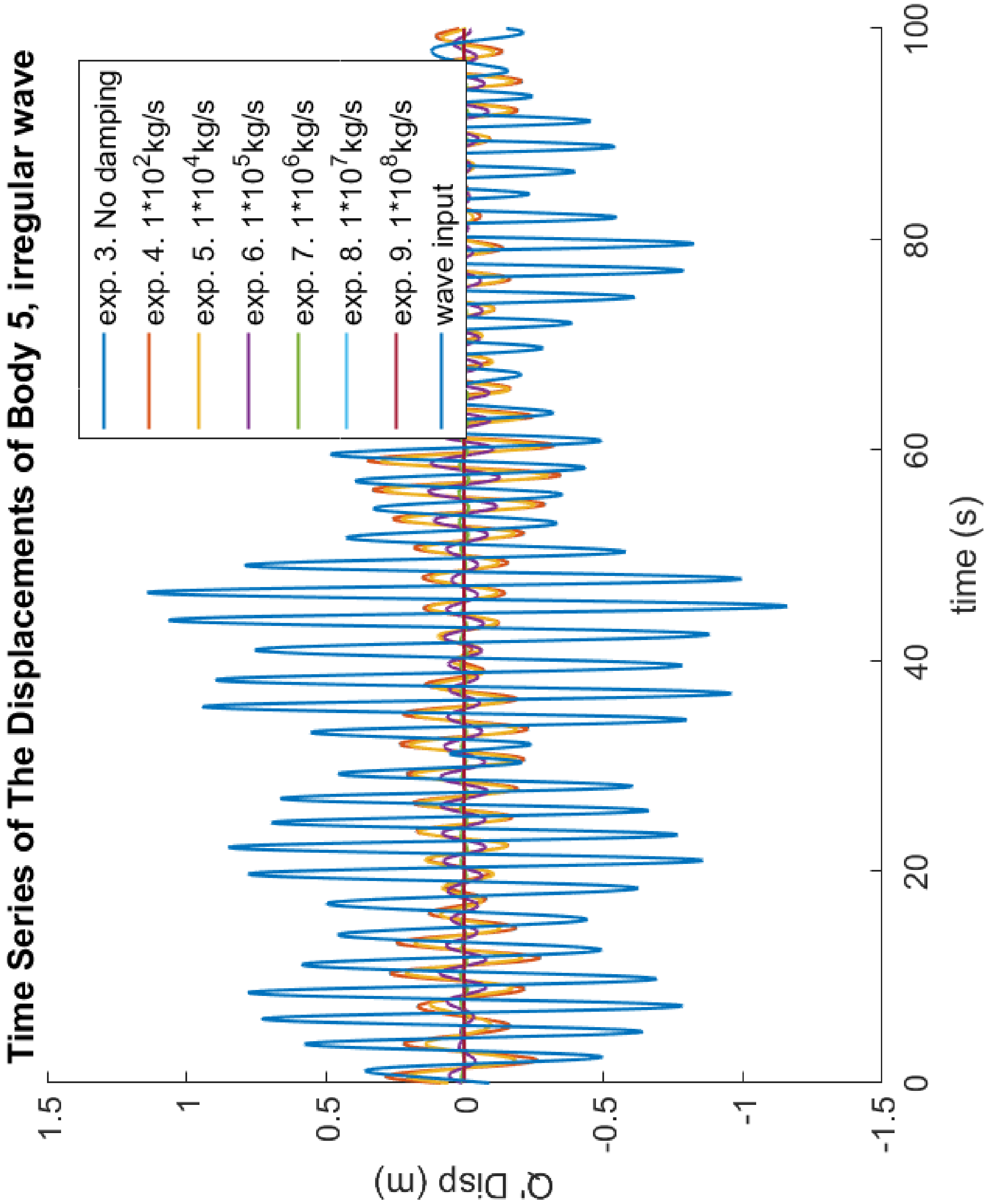

FIGURE A.15: Sweep, irregular wave, displacement of body 5

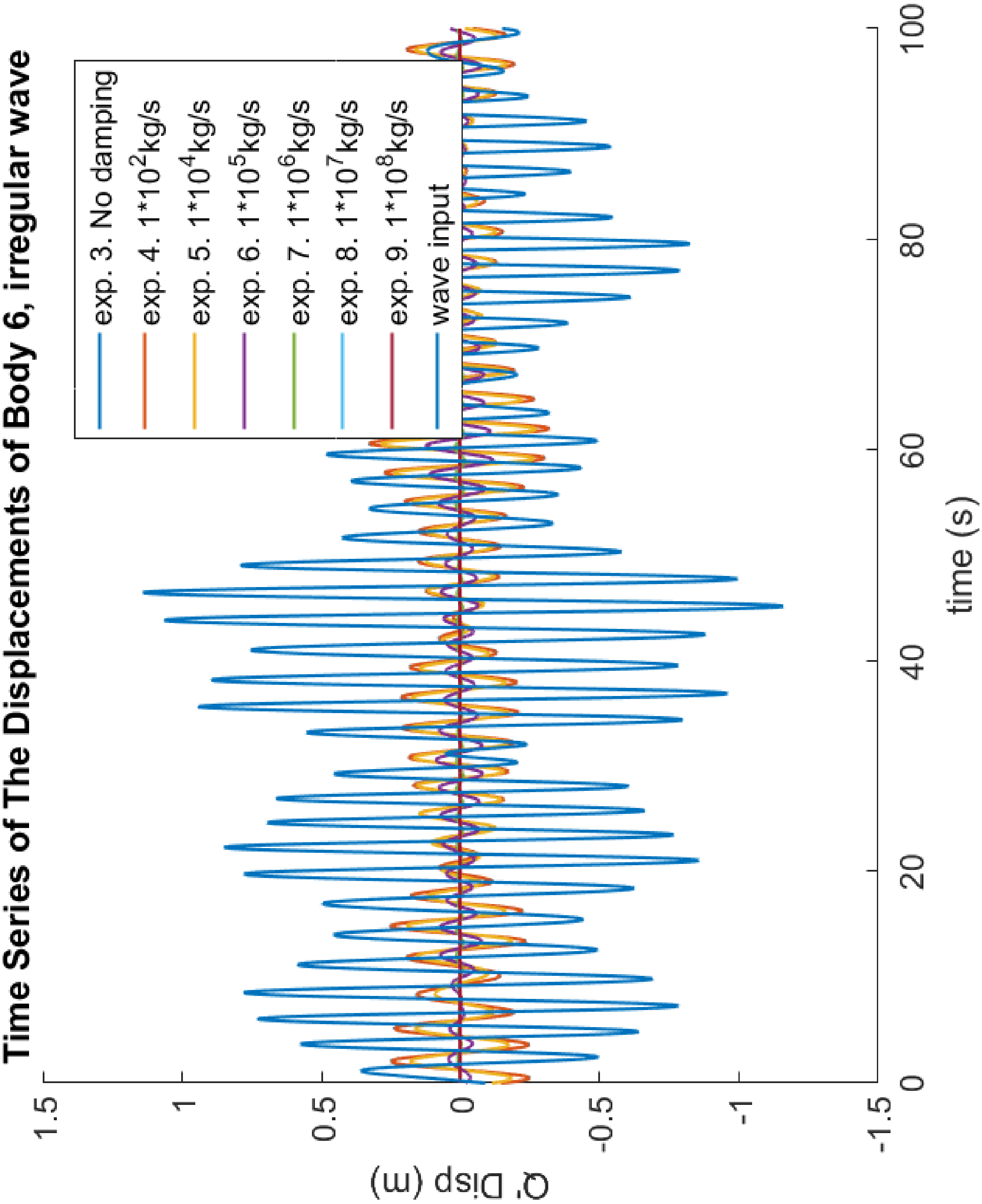

FIGURE A.16: Sweep, irregular wave, displacement of body 6

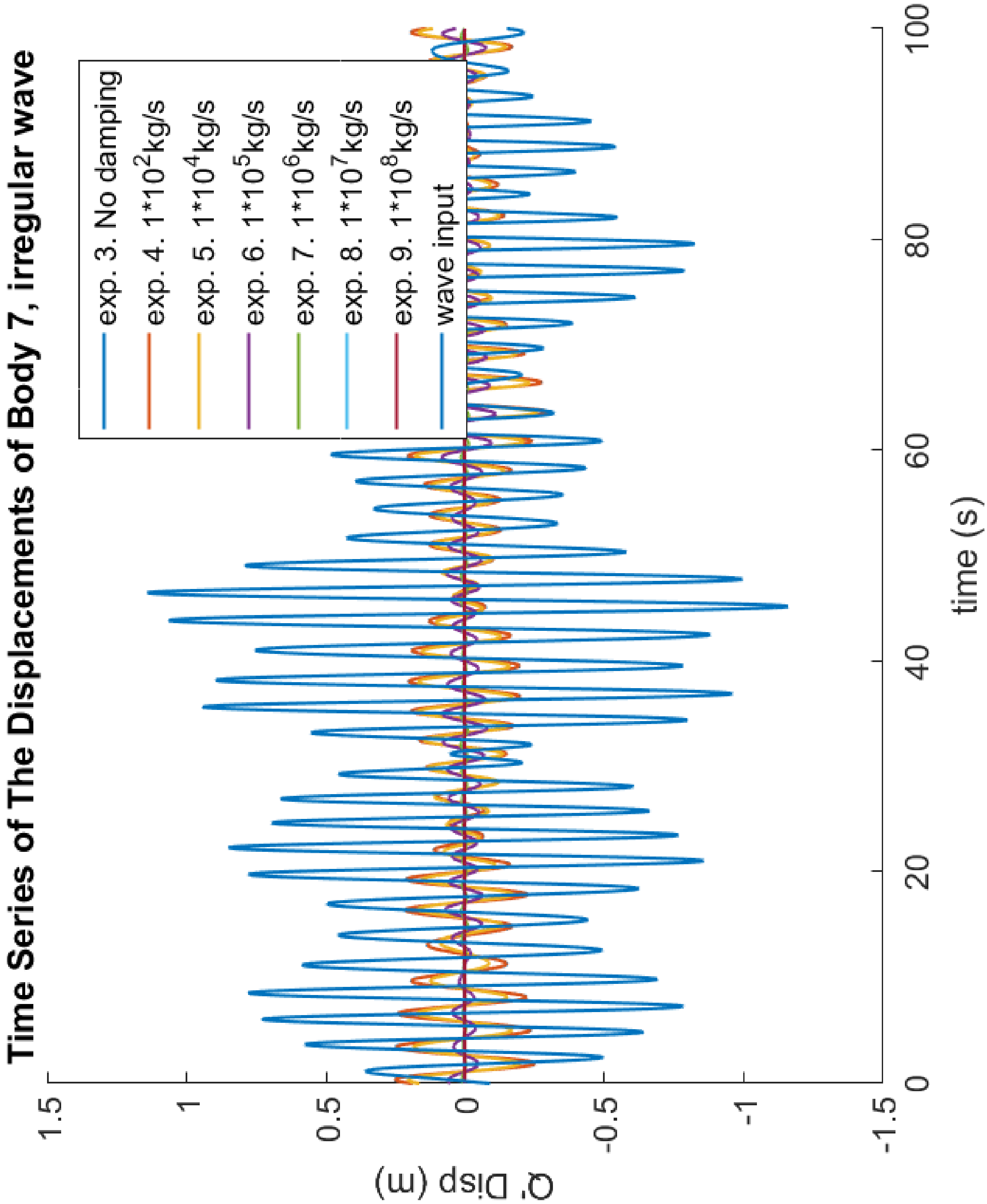

FIGURE A.17: Sweep, irregular wave, displacement of body 7

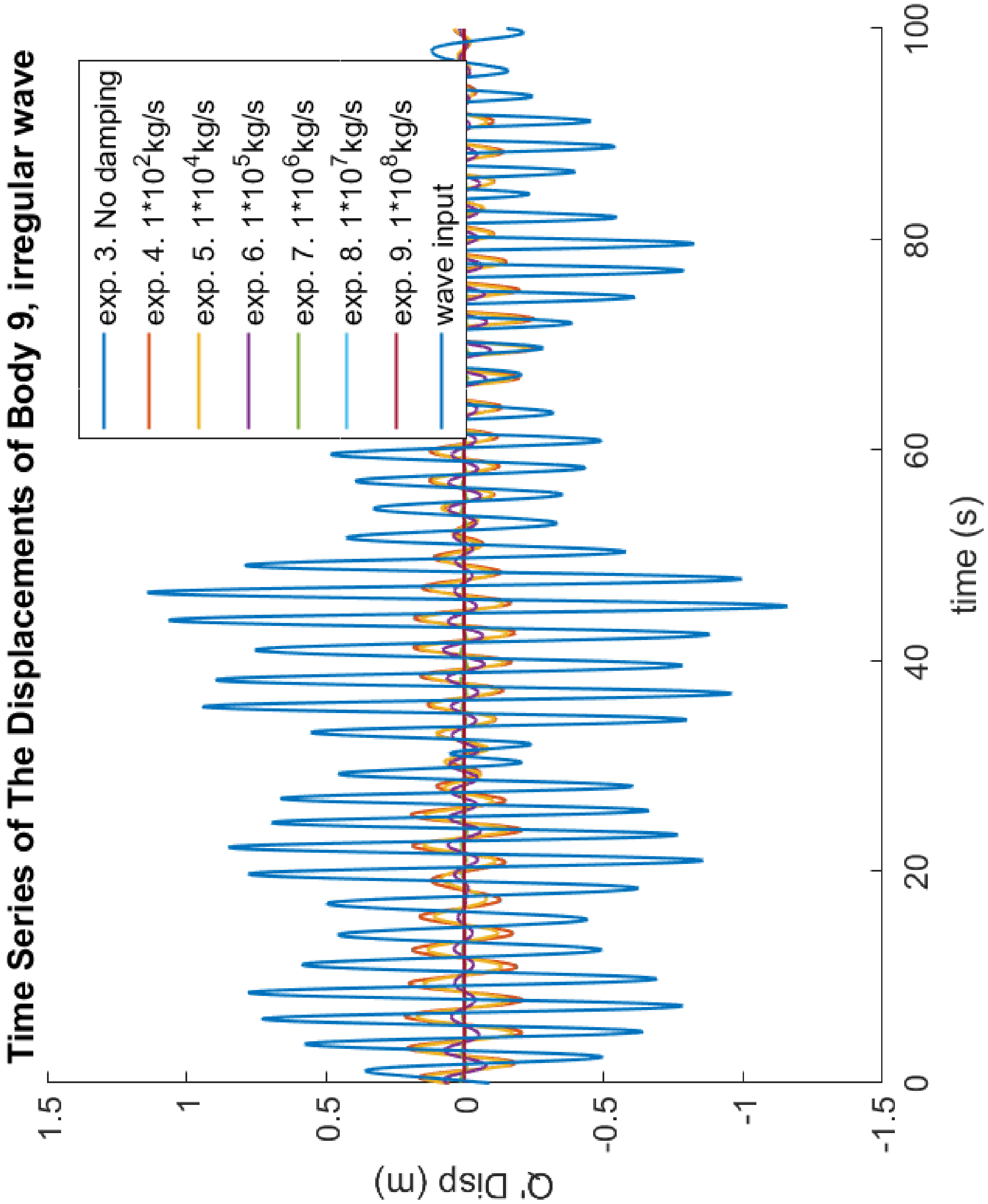

FIGURE A.19: Sweep, irregular wave, displacement of body 9

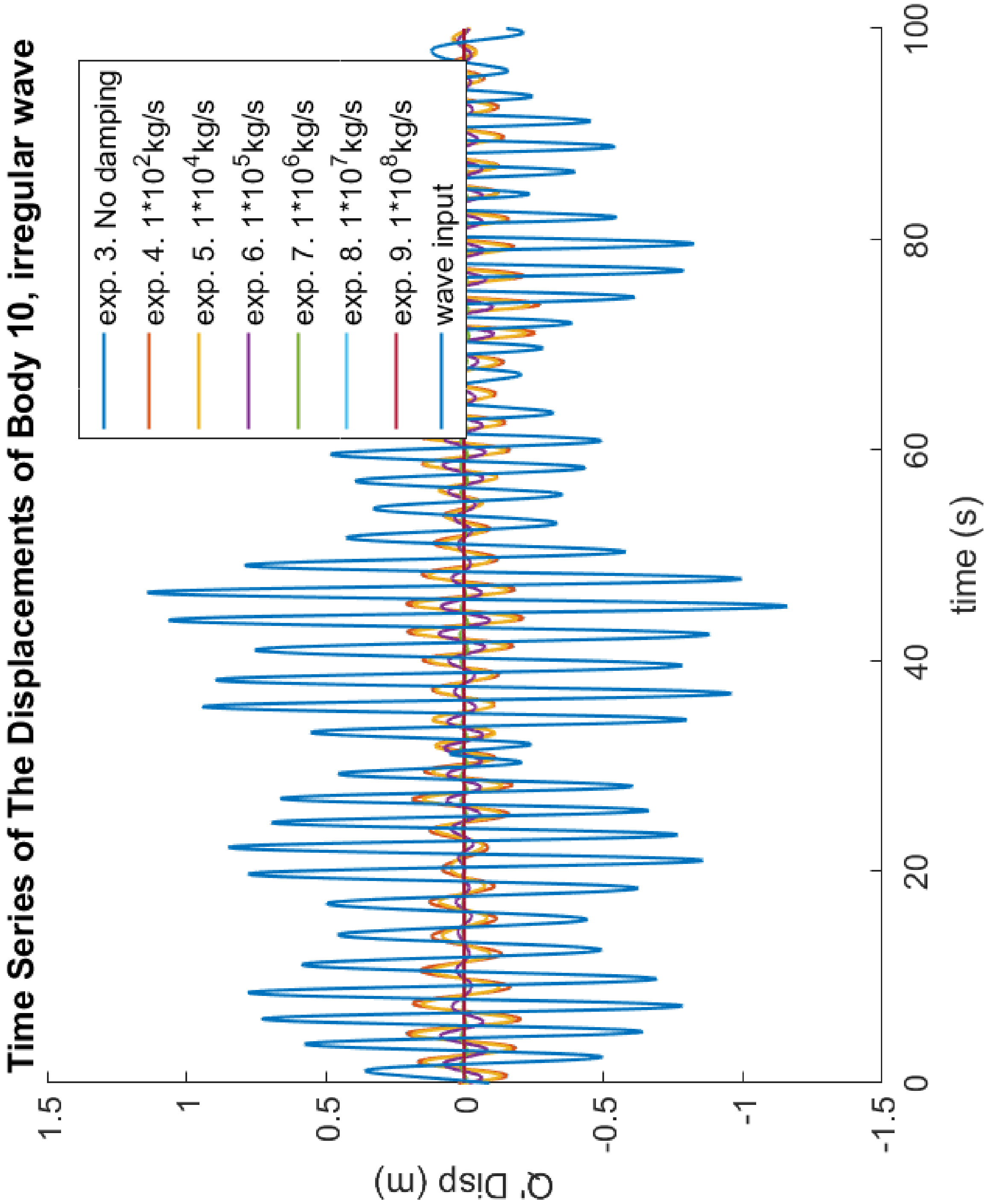

Figure A.20: Sweep, irregular wave, displacement of body 10

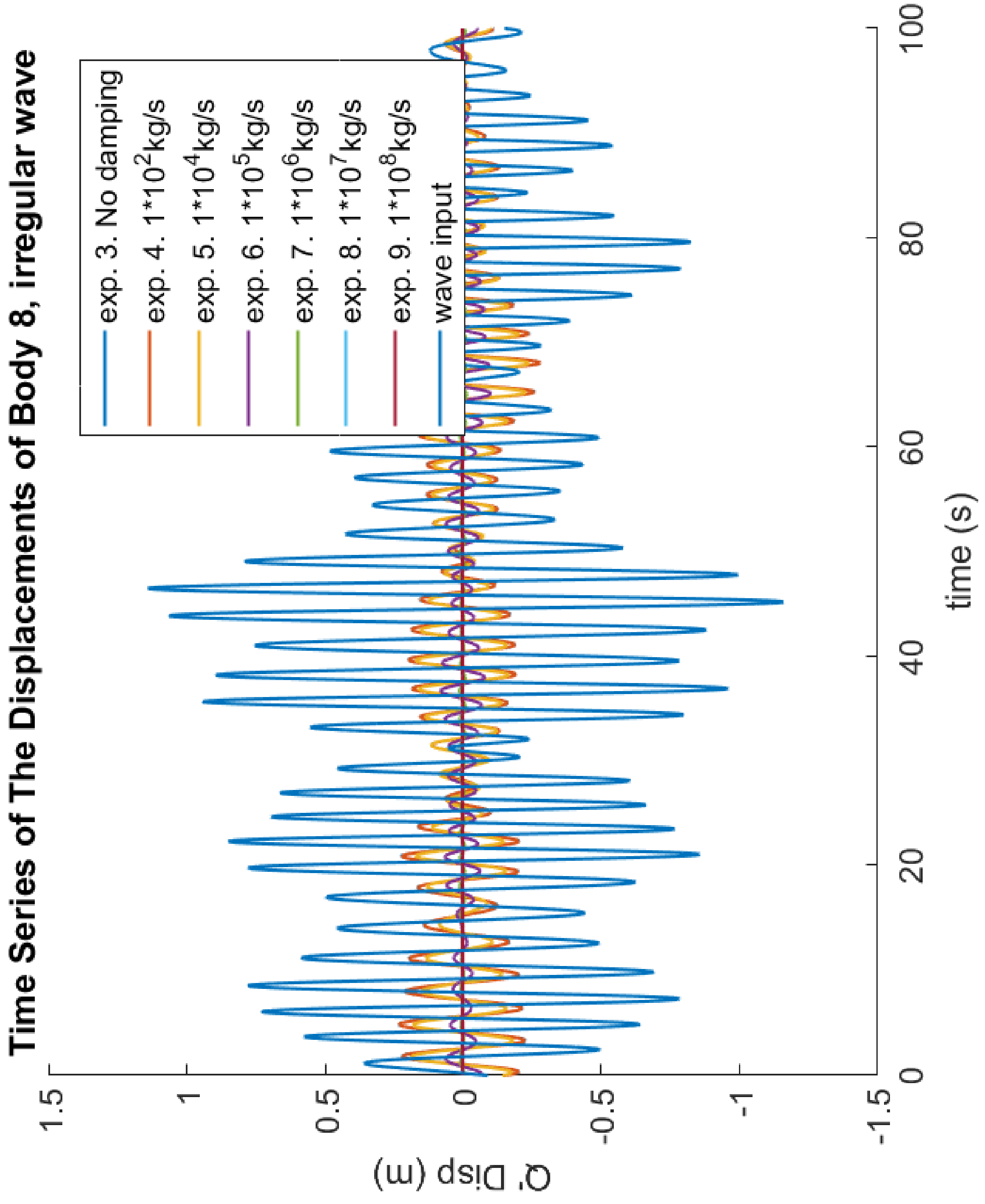

FIGURE A.18: Sweep, irregular wave, displacement of body 8

Bibliography

[1] Sociaal-Economische Raad. "Energieakkoord voor duurzame groei". In: *Geraadpleegd op 7 januari 2015, van http://www. energieakkoordser. nl/˜/media/files/internet /publicaties/overige /2010_2019/2013 /energieakkoordduurzame-groei/energieakkoord-duurzame-groei. ashx* (2013).

[2] Segers R. Meurink A. Muller G. "Hernieuwbare energie in Nederland 2016". In: *Hernieuwbare energie in Nederland URL: http://statline. cbs. nl/StatWeb/publication* (2016). URL: `https://www.cbs.nl/-/media/_pdf/2017/39/2017a403%20hernieuwbare%20energie%20in%20nederland%202016-web.pdf`.

[3] Benjamin Drew, Andrew R Plummer, and M Necip Sahinkaya. *A review of wave energy converter technology*. 2009.

[4] Kari Burman and Andy Walker. "Ocean energy technology overview". In: *US Department of Energy, Office of Energy Efficiency and Renewable Energy, Federal Energy Management Program* (2009).

[5] Se Joon Lim. *Wave energy converters*. 2013.

[6] Segen Farid Estefen, Paulo Roberto Da Costa, and Marcelo Martins Pinheiro. *Wave energy plant for electricity generation*. US Patent 8,099,955. 2012.

[7] Rezvan Alamian et al. "Evaluation of technologies for harvesting wave energy in Caspian Sea". In: *Renewable and Sustainable Energy Reviews* 32 (2014), pp. 468–476.

[8] CYJ Chen. "Determination of the right wave by empirical statistics: The wave energy resource assessment and the investigation of existing marine and coastal potential compatibility". In: *Journal of Ocean Engineering and Science* 1.4 (2016), pp. 284–288.

[9] URL: `"https://www.greenbiz.com/"`.

[10] Alok Jha. "Making Waves: UK firm harnesses power of the sea... in Portugal". In: *The Guardian* (2008), pp. 32–36.

[11] S Foteinis and T Tsoutsos. "Strategies to improve sustainability and offset the initial high capital expenditure of wave energy converters (WECs)". In: *Renewable and Sustainable Energy Reviews* 70 (2017), pp. 775–785.

[12] Ricardo Gobato, Alekssander Gobato, and Desire Francine Gobato Fedrigo. "Study Pelamis system to capture energy of ocean wave". In: *arXiv preprint arXiv:1508.01106* (2015).

[13] TJT Whittaker et al. "The Limpet Wave Power Project–the first years of operation". In: *Renewable Energy* (2004).

[14] Tom HEATH. "The Construction, Commissioning and Operation of the LIMPET Wave Energy Collector". In: *Wavegen, Reino Unido* (2001).

[15] Ion Bostan et al. "Sea Waves Energy". In: *Resilient Energy Systems*. Springer, 2013, pp. 455–507.

[16] Andreas Poullikkas. "Technology prospects of wave power systems". In: *Electronic Journal of Energy & Environment* 2.1 (2014), pp. 47–69.

[17] Sorin Diaconu and Eugen Rusu. “The environmental impact of a Wave Dragon array operating in the Black Sea”. In: *The Scientific World Journal* 2013 (2013).

[18] H Dijkstra et al. “Revenue optimization for the Ocean Grazer wave energy converter through storage utilization”. In: *Proc. of the RENEW2016 Conference.* 2016, pp. 207–213.

[19] M van Rooij. “Experimental validation of dynamical contact models of the Ocean Grazer”. In: *University of Groningen* (2015).

[20] URL: `"http://www.oceangrazer.com/"`.

[21] JJ Barradas-Berglind et al. “Towards Ocean Grazer’s Modular Power Take-Off System Modeling: a Port-Hamiltonian Approach”. In: *IFAC-PapersOnLine* 50.1 (2017), pp. 15663–15669.

[22] HE de Swart. “OCEAN WAVES”. In: *Lecturenotes, as part of the Master’s Programme ’Meteorology, Physical Oceanography and Climate’* (2015).

[23] Alessandro Toffoli and Elzbieta M Bitner-Gregersen. “Types of Ocean Surface Waves, Wave Classification”. In: *Encyclopedia of Maritime and Offshore Engineering* ().

[24] R Caflisch and H Lamb. “Hydrodynamics (Cambridge Mathematical Library)”. In: (1993).

[25] ”could not be determined”.

[26] Thomas Ainsworth. “Mariners weather log april 2006”. In: *Juneau, AK* (2006).

[27] MS Longuett-Higgins. “On the statistical distribution of the heights of sea waves”. In: *J. Mar. Research* 11.3 (1952), pp. 245–266.

[28] Jurjen A Battjes and Heiko W Groenendijk. “Wave height distributions on shallow foreshores”. In: *Coastal engineering* 40.3 (2000), pp. 161–182.

[29] Marlotte Mohr. “Calculation of power absorption from irregular waves by the floater blanket of the Ocean Grazer”. In: *Bachelor Thesis* (2018).

[30] Willard J Pierson and Lionel Moskowitz. “A proposed spectral form for fully developed wind seas based on the similarity theory of SA Kitaigorodskii”. In: *Journal of geophysical research* 69.24 (1964), pp. 5181–5190.

[31] Wah T Lee and Susan L Bales. *A Modified JONSWAP Spectrum Dependent Only On Wave Height and Period.* Tech. rep. DAVID W TAYLOR NAVAL SHIP RESEARCH and DEVELOPMENT CENTER BETHESDA MD SHIP PERFORMANCE DEPT, 1980.

[32] Steven A Hughes. *The TMA shallow-water spectrum description and applications.* Tech. rep. Coastal Engineering Research Center Vicksburg MS, 1984.

[33] Klaus Hasselmann et al. “Measurements of wind-wave growth and swell decay during the Joint North Sea Wave Project (JONSWAP)”. In: *Ergänzungsheft 8-12* (1973).

[34] Qiuying Guo and Zunyi Xu. “Simulation of deep-water waves based on JONSWAP spectrum and realization by MATLAB”. In: *Geoinformatics, 2011 19th International Conference on.* IEEE. 2011, pp. 1–4.

[35] Walter H Michel. “Sea spectra simplified”. In: *Marine Technology* 5.1 (1968), pp. 17–30.

[36] Turgut Sarpkaya and Michael Isaacson. “Mechanics of wave forces on offshore structures”. In: (1981).

[37] MOHAMMAD JAVAD KETABDARI and A Ranginkaman. “Simulation of random irregular sea waves for numerical and physical models using digital filters”. In: (2009).

[38] Steven A Hughes. *Physical models and laboratory techniques in coastal engineering.* Vol. 7. World Scientific, 1993.

[39] Jean-Baptiste Saulnier et al. “Mean power output estimation of WECs in simulated sea”. In: 710 (2009).

[40] Rico H Hansen, Morten M Kramer, and Enrique Vidal. “Discrete displacement hydraulic power take-off system for the wavestar wave energy converter”. In: *Energies* 6.8 (2013), pp. 4001–4044.

[41] MJ Tucker, Peter G Challenor, and DJT Carter. “Numerical simulation of a random sea: a common error and its effect upon wave group statistics”. In: *Applied ocean research* 6.2 (1984), pp. 118–122.

[42] Laura K Alford and Kevin J Maki. “Generating Large Deterministic Water Waves for Numerical Simulation”. In: *Ann Arbor* 1001 (), p. 48109.

[43] MD Miles and ER Funke. “A comparison of methods for synthesis of directional seas”. In: *Journal of Offshore Mechanics and Arctic Engineering* 111.1 (1989), pp. 43–48.

[44] Celso K Morooka, Irineu H Yokoo, et al. “Numerical simulation and spectral analysis of irregular sea waves”. In: *International Journal of Offshore and Polar Engineering* 7.03 (1997).

[45] Jeffrey A Fessler. “On transformations of random vectors”. In: *Commun. Signal Process. Lab., Dept. Elect. Eng. Comput. Sci., Univ. Michigan, Ann Arbor, MI, http://www. eecs. umich. edu/˜ fessler* (1998).

[46] Xavier Español Espinar. “Pseudorandom noise generators dedicated for acustic measurements”. In: (2012).

[47] Signal procssing toolbox MathWorks. “User’s Guide”. In: *Mathworks Inc* (2018). URL: `https://nl.mathworks.com/help/signal/ug/fir-filter-design.html`.

[48] Peter Frigaard, M Hgedal, and Morten Christensen. “Wave generation theory”. In: *Hydraulics and Coastal Engineering Laboratory, Dept. of Civil Engineering, Aalborg University, Aalborg (Denmark)* (1993).

[49] John G Proakis. *Digital signal processing: principles algorithms and applications*. Pearson Education India, 2001.

[50] Yaduvir Singh, Sweta Tripathi, and Manoj Pandey. “Analysis of digital iir filter with labview”. In: *Analysis* 10.6 (2010).

[51] MZ Almuzakki et al. “A port-Hamiltonian Approach to Cummins’ Equation for Floater Arrays with Linear Power-Take Off Systems”. In: *IFAC-PapersOnLine* 51.3 (2018), pp. 155–160.

[52] WE Cummins. *The Cummins equation*. Tech. rep. David Taylor Model Basin Washington DC, 1962.

[53] G Delhommeau. “Seakeeping codes aquadyn and aquaplus”. In: *19th WEGEMT School Numerical Simulation of Hydrodynamics: Ships and Offshore Structures* (1993).

[54] Aurélien Babarit and Gérard Delhommeau. “Theoretical and numerical aspects of the open source BEM solver NEMOH”. In: *11th European Wave and Tidal Energy Conference (EWTEC2015)*. 2015.

[55] Liangyi Luo. “SOFTWARE EFFICIENCY OR PERFORMANCE OPTIMIZATION AT THE SOFTWARE AND HARDWARE ARCHITECTURAL LEVEL”. In: *Information Technology and Software Architecture* (2013).

[56] Rens Folkertsma. “Mathematical modeling of slamming in a single-piston pump inside the Ocean Grazer”. In: *Bachelor Thesis* (2018).

[57] Y Wei et al. “Investigating the adaptability of the multi-pump multi-piston power take-off system for a novel wave energy converter”. In: *Renewable Energy* 111 (2017), pp. 598–610.

[58] Kelley Ruehl et al. “Preliminary verification and validation of WEC-Sim, an open-source wave energy converter design tool”. In: *ASME 2014 33rd International Conference on Ocean, Offshore and Arctic Engineering*. American Society of Mechanical Engineers. 2014, V09BT09A040–V09BT09A040.

[59] Yi-Hsiang Yu et al. “Design and analysis for a floating oscillating surge wave energy converter”. In: *ASME 2014 33rd International Conference on Ocean, Offshore and Arctic Engineering*. American Society of Mechanical Engineers. 2014, V09BT09A048–V09BT09A048.

[60] Bret Bosma et al. “WEC-Sim Phase 1 Validation Testing: Experimental Setup and Initial Results”. In: *ASME 2016 35th International Conference on Ocean, Offshore and Arctic Engineering*. American Society of Mechanical Engineers. 2016, V006T09A025–V006T09A025.

[61] Kelley Ruehl et al. “WEC-Sim Phase 1 Validation Testing: Numerical Modeling of Experiments”. In: *ASME 2016 35th International Conference on Ocean, Offshore and Arctic Engineering*. American Society of Mechanical Engineers. 2016, V006T09A026–V006T09A026.